



TECHNISCHE
UNIVERSITÄT
WIEN
Vienna University of Technology

Interaction and manipulation of nanofiber-trapped atoms with spin-orbit coupled light

DISSERTATION

zur Erlangung des akademischen Grades

Doktor der Naturwissenschaften

eingereicht von

Rudolf Mitsch

Matrikelnummer 1028068

Turmburggasse 13/2-3, 1060 Wien

an der
Fakultät für Physik der Technischen Universität Wien

Betreuung: Prof. Dr. Arno Rauschenbeutel, E141 – Atominstitut

Diese Dissertation haben begutachtet:

(Prof. Dr. Arno
Rauschenbeutel)

(Prof. Dr. Peter Lodahl)

Wien, 03.09.2014

(Rudolf Mitsch)



TECHNISCHE
UNIVERSITÄT
WIEN
Vienna University of Technology

Interaction and manipulation of nanofiber-trapped atoms with spin-orbit coupled light

DISSERTATION

submitted in partial fulfillment of the requirements for the degree of

Doktor der Naturwissenschaften

by

Rudolf Mitsch

Registration Number 1028068

Turmburggasse 13/2-3, 1060 Wien

to the Faculty of Physics
at the Vienna University of Technology

Advisor: Prof. Dr. Arno Rauschenbeutel, E141 – Atominstitut

The dissertation has been reviewed by:

(Prof. Dr. Arno
Rauschenbeutel)

(Prof. Dr. Peter Lodahl)

Wien, 03.09.2014

(Rudolf Mitsch)

Abstract

Light is often described as an electromagnetic wave that is transversely polarized with respect to its propagation direction. This description however breaks down when the light field is strongly transversely confined. Such a light field exhibits a longitudinal component of its electromagnetic field. In this situation the spin and the orbital angular momentum of light are coupled and thus not independent quantities anymore, e.g., the local spin depends on the propagation direction of the light field.

In this thesis, the interaction between nanofiber-trapped atoms and spin-orbit coupled light fields is studied in the dispersive and the resonant regime. In our system, the nanofiber provides an evanescent field interface between the strongly guided optical mode and neutral cesium atoms. The atoms are confined in two diametric arrays in the vicinity of the nanofiber surface using a nanofiber-based two-color optical dipole trap. It is demonstrated that by using the peculiar polarization pattern of the guided light fields, the two atomic ensembles can be simultaneously optically pumped to opposite Zeeman states. Furthermore, it is shown that the state-dependent light shifts induced by a fictitious magnetic field can be locally distinct. This enables the independent coherent manipulation of the two ensembles via microwave radiation.

Moreover, due to the spin-orbit interaction of light, the system exhibits asymmetric scattering of photons by the atoms into counter-propagating nanofiber-guided modes. An asymmetry of the scattering rates into the two propagation directions higher than 10:1 is demonstrated. It is presented that this asymmetry can be tailored by the internal state of the atom and the polarization of the excitation light field. Additionally, it is shown that the spin-orbit interaction in our system can lead to nonreciprocal transmission of a nanofiber-guided light field. Building on this property a nanoscale optical diode is demonstrated, which can be operated down to the single-photon regime.

Kurzfassung

Licht wird meistens als elektromagnetische Welle beschrieben, die bezüglich ihrer Ausbreitungsrichtung transversal polarisiert ist. Diese Beschreibung ist für Lichtfelder, die lateral stark eingeschlossen sind aber nicht mehr zutreffend. Solche Lichtfelder weisen eine longitudinale Komponente in ihrem elektrischen Feld auf. Wenn dies der Fall ist, sind Spin- und Bahndrehimpuls des Lichtfeldes gekoppelt. Sie sind damit keine voneinander unabhängigen Größen mehr, was dazu führt, dass zum Beispiel der lokale Spindrehimpuls von der Ausbreitungsrichtung des Lichtfeldes abhängt.

In dieser Arbeit wird die Wechselwirkung von Atomen, die an einer Nanofaser gefangen sind, und Licht, das Spin-Bahn-Kopplung aufweist, untersucht. In unserem System wird durch die Nanofaser eine Schnittstelle zwischen neutralen Cäsium-Atomen und dem evaneszenten Feld der stark geführten optischen Moden realisiert. Mit Hilfe einer optischen Zweifarben-Falle, die auf Dipolkräften beruht, sind die Atome nahe der Oberfläche der Nanofaser in zwei diametral gegenüberliegenden Reihen gefangen. Die besondere Polarisation des evaneszenten Feldes ermöglicht es, die beiden atomaren Ensembles gleichzeitig durch optisches Pumpen in unterschiedliche Zeeman-Zustände zu bringen. In dieser Arbeit wird außerdem gezeigt, dass die zustandsabhängige Verschiebung der Energieniveaus, die durch fiktive Magnetfelder induziert wird, von der räumlichen Position der Atome abhängt. Dies ermöglicht die unabhängige und kohärente Manipulation der beiden atomaren Ensembles mit Mikrowellenstrahlung.

Photonen, die von den Atomen gestreut werden, koppeln durch die Spin-Bahn-Wechselwirkung von Licht unterschiedlich stark an Moden, die sich in entgegengesetzter Richtung in der Nanofaser ausbreiten. Hier wird gezeigt, dass diese Asymmetrie der Streuraten in die beiden Ausbreitungsrichtungen höher als 10:1 sein kann. Die Asymmetrie kann man abhängig von der Polarisation des anregenden Lichtfeldes sowie des inneren Zustandes der Atome beeinflussen. Hinzu kommt, dass die Spin-Bahn-Wechselwirkung von Licht in unserem System dazu führen kann, dass Lichtfelder abhängig von ihrer Ausbreitungsrichtung durch die Nanofaser unterschiedlich stark transmittiert werden. Basierend auf diesem Effekt wird gezeigt, dass eine optische Diode im Nanomaßstab realisiert werden kann, die auch mit einzelnen Photonen noch funktioniert.

List of Publications

In the process of working on this thesis, the following articles have been published in peer-reviewed journals or will be published soon:

- R. Mitsch, C. Sayrin, B. Albrecht, P. Schneeweiss, and A. Rauschenbeutel.
Directional nanophotonic atom–waveguide interface based on spin–orbit coupling of light
accepted for publication in *Nat. Phys.*
(*arXiv.org*, arxiv:1406.0896, 2014.)
- R. Mitsch, C. Sayrin, B. Albrecht, P. Schneeweiss, and A. Rauschenbeutel.
Exploiting the local polarization of strongly confined light for sub-micrometer-resolution
internal state preparation and manipulation of cold atoms
Phys. Rev. A, 89:063829, 2014.
- D. Reitz, C. Sayrin, B. Albrecht, I. Mazets, R. Mitsch, P. Schneeweiss, and A. Rauschen-
beutel.
Backscattering properties of a waveguide-coupled array of atoms in the strongly non-
paraxial regime
Phys. Rev. A, 89:031804(R), 2014.
- D. Reitz, C. Sayrin, R. Mitsch, P. Schneeweiss, and A. Rauschenbeutel.
Coherence properties of nanofiber-trapped cesium atoms
Phys. Rev. Lett., 110:243603, 2013.
- P. Schneeweiss, S. T. Dawkins, R. Mitsch, D. Reitz, E. Vetsch, and A. Rauschenbeutel.
A nanofiber-based optical conveyor belt for cold atoms
Appl. Phys. B, 110:279, 2013.
- E. Vetsch, S. T. Dawkins, R. Mitsch, D. Reitz, P. Schneeweiss, and A. Rauschenbeutel.
Nanofiber-based optical trapping of cold neutral atoms
IEEE J. Quantum Electron., 18(6):1763, 2012.
- S. T. Dawkins, R. Mitsch, D. Reitz, E. Vetsch, and A. Rauschenbeutel.
Dispersive Optical Interface Based on Nanofiber-Trapped Atoms
Phys. Rev. Lett., 107:243601, 2011.

Contents

1	Introduction	1
2	Optical nanofibers	5
2.1	Modes guided by an optical fiber	6
2.1.1	Wave equations for a circular waveguide	6
2.1.2	A step-index circular waveguide	8
2.1.3	The fundamental mode for nanofibers	13
2.2	Polarization of the fundamental mode	15
2.3	Spin-orbit interaction	17
2.3.1	Poynting vector and angular momentum density	19
2.3.2	Maximizing the spin-orbit interaction	21
2.4	Tapered optical fiber with a nanofiber waist	22
3	Atom-light interaction	27
3.1	Hyperfine interaction	27
3.2	AC Stark shift and atomic polarizability	29
3.2.1	AC Stark interaction	29
3.3	A two-color dipole trap	33
3.3.1	Dipole trap for neutral cesium atoms	33
3.3.2	Eigenstates and eigenenergies at the trapping minimum	37
3.4	Fictitious magnetic fields	40
4	Nanofiber-based trapping and interfacing neutral cesium atoms	45
4.1	Introduction	45
4.2	Experimental setup	46
4.2.1	Vacuum setup	46
4.2.2	Magneto-optical trap	46
4.2.3	Nanofiber-based dipole trap	49
4.2.4	Detection system	51
4.3	Characterization of nanofiber-trapped atoms	52
4.3.1	Spectroscopy and saturation	53
4.3.2	Coherence properties	57
4.3.3	Manipulation of first order magnetic field-sensitive states	59

5	Discerning and selectively manipulating nanofiber-trapped atoms	63
5.1	Introduction	63
5.2	Optical Pumping	64
5.2.1	Optical pumping into $m_F = 0$	65
5.2.2	Optical pumping into the outermost Zeeman states	68
5.3	Selective addressing of atoms prepared in the same substate	72
5.3.1	Lifting the degeneracy between the two atomic ensembles	73
5.3.2	Levelshifts due to fictitious magnetic fields	74
5.3.3	Discerning atoms prepared in $m_F = 0$	77
5.3.4	Selectively addressing magnetic field-sensitive states	78
5.3.5	Limitations of the methods involving fictitious magnetic fields	83
5.4	Optimizing the trapping potential	84
6	Nonreciprocal waveguide based on spin–orbit interaction	87
6.1	Directional spontaneous emission into optical nanofibers	88
6.1.1	Basic idea of the experiment	88
6.1.2	Light scattering by an optical nanofiber	89
6.1.3	Experimental realization	92
6.2	Nanofiber-based optical diode	99
6.2.1	Basic idea of the nanofiber-based optical diode	100
6.2.2	Experimental realization	101
7	Summary & Outlook	109
	Bibliography	115

Introduction

The research on interaction of light and matter in the quantum regime is highly versatile and has been very fruitful in the last decades. Only two years ago, in 2012, S. Haroche and D. Wineland were awarded with the Nobel Prize in Physics “*for ground-breaking experimental methods that enable measuring and manipulation of individual quantum systems*” [1,2]. In order to gain control over the external and internal degrees of freedom of single quantum systems like ions [3] or atoms [4] one lets them interact with electromagnetic radiation. Over the years, matter-based quantum systems with long coherence times could be realized with dopant ions in crystals [5], nitrogen vacancy centers [6], quantum dots [7], trapped neutral atoms [8], and trapped ions [9]. On these grounds, the obtained advances, especially in the field of quantum information processing [10], lead to the idea of combing different types of these systems into so-called hybrid quantum systems [11] to profit from their distinct advantages. A light–matter interface, for example, combines the ability of long-coherence times systems to process and store quantum information with the advantage of photons that are excellent in transmitting quantum information. Such a hybrid quantum system can be a building block in a quantum communication network. The great advantage of quantum communication compared to classical communication is that it can be encrypted on a quantum level. This means, since the information sent through the communication channel has a quantum nature it will be altered when it is measured. Therefore, any eavesdropping on the communication channel would lead to a change of the transmitted information and therefore would be detectable [12]. However, due to losses in a communication channel at some point a signal has to be amplified. Due to the no-cloning theorem [13] it is not possible just to copy the quantum information and amplify it as it is done in classical amplifiers. In quantum communication this task is done by a quantum repeater [14] that makes it possible to realize long-distance quantum communication [15]. Such a quantum repeater could be realized by a light-matter interface.

A possible realization of hybrid quantum system as an atom–light interface lies in the efficient coupling of an ensemble of neutral atoms to the evanescent field of light that propagates in an optical nanofiber. An optical nanofiber can guide light fields like a standard fiber but has a sub-wavelength diameter. An interesting property of the nanofiber is that the guided light fields

are strongly confined. However, this property is not unique to nanofibers: Today there is a strong tendency to miniaturize physical systems either for its benefit for the computer industry or in order to find and study interesting physical effects. Especially in nanoscaled optical systems one always has to deal with strong confinement of light fields [16]. The properties of these fields are different from freely propagating collimated light beams: By applying the paraxial approximation [17] to the Maxwell equations freely propagating collimated beams are usually treated as plane waves that are purely transversely polarized. This approximation is valid in many physical systems. But out of the paraxial approximation a light field cannot be only transversely polarized but also has a longitudinal component [18, 19]. This longitudinal component of the electric field is $\pi/2$ phase shifted with respect to its transverse components [20]. The feature of non-transverse polarization of a light beam becomes more significant when it is strongly confined. Experimentally, the longitudinal component of at the waist of a focused light field has been measured, e.g., in [21]. There, single molecules with fixed absorption dipole orientation were used to probe the longitudinal component. In [22], it was even suggested to use focused light fields as laser particle accelerator where the particles are driven by the Lorentz force that is induced by the longitudinal component of the light field.

The occurrence of the longitudinal component is related to the spin–orbit interaction of light. It has been studied not only in free space [23–25] but also in other situations when a light field is, e.g., interacting with a plane dielectric interface [26,27] or a plane metasurface [28]. In the latter case it is experimentally shown that the spin–orbit interaction of light can lead to the “spin Hall effect” of light [29–32]. This effect describes the fact that the polarization components of a light beam are spatially separated into two parts that have opposite circularity. Nanofiber-guided light fields can locally exhibit these circular polarization components as well, even when the total spin angular momentum of the light field is zero. In [33] it was proposed that on interaction of such a light field with atoms it should thus be possible to spin-polarize the atoms. The interaction of single atoms with nonparaxial photons was investigated in a microscale whispering-gallery-mode resonator and presented in [34, 35]

It was proposed in [36,37] that it should be possible to trap atoms along an optical nanofiber and therefore create an interface between the nanofiber-guided modes and the atoms. This interface consists of a two-color dipole trap for neutral cesium atoms that is generated by the evanescent field of light that propagates in an optical nanofiber. One of the advantages of this system is the fact that the atoms are efficiently coupled to light that propagate in the optical nanofiber via the light’s evanescent field. Therefore, after interacting with the atoms the photons can still be easily routed over long distances. Here, we employ the fact that the nanofiber is realized as the waist of a tapered optical fiber: the light fields that propagate in a standard optical fiber can be efficiently routed into and out of the nanofiber section. The nanofiber-based trap was experimentally demonstrated for the first time in our group [38]. Then, we characterized this system [39, 40] in terms of atomic temperature, distribution of the atoms in the trap, scattering properties of atom, etc. We showed that the trapped atoms can dispersively interact with the nanofiber-guided light fields and that this is nondestructive with respect to the atom number [41]. Furthermore, we showed that we can manipulate the external degree of freedom of the trapped atoms by spatially moving them along the nanofiber [42]. Recently, we demonstrated that the “matter-part” of the system exhibits good ground state coherence times so that it should be

possible to store quantum information in the atoms for several milliseconds [43]. These results triggered both theoretical and experimental research on this topic by various research teams, e.g. [44–49].

In this thesis, the studies of this system of nanofiber-trapped atoms is extended. I investigate the unique polarization pattern that is exhibited by the spin–orbit coupled nanofiber-guided light fields. I then demonstrate that the internal state of the atoms can be manipulated via these fields. In particular, experimental results are presented that show that the trapped atomic ensemble can be polarized upon interaction with a nanofiber-guided light field that possesses a total spin angular momentum of zero [50]. Moreover, it is demonstrated that, based on spin–orbit coupling, this system can serve as a directional nanophotonic atom–waveguide interface. Here, I show that the rate of photons emitted by the trapped atoms into counter-propagating nanofiber-guided modes can be strongly asymmetric [51]. Furthermore, I demonstrate that our system can be strongly nonreciprocal in terms of the transmission of a nanofiber-guided light field.

This work is structured in the following way: In chapter 2, the concept of light propagation in optical fibers with a sub-wavelength diameter, so-called optical nanofibers will be studied. In this chapter, the mode profile functions of the fundamental mode propagating in these nanofibers are derived. I will show the spin–orbit interaction of these light fields and discuss the resulting peculiar polarization properties. Chapter 3 is then focused on the dispersive interaction of light and matter. Here, I will discuss how the optical two-color dipole trap can be realized via the Stark interaction between nanofiber-guided light fields and neutral cesium atoms. After that, I will present the experimental realization of a nanofiber-based two-color dipole trap for neutral cesium atoms in chapter 4 and characterize the trapped atoms. In chapter 5, it is shown how the internal state of the trapped atoms can be manipulated by making use of the features of the non-paraxial guided light fields. In particular, I will show that the atomic ensemble can be optically pumped by the fiber-guided light fields. In chapter 6, the directional incoupling of photons that have been emitted by the trapped atoms is demonstrated. Furthermore, it is shown that, under certain conditions, our system can exhibit a nonreciprocal behavior and that this can be used to realize a nanoscale optical diode.

Optical nanofibers

The principle of guiding light in glass fibers is based on total internal reflection. The light inside a fiber is reflected at the interface between the glass and the surrounding medium, if the refractive index of the surrounding medium is lower than the one of glass. The first optical fibers were bare glass fibers and did not transmit light very well. The problem was that due to the presence of the evanescent field outside the fiber, light could easily be lost by scattering at defects or pollution at the fiber's surface. This problem was solved by cladding the fiber with a material with a slightly lower index of refraction than the one of the glass core. Thus, the evanescent field is no longer accessible from the outside and the guided light is "protected". The optical properties of the fibers were improved but, since the attenuation due to impurities in the glass was as high as ≈ 1000 dB/km, they were still not useful for guiding light over long distances [52]. Charles K. Kao, one of the pioneers in optical fiber technology, who was awarded with the Nobel Prize in Physics in 2009 "*for groundbreaking achievements concerning the transmission of light in fibers for optical communication*" [53], paved the way for the vast usage of optical fibers for optical data transmission. Thanks to his work and the work of his colleagues the attenuation in optical fibers could be reduced to only 0.2 dB/km for wavelengths in the telecommunication band, making them attractive for broadband and long-range communication. Today, optical fibers form the backbone of our worldwide communication network used for example for internet connections across continents and oceans.

In this chapter, I will first describe the modes of an electromagnetic field that is guided in an optical fiber. The trapping and interfacing of neutral atoms with optical fibers takes place in the evanescent part of the guided light field. Therefore, in the following section, I will focus on this evanescent part with a close look at the polarization properties of the electric field. In the next section I will provide an alternative description of the local polarization properties in terms of spin-orbit interaction. In order to bring atoms so close to the fiber, that they can interact with the evanescent field of a guided mode, we have to remove the cladding of the fiber without deteriorating its transmission. Optical nanofibers can guide modes that possess a strong and accessible evanescent field and still have a high transmission. The fabrication of optical nanofibers is discussed in the last section.

2.1 Modes guided by an optical fiber

The propagation of light in optical fibers has been thoroughly studied in the literature [54, 55]. The derivation given here closely follows the one given by Yariv [55]. In this section, we derive the electromagnetic field that propagates through an optical step index fiber with circular cross section. At the end of the section I will present an expression for the evanescent field of the fundamental mode that is guided by an optical nanofiber.

2.1.1 Wave equations for a circular waveguide

Let us consider a waveguide in form of an optical fiber that is cylindrically symmetric, i.e., its refractive index $n(r)$ only depends on the radial direction. In this case, it is convenient to write the electromagnetic field in cylindrical coordinates. The electric and the magnetic fields that propagate inside an optical fiber can be expressed by

$$\mathbf{E}(\mathbf{r}, t) = \mathbf{E}(r, \varphi) \exp[i(\omega t - \beta z)] \quad \text{and} \quad \mathbf{H}(\mathbf{r}, t) = \mathbf{H}(r, \varphi) \exp[i(\omega t - \beta z)], \quad (2.1)$$

where ω is the angular frequency and t is the time. The value of the propagation constant β will be determined later. Here, it is assumed that the wave propagates along the fiber axis, which is defined as the z axis. The wave equation for the electric field that can be derived from Maxwell's equations reads

$$\nabla^2 \mathbf{E} - \mu \epsilon \frac{\partial^2 \mathbf{E}}{\partial t^2} = -\nabla \left(\frac{1}{\epsilon} \mathbf{E} \cdot \nabla \epsilon \right), \quad (2.2)$$

where μ denotes the permeability and ϵ the permittivity of the material. The Laplace operator ∇^2 is given by

$$\nabla^2 = \frac{\partial^2}{\partial r^2} + \frac{1}{r} \frac{\partial}{\partial r} + \frac{1}{r^2} \frac{\partial^2}{\partial \varphi^2} + \frac{\partial^2}{\partial z^2}.$$

Using the Maxwell's equations that interconnect the electric and magnetic fields we can express the transverse components E_r , E_φ , H_r , and H_φ of the electric and magnetic field stated in equation (2.1) in terms of the longitudinal components E_z and H_z :

$$\begin{aligned} E_r &= \frac{-i\beta}{\omega^2 \mu \epsilon - \beta^2} \left(\partial_r E_z + \frac{\omega \mu}{\beta} \frac{1}{r} \partial_\varphi H_z \right) \\ E_\varphi &= \frac{-i\beta}{\omega^2 \mu \epsilon - \beta^2} \left(\frac{1}{r} \partial_\varphi E_z - \frac{\omega \mu}{\beta} \partial_r H_z \right) \end{aligned} \quad (2.3)$$

$$\begin{aligned} H_r &= \frac{-i\beta}{\omega^2 \mu \epsilon - \beta^2} \left(\partial_r H_z - \frac{\omega \epsilon}{\beta} \frac{1}{r} \partial_\varphi E_z \right) \\ H_\varphi &= \frac{-i\beta}{\omega^2 \mu \epsilon - \beta^2} \left(\frac{1}{r} \partial_\varphi H_z + \frac{\omega \epsilon}{\beta} \partial_r E_z \right). \end{aligned} \quad (2.4)$$

Here, the abbreviation $\partial_x = \frac{\partial}{\partial x}$ was used. These relations show that it is sufficient to solve the wave equation for the longitudinal components E_z and H_z , only. The transverse components can then be calculated directly from Eq. (2.3) and (2.4). Assuming that the fractional change of the permittivity ϵ of the material over one optical wavelength is very small, the wave Eq. (2.2)

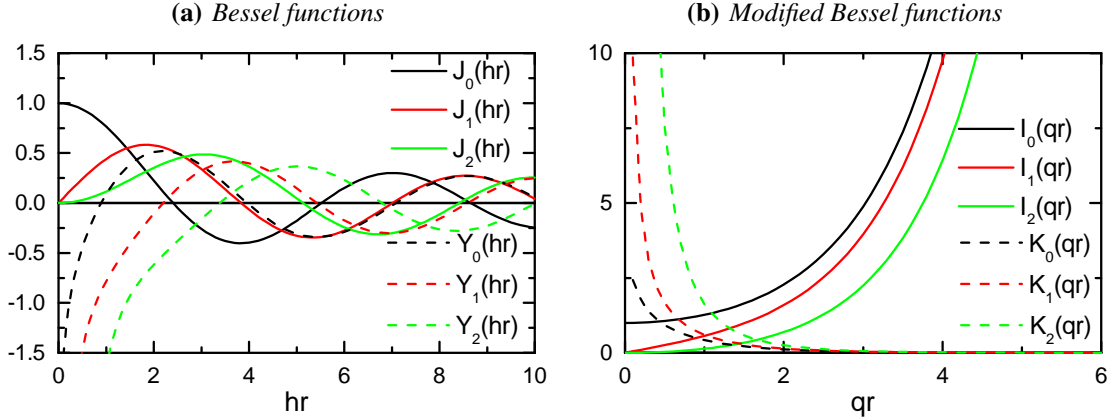


Figure 2.1: The Bessel functions $J_l(x)$ and $Y_l(x)$ of order $l = 0, 1, 2$ are plotted in (a). The modified Bessel functions $I_l(x)$ and $K_l(x)$ of the same order are shown in (b).

can be simplified by neglecting the right hand side. In combination with (2.1) we then get for the longitudinal components

$$\left[\partial_r^2 + \frac{1}{r} \partial_r + \frac{1}{r^2} \partial_\varphi^2 + (k^2 - \beta^2) \right] \begin{bmatrix} E_z(\mathbf{r}, t) \\ H_z(\mathbf{r}, t) \end{bmatrix} = 0, \quad (2.5)$$

where $k = \omega n/c_0$ is the wavenumber and c_0 the speed of light in vacuum. This equation is separable in the variables r and φ . The solutions take the following form:

$$\begin{bmatrix} E_z(r, \varphi) \\ H_z(r, \varphi) \end{bmatrix} = \psi(r) \exp(\pm i l \varphi), \quad \text{with } l = 0, 1, 2, \dots \quad (2.6)$$

The physical meaning of l is similar to the quantum number describing the orbital angular momentum of an electron in an azimuthally symmetric potential [55]. Therefore, the sign of the exponent can be understood as a “circulation” of the photons around the z axis, where the “+” sign would corresponds to clockwise “circulation” and “-” sign to counter-clockwise “circulation”. With this ansatz, Eq. (2.5) can be rewritten as:

$$\left[\partial_r^2 + \frac{1}{r} \partial_r + (k^2 - \beta^2 - \frac{l^2}{r^2}) \right] \begin{bmatrix} E_z(r, t) \\ H_z(r, t) \end{bmatrix} = 0. \quad (2.7)$$

This equation corresponds to the Bessel differential equation, where the solutions are called Bessel functions of order l . For solving the Bessel differential equation, one has to consider two different cases:

- For $k^2 - \beta^2 > 0$ the general solution of the equation above is

$$\psi(r) = c_1 J_l(hr) + c_2 Y_l(hr), \quad (2.8)$$

with c_1 and c_2 being constants that will be determined in the next section. Furthermore, $h^2 = k^2 - \beta^2$, and J_l and Y_l being the Bessel functions of the first and second kind of the order l , respectively.

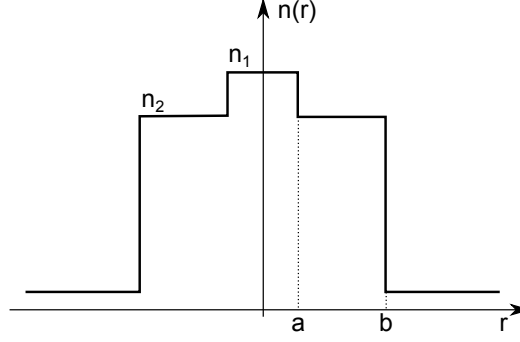


Figure 2.2: The sketch shows the profile of the refractive index $n(r)$ as a function of distance r from the center of the fiber of a step index circular waveguide. Here, n_1 and n_2 are the index of refraction of the core and the cladding material, respectively. The radius of the core is denoted by a and the radius of the cladding by b .

- For the case of $k^2 - \beta^2 < 0$ the general solution is given by the modified Bessel functions I_l and K_l of the first and second kind of the order l , respectively

$$\psi(r) = d_1 I_l(qr) + d_2 K_l(qr), \quad (2.9)$$

with $q^2 = \beta^2 - k^2$ and d_1 and d_2 being constants that will be determined in the next section.

In figure 2.1 the Bessel functions and the modified Bessel functions are plotted for different orders l . The Bessel functions plotted in Fig. 2.1 (a) show a strong oscillatory behavior, in addition the Bessel functions of the second kind Y_l diverge for $hr \rightarrow 0$. The modified Bessel functions of the first and of the second kind shown in (b) diverge for $qr \rightarrow \infty$ and $qr \rightarrow 0$, respectively.

2.1.2 A step-index circular waveguide

In the following, we will see how to determine the values for the constants c_1 and c_2 given in Eq. (2.8) and d_1 and d_2 given in Eq. (2.9). To describe the radial behavior of E_z and H_z guided by an optical fiber one has to consider the radial dependency of the refractive index $n(r)$. In Fig. 2.2 $n(r)$ is sketched for a step-index circular waveguide. The radius of the core of the fiber is a and the radius of the cladding is b . We take the radius b to be very large, so that the electromagnetic field at b is basically zero. The refractive index of the core is denoted n_1 and the refractive index of the cladding is denoted n_2 .

In order to have a transversely confined mode, the propagation constant β has to be smaller than the propagation constant of a plane wave traveling in the core and bigger than the one of a plane wave traveling in the cladding, i.e., $n_1 k_0 > \beta > n_2 k_0$ (with $k_0 = \omega/c$). Therefore, to describe the fields inside the core ($r < a$), where $n_1 k_0 > \beta$ we have to use Eq. (2.8):

$$\begin{bmatrix} E_z(\mathbf{r}, t) \\ H_z(\mathbf{r}, t) \end{bmatrix} = \begin{bmatrix} A \\ B \end{bmatrix} [J_l(hr) \exp(i(\omega t \pm l\varphi - \beta z))] \quad (2.10)$$

with $h^2 = n_1^2 k_0^2 - \beta^2$. The constant c_1 from Eq. (2.8) is replaced by A and B . These complex constants will be determined later. Note that in Eq. (2.10) the constant c_2 in Eq. (2.8) has been set to zero to ensure that the fields are not diverging for $hr \ll 1$.

For the fields outside the core ($r > a$) the propagation constant must fulfill $\beta > n_2 k_0$ and we therefore have to use Eq. (2.9) and get:

$$\begin{bmatrix} E_z(\mathbf{r}, t) \\ H_z(\mathbf{r}, t) \end{bmatrix} = \begin{bmatrix} C \\ D \end{bmatrix} [K_l(qr) \exp(i(\omega t \pm l\varphi - \beta z))], \quad (2.11)$$

with $q^2 = \beta^2 - n_2^2 k_0^2$. The constant d_2 from Eq. (2.9) is replaced by C and D . Also these complex constants that will be determined later. Here the constant d_1 is set to zero to prevent a diverging behavior for $qr \rightarrow \infty$.

Using the results that are given in Eq. (2.10) and (2.11) for the z component of the electric and magnetic field, we calculate the other components via Eq. (2.3) and (2.4). For the core region ($r < a$) this leads to

$$\begin{aligned} E_r &= \frac{-i\beta}{h^2} \left[AhJ_l'(hr) + \frac{i\omega\mu(\pm l)}{\beta r} BJ_l(hr) \right] \exp[i(\omega t \pm l\varphi - \beta z)] \\ E_\varphi &= \frac{-i\beta}{h^2} \left[\frac{i(\pm l)}{r} AJ_l(hr) - \frac{\omega\mu}{\beta} BhJ_l'(hr) \right] \exp[i(\omega t \pm l\varphi - \beta z)] \\ E_z &= AJ_l(hr) \exp[i(\omega t \pm l\varphi - \beta z)] \end{aligned} \quad (2.12)$$

$$\begin{aligned} H_r &= \frac{-i\beta}{h^2} \left[BhJ_l'(hr) - \frac{i\omega\epsilon n_1(\pm l)}{\beta r} AJ_l(hr) \right] \exp[i(\omega t \pm l\varphi - \beta z)] \\ H_\varphi &= \frac{-i\beta}{h^2} \left[\frac{i(\pm l)}{r} BJ_l(hr) + \frac{\omega\epsilon n_1}{\beta} AhJ_l'(hr) \right] \exp[i(\omega t \pm l\varphi - \beta z)] \\ H_z &= BJ_l(hr) \exp[i(\omega t \pm l\varphi - \beta z)]. \end{aligned} \quad (2.13)$$

In these equations, the derivative of the Bessel functions is denoted $J_l'(x) = dJ_l(x)/dx$. Outside the core region ($r > a$) the fields have the following form:

$$\begin{aligned} E_r &= \frac{i\beta}{q^2} \left[CqK_l'(qr) + \frac{i\omega\mu(\pm l)}{\beta r} DK_l(qr) \right] \exp[i(\omega t \pm l\varphi - \beta z)] \\ E_\varphi &= \frac{i\beta}{q^2} \left[\frac{i(\pm l)}{r} CK_l(qr) - \frac{\omega\mu}{\beta} DqK_l'(qr) \right] \exp[i(\omega t \pm l\varphi - \beta z)] \\ E_z &= CK_l(qr) \exp[i(\omega t \pm l\varphi - \beta z)] \end{aligned} \quad (2.14)$$

$$\begin{aligned} H_r &= \frac{i\beta}{q^2} \left[DqK_l'(qr) - \frac{i\omega\epsilon n_2(\pm l)}{\beta r} CK_l(qr) \right] \exp[i(\omega t \pm l\varphi - \beta z)] \\ H_\varphi &= \frac{i\beta}{q^2} \left[\frac{i(\pm l)}{r} DK_l(qr) + \frac{\omega\epsilon n_2}{\beta} CqK_l'(qr) \right] \exp[i(\omega t \pm l\varphi - \beta z)] \\ H_z &= DK_l(qr) \exp[i(\omega t \pm l\varphi - \beta z)]. \end{aligned} \quad (2.15)$$

To determine the coefficients A , B , C , and D , the boundary conditions for the fields have to be considered: the components that are parallel to the dielectric interface between n_1 and n_2 (e.g.

E_φ , E_z , H_φ , and H_z) have to be continuous at this position ($r = a$) [56]. With this requirement four continuity equations can be derived from Eqs. (2.12)- (2.15) that yield a nontrivial solution for A , B , C , and D . With this solution, a mode condition that determines the propagation constant β can be formulated [55]

$$\begin{aligned} \frac{J'_l(ha)}{haJ_l(ha)} = & - \left(\frac{n_1^2 + n_2^2}{2n_1^2} \right) \frac{K'_l(qa)}{qaK_l(qa)} \\ & \pm \left[\left(\frac{n_1^2 - n_2^2}{2n_1^2} \right)^2 \left(\frac{K'_l(qa)}{qaK_l(qa)} \right)^2 + \frac{l^2}{n_1^2} \left(\frac{\beta}{k_0} \right)^2 \left(\left(\frac{1}{qa} \right)^2 + \left(\frac{1}{ha} \right)^2 \right)^2 \right]^{1/2}. \end{aligned} \quad (2.16)$$

We also get the constraints:

$$\begin{aligned} \frac{C}{A} &= \frac{2\beta}{q} \\ \frac{B}{A} &= \frac{i2ql}{\omega\mu} \frac{K_l(qa)}{J_l(ha)} \left(\frac{1}{q^2a^2} + \frac{1}{h^2a^2} \right) \left(\frac{J'_l(ha)}{haJ_l(ha)} + \frac{K'_l(qa)}{qaK_l(qa)} \right)^{-1} \\ \frac{D}{A} &= \frac{J_l(ha)}{K_l(qa)} \frac{B}{A}. \end{aligned} \quad (2.17)$$

Thus, the quantities B , C , and D can be expressed in dependency of A . The parameter A physically plays the role of the amplitude of the electromagnetic field. Its explicit relation to the optical power that is guided in the mode will be stated in the next section.

The two equations for the determination of β given by the \pm sign in Eq. (2.16) can be rewritten and are typically designated as the EH and the HE modes. These so-called hybrid modes have, in general, nonvanishing r , ϕ , and z components of the electric and magnetic field. The mode equations read:

$$\text{EH mode:} \quad \frac{J_{l+1}(ha)}{haJ_l(ha)} = \frac{n_1^2 + n_2^2}{2n_1^2} \frac{K'_l(qa)}{qaK_l(qa)} + \left(\frac{l}{(ha)^2} - R \right) \quad (2.18)$$

$$\text{HE mode:} \quad \frac{J_{l-1}(ha)}{haJ_l(ha)} = -\frac{n_1^2 + n_2^2}{2n_1^2} \frac{K'_l(qa)}{qaK_l(qa)} + \left(\frac{l}{(ha)^2} - R \right) \quad (2.19)$$

with

$$R = \left[\left(\frac{n_1^2 - n_2^2}{2n_1^2} \right)^2 \left(\frac{K'_l(qa)}{qaK_l(qa)} \right)^2 + \left(\frac{l\beta}{n_1k_0} \right)^2 \left(\frac{1}{(qa)^2} + \frac{1}{(ha)^2} \right)^2 \right]^{1/2}. \quad (2.20)$$

These equations are transcendental and can be either solved numerically or graphically. Let us consider $l > 0$. For the graphical solution both sides of the Eq. (2.18) and (2.19) are plotted as a function of ha in Fig. 2.3. In this context, the V -parameter is used to express (qa) via the relation $(qa)^2 = V^2 - (ha)^2$. The V -parameter or normalized frequency is defined as $V = ak_0\sqrt{n_1^2 - n_2^2}$. It is a property of the waveguide and sets, for a given wavelength, a limit to the number of guided modes that can exist, as it can be seen in Fig. 2.3. With the value $(ha)_{\text{cross}}$,

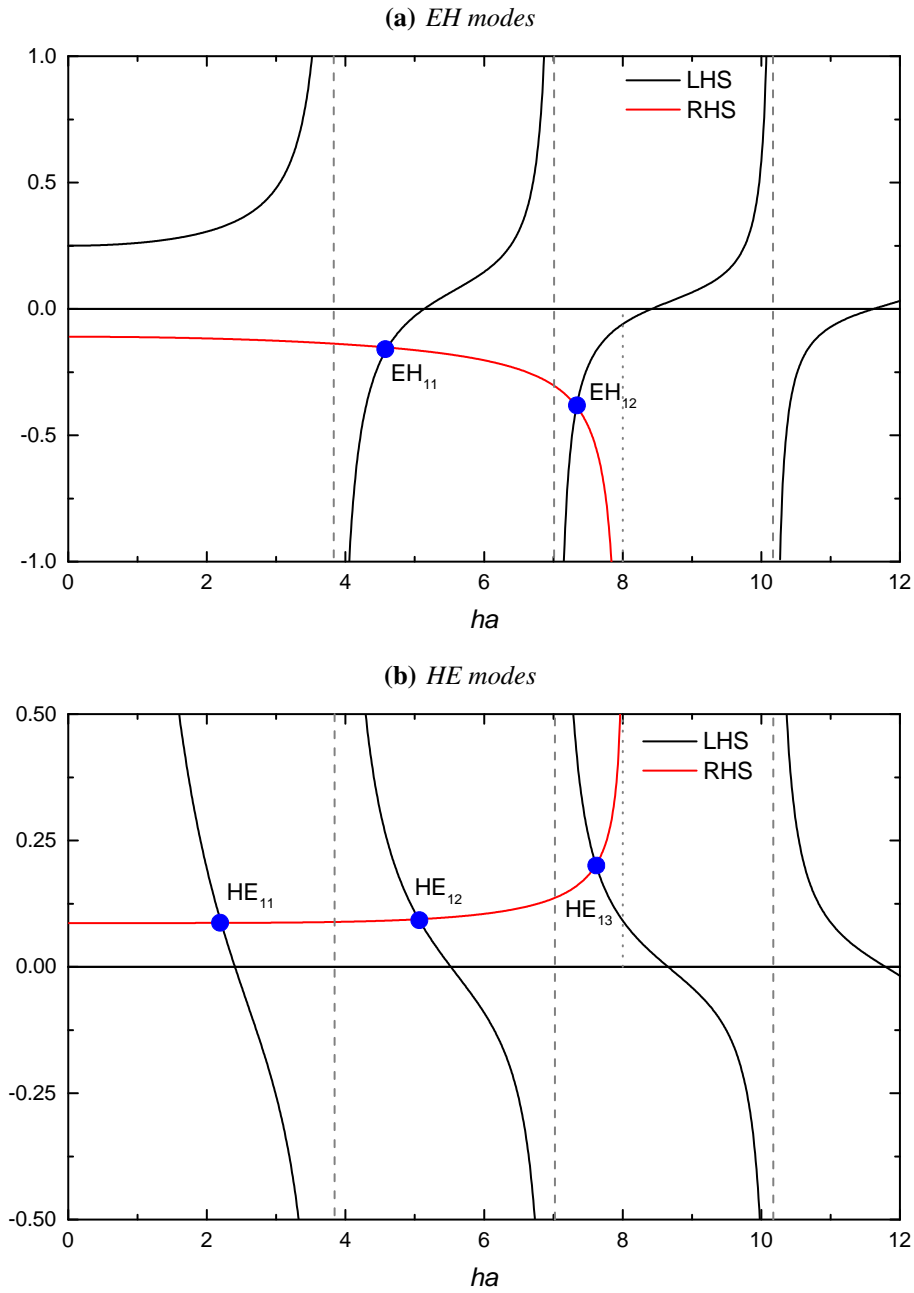


Figure 2.3: Graphical method for the determination of the propagation constant β for **(a)** the EH modes and **(b)** the HE modes, with the parameters $l = 1$, $n_1 = 1.45$, $n_2 = 1$, and $V = 8$. In the plots the value of V is indicated by the dotted line. The intersection point of the left hand side (LHS) and the right hand side (RHS) of the mode equations (2.18) and (2.19) are marked with blue dots and labeled with the name of the corresponding mode.

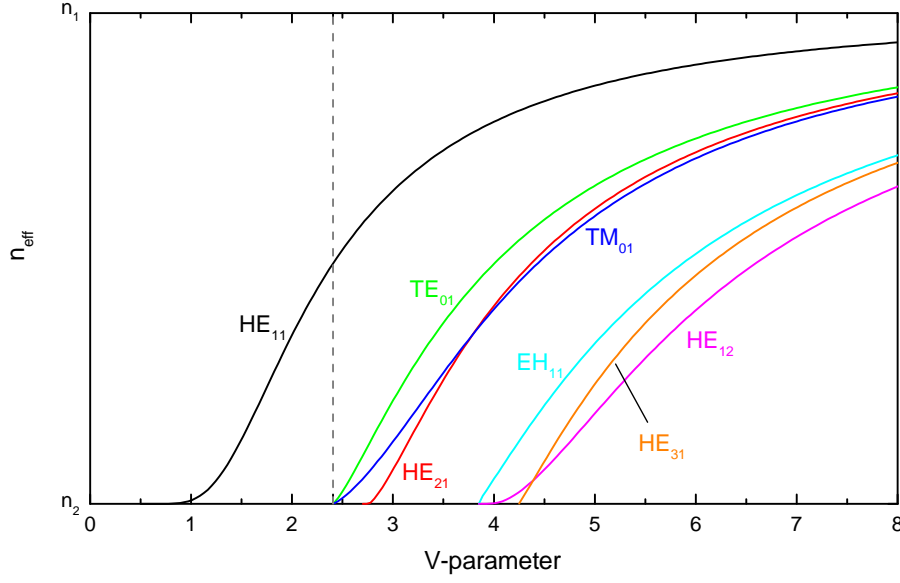


Figure 2.4: Effective refractive index as a function of the V -parameter for a few of the lowest order modes of a step index fiber with the following parameters: $n_1 = 1.45$, $n_2 = 1$, and $\lambda = 852$ nm. The dashed line shows $V = 2.405$, separating the regimes of single and multi mode operation.

where the left-hand-side (LHS) and the right-hand-side (RHS) of the mode equations (2.18) and (2.19) intersect, the propagation constant can be determined by

$$\beta = \sqrt{n_1^2 k_0^2 - \left(\frac{(ha)_{\text{cross}}}{a} \right)^2}. \quad (2.21)$$

For the special case of $l = 0$ solutions for the mode equations (2.18) and (2.19) exist, where all the field components are radially symmetric. For the solutions of Eq. (2.18) the only non-vanishing field components are H_r , H_z , and E_φ and therefore is called transversely electric (TE_{0m}), where the first subscript stands for $l = 0$ and the second for the different mode solutions $m = 1, 2, 3, \dots$. For the solutions of Eq. (2.19) the nonvanishing field components are E_r , E_z , and H_φ and according to this is called transversely magnetic (TM_{0m}).

For many applications it is interesting to know the propagation constant β as a function of the wavelength λ of the light that is sent into a fiber. In Fig. 2.4 the mode index defined as $n_{\text{eff}} = \beta/k_0$ is plotted as a function of the V -parameter. We can see from this graph that the number of possible guided modes crucially depends on V . Furthermore, we can identify the fundamental mode to be the HE_{11} mode, since this is the only mode that does not have a cut-off frequency and that is therefore always guided. Thus, single mode operation can be guaranteed for $V < 2.405$.

2.1.3 The fundamental mode for nanofibers

The optical nanofiber that is used in the experiments discussed in this thesis was fabricated from a standard optical fiber (see section 2.4). It has a diameter of 500 nm to provide a strong evanescent field [57]. The refractive index of the core is the one of fused silica ($n_1 = 1.4525$) and the refractive index of the cladding is the one of vacuum ($n_2 = 1$). It thus corresponds to a step index fiber and the previously derived results can be applied. With these parameters, the nanofiber only guides the fundamental HE_{11} mode for all the light fields that will be used here.

In this section, the notations stated in the publications by Fam Le Kien et al. [58, 59] are used. The only free parameter left to fully describe the electric field of the fundamental mode is the fields amplitude A (see Eq. (2.17)). In order to determine A its relation to the cycle-averaged Poynting vector $\mathcal{P} = 1/2 \cdot \text{Re}(\mathbf{E} \times \mathbf{H}^*)$ can be used. The power flow along the fiber is given by

$$P = \int_0^\infty \int_0^{2\pi} \mathcal{P}_z \, dr \, d\varphi, \quad (2.22)$$

where the total power P is the sum of the power inside and outside the core $P = P_z^{\text{in}} + P_z^{\text{out}}$. One finds [59]

$$A = \sqrt{\frac{P \beta}{\pi a^2 \omega \epsilon_0}} (D^{\text{in}} + D^{\text{out}})^{-1/2}, \quad (2.23)$$

where D^{in} and D^{out} are related to the fractions of power traveling inside and outside the core. They are given by

$$\begin{aligned} D^{\text{in}} &= n_1^2 \frac{q^2 K_1^2(qa)}{h^2 J_1^2(ha)} \left\{ (1-s)(1-s_1) [J_0^2(ha) + J_1^2(ha)] \right. \\ &\quad \left. + (1+s)(1+s_1) [J_2^2(ha) - J_1(ha)J_3(ha)] \right\}, \\ D^{\text{out}} &= n_2^2 \left\{ (1-s)(1-s_2) [K_1^2(qa) - K_0^2(qa)] \right. \\ &\quad \left. + (1+s)(1+s_2) [K_1(qa)K_3(qa) - K_2^2(qa)] \right\}, \end{aligned}$$

with

$$\begin{aligned} s &= \left(\frac{1}{q^2 a^2} + \frac{1}{h^2 a^2} \right) \left(\frac{J_1'(ha)}{ha J_1(ha)} + \frac{K_1'(qa)}{qa K_1(qa)} \right)^{-1} \\ s_1 &= \frac{\beta^2}{k_0^2 n_1^2} s \\ s_2 &= \frac{\beta^2}{k_0^2 n_2^2} s. \end{aligned}$$

With all these ingredients, one can finally write down the mode profile function $\mathbf{e}(\mathbf{r})$ and $\mathbf{h}(\mathbf{r})$ of the electric and the magnetic field of the fundamental quasi-circularly polarized HE_{11} mode [59].

- $r < a$

$$\begin{aligned}
 e_r &= i \frac{qK_1(qa)}{hJ_1(ha)} [(1-s)J_0(hr) - (1+s)J_2(hr)] \\
 e_\varphi &= -\frac{qK_1(qa)}{hJ_1(ha)} [(1-s)J_0(hr) + (1+s)J_2(hr)] \\
 e_z &= \frac{2q}{\beta} \frac{K_1(qa)}{J_1(ha)} J_1(hr)
 \end{aligned} \tag{2.24}$$

and

$$\begin{aligned}
 h_r &= \frac{\omega\epsilon_0 n_1^2 q}{\beta h} \frac{K_1(qa)}{J_1(ha)} [(1-s_1)J_0(hr) + (1+s_1)J_2(hr)] \\
 h_\varphi &= i \frac{\omega\epsilon_0 n_1^2 q}{\beta h} \frac{K_1(qa)}{J_1(ha)} [(1-s_1)J_0(hr) - (1+s_1)J_2(hr)] \\
 h_z &= i \frac{2q}{\omega\mu_0} s \frac{K_1(qa)}{J_1(ha)} J_1(hr)
 \end{aligned} \tag{2.25}$$

- $r > a$

$$\begin{aligned}
 e_r &= i [(1-s)K_0(qr) + (1+s)K_2(qr)] \\
 e_\varphi &= -[(1-s)K_0(qr) - (1+s)K_2(qr)] \\
 e_z &= \frac{2q}{\beta} K_1(qr)
 \end{aligned} \tag{2.26}$$

and

$$\begin{aligned}
 h_r &= \frac{\omega\epsilon_0 n_2^2}{\beta} [(1-s_2)K_0(qr) - (1+s_2)K_2(qr)] \\
 h_\varphi &= i \frac{\omega\epsilon_0 n_2^2}{\beta} [(1-s_2)K_0(qr) + (1+s_2)K_2(qr)] \\
 h_z &= i \frac{2q}{\omega\mu_0} s K_1(qr)
 \end{aligned} \tag{2.27}$$

The prefix ‘‘quasi’’ is added to underline the difference of these modes to freely propagating light fields due to the appearance of nonvanishing axial components. In order to distinguish the different modes we label them with $f = +, -$ that denotes propagation in $\pm z$ direction of the mode through the fiber, and $p = +, -$ that denotes counterclockwise or clockwise rotation of polarization, respectively [60]: $e_r^{(f,p)} = e_r$, $e_\varphi^{(f,p)} = p e_\varphi$, and $e_z^{(f,p)} = f e_z$ and $h_r^{(f,p)} = p h_r$, $h_\varphi^{(f,p)} = h_\varphi$, and $h_z^{(f,p)} = p f h_z$.

A linear superposition of equal weight of the quasi-circularly polarized light field yields so-called quasi-linearly polarized light, e.g., $1/\sqrt{2} (\mathbf{e}^{(f,+)} e^{i(\varphi-\phi_0)} + \mathbf{e}^{(f,-)} e^{-i(\varphi-\phi_0)})$. The electric and the magnetic field of the fundamental quasi-linearly polarized mode in cylindrical coordinates then are

$$\mathbf{E}^{\text{lin}}(r, \varphi, z) = A\sqrt{2} \begin{pmatrix} e_r \cos(\varphi - \phi_0) \\ i e_\varphi \sin(\varphi - \phi_0) \\ f e_z \cos(\varphi - \phi_0) \end{pmatrix} \cdot \exp[i f \beta z - i \omega t]. \tag{2.28}$$

and

$$\mathbf{H}^{\text{lin}}(r, \varphi, z) = A\sqrt{2} \begin{pmatrix} ih_r \sin(\varphi - \phi_0) \\ h_\varphi \cos(\varphi - \phi_0) \\ ifh_z \sin(\varphi - \phi_0) \end{pmatrix} \cdot \exp[if\beta z - i\omega t]. \quad (2.29)$$

Together with Eqs. (2.26) and (2.27), we can see that the z component and the transverse components (r and φ) are phase shifted by $\pm\pi/2$ for both the electric and the magnetic field. This leads to the fact that the evanescent field is locally elliptically polarized. This matter will further be discussed in the next section.

In Fig. 2.5 (a), the real part of the electric field outside the fiber is plotted in the x - y and x - z plane. For $\phi_0 = 0$, the transverse components of the electric field only point in the $\pm x$ direction, for $x = 0$ or $y = 0$. We will call this direction the main direction of polarization. Note that for $\phi_0 = \pi/2$, the main direction of polarization is along the $\pm y$ direction. The plot in Fig. 2.5 (a) reveals that for $x \neq 0$ and $y \neq 0$ the electric field has also a component that points along the y direction for $\phi_0 = 0$. In Fig. 2.5 (b) we can see that the quasi-linearly polarized light field exhibits a nonvanishing z component as well, which depends on the position z along the fiber.

In Fig. 2.5 (c), the intensity $\mathbf{E}^{\text{lin}} \cdot \mathbf{E}^{\text{lin}*}$ is plotted for the quasi-linearly polarized HE_{11} mode inside and outside of the nanofiber. The intensity is normalized to the maximal intensity that can be found for the parameters chosen here at the center of the fiber. The plot shows the discontinuity of the intensity at the surface of the fiber. Furthermore, the intensity exhibits a significant breaking of symmetry in the azimuthal direction: in the direction orthogonal to the main direction of polarization (i.e. the y axis) the intensity is reduced by a factor of 4.8 (at the fiber surface) with respect to the intensity along main direction of polarization (i.e. the x axis). The intensity of the evanescent field depends on the wavelength λ of the light field propagating inside the nanofiber and on the radius a of the latter. In Fig. 2.5 (d) the intensity for the quasi-linearly polarized HE_{11} mode on the surface of the nanofiber (at $x = a$ and $y = 0$ with $\phi_0 = 0$) is plotted as a function of the ratio a/λ . The intensity is normalized to its maximum value for $a/\lambda = 0.23$. This plot shows that the radius of the nanofiber has to be on the order of only few hundred nanometer in order to ensure that a large fraction of the power traveling through the nanofiber is guided in the evanescent field.

2.2 Polarization of the fundamental mode

When the interaction of light and atoms is studied, the polarization of the light field is of interest. Depending on the polarization of a resonant light field, different atomic transitions can be driven, i.e., only transitions where the total angular momentum is conserved are allowed. Thus, a convenient way to express the electric field is in terms of spherical tensor components [61]. In this system the three basis vectors \mathbf{e}_{-1} , \mathbf{e}_0 , and \mathbf{e}_{+1} describe the part of the light that is σ^- , π , and σ^+ -polarized, respectively. In the experiments described here, an external magnetic field can be applied along the y axis. Therefore, without loss of generality, the quantization axis is chosen to be along the y axis. The transformation for the basis vectors from Cartesian coordinate

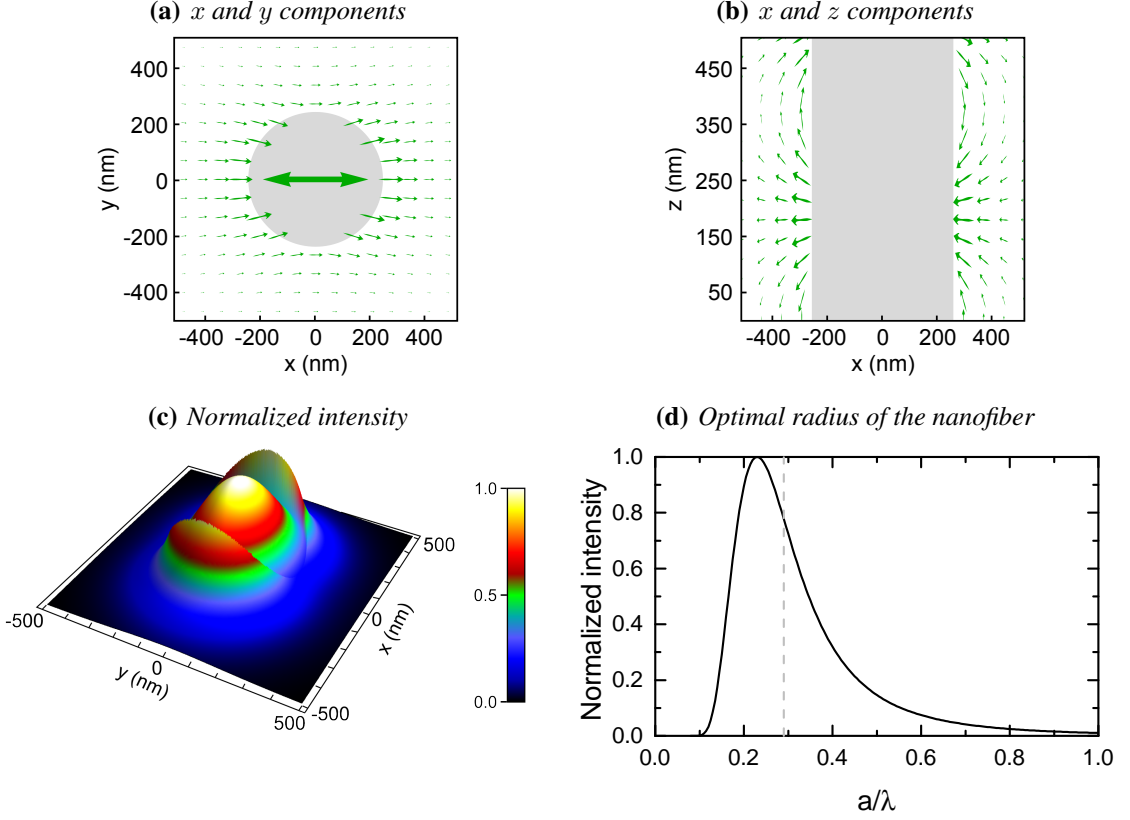


Figure 2.5: (a) Real part of the electric field of the HE_{11} mode outside the nanofiber at a fixed time. The gray area represents a cut through the nanofiber with a radius $a = 250$ nm, and the big green double arrow indicates the main direction of polarization. In (b) the real part of the electric field for a cut in the x - z plane is plotted while the main axis of polarization is still along the x axis. In (c) the normalized intensity of the quasi-linearly polarized fundamental mode is plotted. Note that the intensity is not continuous at the surface of the fiber ($r = 250$ nm). The parameters for the plots are: $a = 250$ nm, $\lambda = 852$ nm, $n_1 = 1.4525$, $n_2 = 1$, and $f = \pm 1$. (d) Intensity at the surface of the nanofiber depending on the ratio a/λ of the radius of the nanofiber and the wavelength of the guided light field. The intensity is normalized to its maximal value at 0.23. The dashed line shows the intensity at $a/\lambda = 0.29$ that is for $a = 250$ nm and $\lambda = 852$ nm.

system to the spherical tensor components then reads [59]

$$\mathbf{e}_{-1} = \frac{1}{\sqrt{2}}(\mathbf{e}_z - i\mathbf{e}_x), \quad \mathbf{e}_0 = \mathbf{e}_y, \quad \mathbf{e}_{+1} = -\frac{1}{\sqrt{2}}(\mathbf{e}_z + i\mathbf{e}_x), \quad (2.30)$$

The positive frequency envelope \mathcal{E} of the electric field can be expanded like any arbitrary vector in terms of the spherical tensor components to

$$\mathcal{E} = \sum_q (-1)^q \mathcal{E}_q \mathbf{e}_{-q}, \quad \text{with } q = -1, 0, +1 \quad (2.31)$$

where

$$\mathcal{E}_{-1} = \frac{1}{\sqrt{2}} (\mathcal{E}_z - i\mathcal{E}_x) , \quad \mathcal{E}_0 = \mathcal{E}_y , \quad \mathcal{E}_{+1} = -\frac{1}{\sqrt{2}} (\mathcal{E}_z + i\mathcal{E}_x) . \quad (2.32)$$

Note that then the spherical tensor components of the electric field \mathcal{E}_{-1} , \mathcal{E}_0 , and \mathcal{E}_{+1} represent σ^+ , π , and σ^- -polarized light, respectively.

In Fig. 2.6, the electric field in terms of the spherical tensor components is plotted. The plots in the left column show the fraction of σ^+ , σ^- , and π polarization for a quasi-linearly polarized light field with its main direction of polarization along the x axis. The first plot in the left column shows the fraction of σ^- -polarized light for a mode propagating in the positive z direction ($f = 1$). This is denoted by the label $\{+z, \sigma^-\}$. It is apparent that the light of the evanescent field for this mode is almost completely σ^- -polarized along the $-x$ axis. At the surface of the fiber, at $y = 0$ and $x = -250$ nm, 93 % of the light is σ^- -polarized. On the lowest plot in the left column, the fraction of σ^+ polarization for the same mode is plotted $\{+z, \sigma^+\}$. Here, we can see that the light is almost fully σ^+ -polarized along the $+x$ axis (for $y = 0$). Along the y axis for $x = 0$ the light consists of equal parts of σ^+ and σ^- polarization and is therefore linearly polarized.

When the mode propagates in the $-z$ direction the circularity changes its sign: the light at $x < 0$ that is almost fully σ^- -polarized for propagation of the mode in the $+z$ direction, is almost fully σ^+ -polarized for a propagation of the mode in the $-z$ direction. This is denoted by the labels on the plots which signify that, e.g., the upper plot in the left column shows $\{+z, \sigma^-\}$ and $\{-z, \sigma^+\}$.

The fraction of π polarization for this mode is shown in the plot in the center of the left column. Along the x and along the y axis, there is strictly no π -polarized light. On the surface of the fiber at the angles 56° , 124° , 236° , and 304° , this mode exhibits a maximum fraction of π polarization of only 8 %. Note that the fraction of π polarization is independent of the propagation direction of the light field.

The plots in the right column of Fig. 2.6 show the same polarization components but for quasi-linearly polarized light field with its main direction of polarization along the y axis. In this configuration, the light outside the nanofiber is almost completely π -polarized with a maximum of 100 % along the x axis as it is shown in the center plot. Along the y axis, the minimal fraction of π polarization on the surface is still almost 73 %. Again, the π polarization does not change when the propagation direction is changed from $+z$ to $-z$. The fraction of σ^+ and σ^- polarization for this mode is overall very weak and strictly zero for $y = 0$.

2.3 Spin-orbit interaction

In this section, I will present an alternative way to describe the local polarization of the evanescent field of nanofiber-guided light. As discussed in the previous section, the local polarization depends on both the position in the plane perpendicular to the fiber axis and on the direction of propagation of the field along the fiber. This physical situation can be explained in terms of spin-orbit interaction (SOI) of light. For light that exhibits SOI, spin angular momentum and the orbital angular momentum are no longer independent physical quantities.

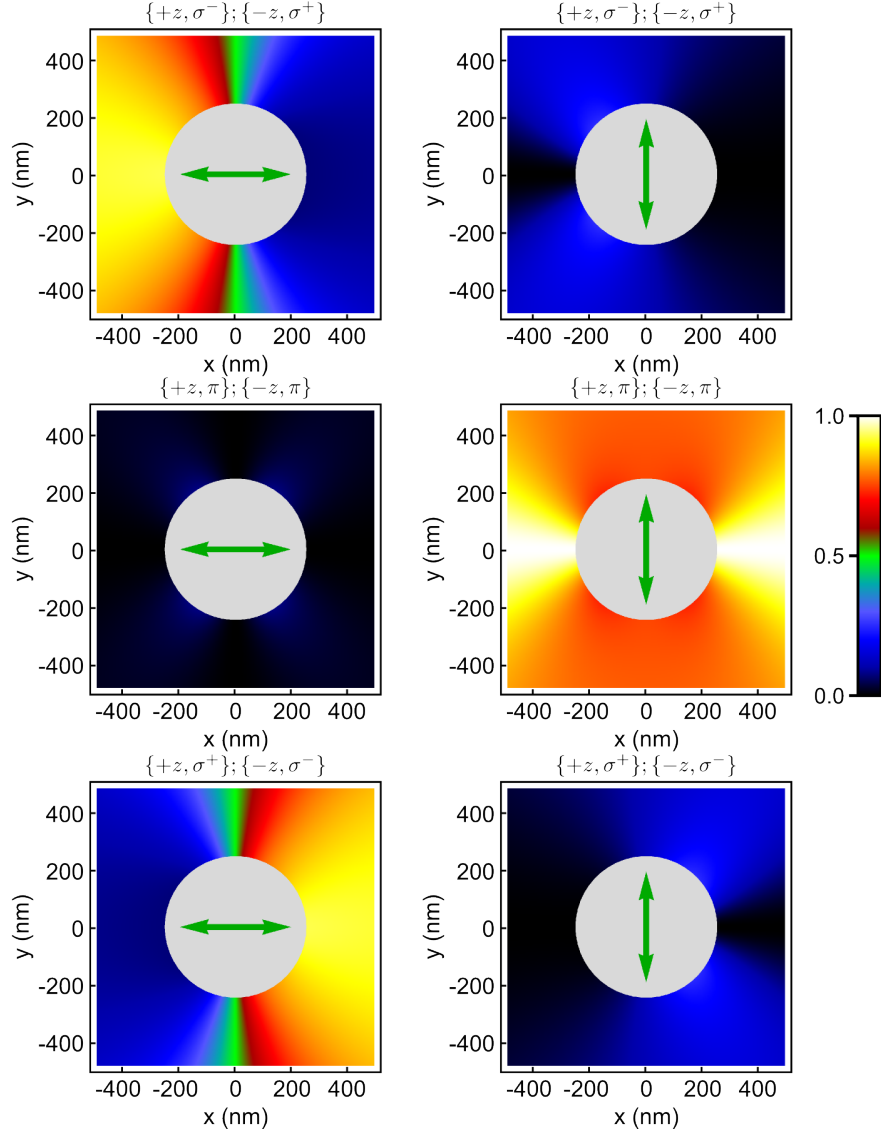


Figure 2.6: The square of the spherical tensor components \mathcal{E}_{-1} , \mathcal{E}_0 , and \mathcal{E}_{+1} are displayed normalized to \mathcal{E}^2 . The main direction of polarization of the quasi-linearly polarized light field is the x axis for the left column and the y axis for the right column, as indicated by the big green double arrow. The following parameters were used for the calculations: $a = 250$ nm, $\lambda = 852$ nm, $n_1 = 1.4525$, and $n_2 = 1$. The quantization axis is chosen to be along the y axis.

A good overview on “spin–orbit interactions of light in isotropic media” is given in a review article in [32]. SOI phenomena occur essentially in all modern optical applications dealing with subwavelength scales, e.g., photonics, plasmonics, nano-optics etc.

In order to describe the SOI of nanofiber-guided light fields, the Poynting vector and the

angular momentum of the fundamental quasi-linearly polarized HE_{11} mode are analyzed in this section. Furthermore, I will look at their local spin and orbital components in the evanescent field in the plane transverse to the nanofiber axis. The second part of this section, is focused on how to increase the spin–orbit coupling of the evanescent field for the nanofiber-guided modes.

2.3.1 Poynting vector and angular momentum density

An important characteristic of a light field is the cycle-averaged Poynting vector [56]

$$\mathcal{P} = \frac{1}{2} \text{Re} [\mathcal{E} \times \mathcal{H}^*]. \quad (2.33)$$

Here, we represent the electric and magnetic component of the field as $\mathbf{E} = 1/2(\mathcal{E}e^{-i\omega t} + \mathcal{E}^*e^{i\omega t})$ and $\mathbf{H} = 1/2(\mathcal{H}e^{-i\omega t} + \mathcal{H}^*e^{i\omega t})$, respectively, where \mathcal{E} and \mathcal{H} are the complex field amplitudes. The Poynting vector describes the energy flux density of the light field. Furthermore, it is directly related to the momentum density $\mathbf{p} = 1/c^2 \cdot \mathcal{P}$. According to [62], the momentum density can be decomposed into two parts – the orbital momentum density and the spin momentum density: $\mathbf{p} = \mathbf{p}^{\text{orb}} + \mathbf{p}^{\text{spin}}$. When we apply such a decomposition to the Poynting vector, we obtain [62, 63]

$$\mathcal{P}^{\text{orb}} = \frac{c}{4k} \text{Im} [\epsilon_0 \mathcal{E}^* \cdot (\nabla) \mathcal{E} + \mu_0 \mathcal{H}^* \cdot (\nabla) \mathcal{H}] = c^2 \mathbf{p}^{\text{orb}} \quad (2.34)$$

and

$$\mathcal{P}^{\text{spin}} = \frac{c}{8k} \nabla \times \text{Im} [\epsilon_0 \mathcal{E}^* \times \mathcal{E} + \mu_0 \mathcal{H}^* \times \mathcal{H}] = c^2 \mathbf{p}^{\text{spin}}, \quad (2.35)$$

where $k = 2\pi/\lambda$ is the wave number of the light field in free space. In these equations, we use the notation $\mathcal{E}^* \cdot (\nabla) \mathcal{E} \equiv \sum_{i=x,y,z} \mathcal{E}_i^* \nabla \mathcal{E}_i$ which applies for \mathcal{H} as well.

For the fundamental quasi-linearly polarized HE_{11} mode, the only nonvanishing component of the Poynting vector is its z -component. This means that for this mode the energy flow points only along the fiber. This is in contrast to the quasi-circularly polarized fundamental mode, where there is also an energy flow in the azimuthal direction around the fiber [63]. In Fig. 2.7 (a)-(c) \mathcal{P}_z , $\mathcal{P}_z^{\text{orb}}$, and $\mathcal{P}_z^{\text{spin}}$ are plotted for the quasi-linearly polarized fundamental mode that has its main direction of polarization along the x axis and propagates in the $+z$ direction. Note that $\mathcal{P}_z^{\text{spin}} < 0$ and thus points opposite to the propagation direction. Nevertheless, since $|\mathcal{P}_z^{\text{spin}}|/|\mathcal{P}_z^{\text{orb}}| \lesssim 40\%$, where equality is reached at the surface of the fiber, the total energy flow still points in the propagation direction of the light field. Note furthermore, that for quasi-linearly polarized light \mathcal{P}_z , $\mathcal{P}_z^{\text{orb}}$, and $\mathcal{P}_z^{\text{spin}}$ are not azimuthally symmetric.

The spin momentum density \mathbf{p}^{spin} can also be expressed in terms of the spin angular momentum density $\mathbf{j}_{\text{local}}^{\text{spin}}$ of the light field [62]

$$\mathbf{p}^{\text{spin}} = \frac{1}{2} \nabla \times \mathbf{j}_{\text{local}}^{\text{spin}}, \quad (2.36)$$

with

$$\mathbf{j}_{\text{local}}^{\text{spin}} = \frac{1}{4kc} \text{Im} [\epsilon_0 \mathcal{E}^* \times \mathcal{E} + \mu_0 \mathcal{H}^* \times \mathcal{H}]. \quad (2.37)$$

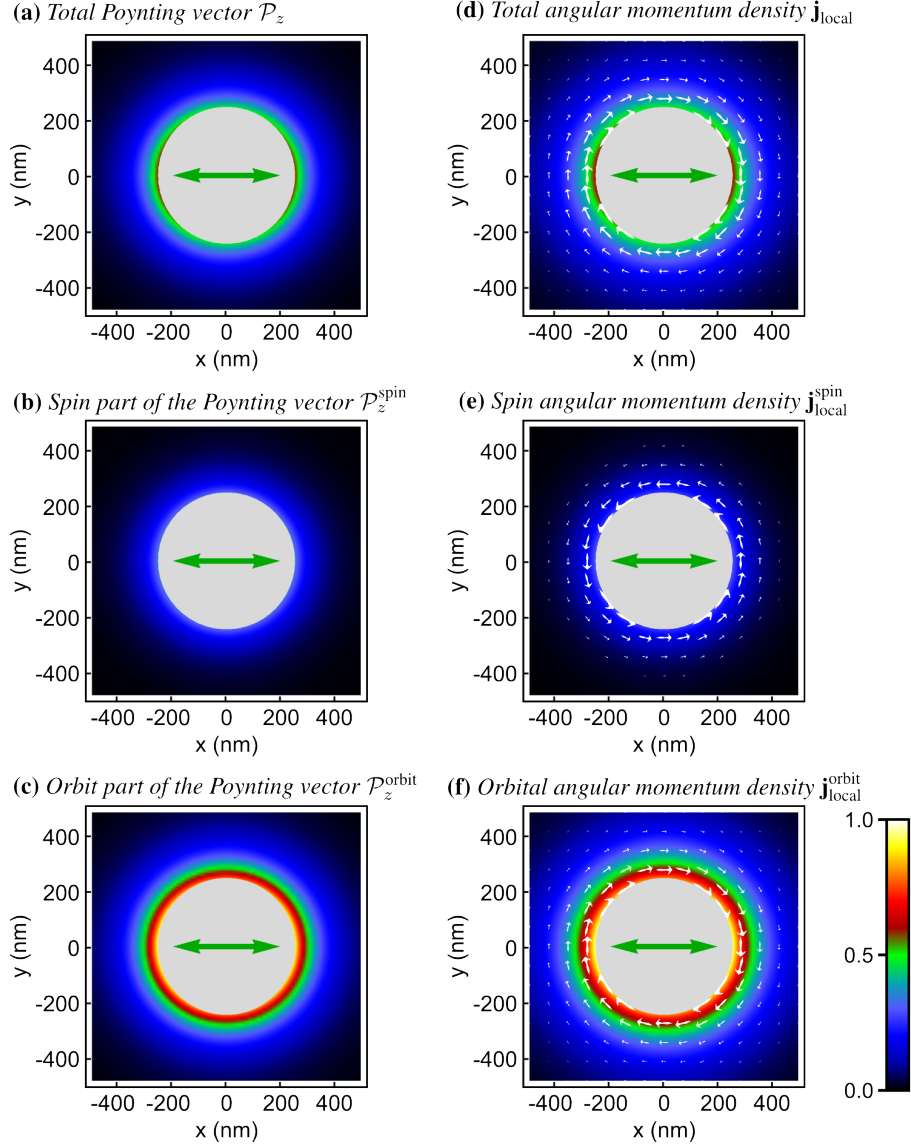


Figure 2.7: (a) Magnitude of the z component \mathcal{P}_z of the total Poynting vector of the evanescent field of a quasi-linearly polarized HE₁₁ mode with its main direction of polarization along the x axis and its spin and orbital parts, (b) $\mathcal{P}_z^{\text{spin}}$, (c) $\mathcal{P}_z^{\text{orbit}}$. Their magnitudes are normalized to the maximum value of its orbit part at $x = \pm a$ and $y = 0$. Note that in (b) $\mathcal{P}_z^{\text{spin}} < 0$ and thus points in the direction opposite to the propagation direction. (d) Total angular momentum density $\mathbf{j}_{\text{local}}$ of the same mode as in (a)-(c) and its decomposition into (e) $\mathbf{j}_{\text{local}}^{\text{spin}}$ and (f) $\mathbf{j}_{\text{local}}^{\text{orbit}}$. Their magnitudes, indicated by the color, are normalized to the maximum value of $\mathbf{j}_{\text{local}}^{\text{orbit}}$ at $x = \pm a$ and $y = 0$. For these plots, the light field with $\lambda = 852$ nm propagates in the $+z$ direction through the nanofiber with a radius of $a = 250$ nm and $n_1 = 1.4525$.

The orbital angular momentum density $\mathbf{j}_{\text{local}}^{\text{orb}}$ that is generated by orbital momentum density \mathbf{p}^{orb} is an extrinsic origin-dependent quantity. It can be given in terms of the Poynting vector as $\mathbf{j}_{\text{local}}^{\text{orb}} = \frac{1}{c^2} \mathbf{r} \times \mathcal{P}^{\text{orb}}$. In contrast to this, the spin angular momentum density $\mathbf{j}_{\text{local}}^{\text{spin}}$ is an intrinsic origin-independent quantity [62]. Its cross-section-integrated value, nevertheless, is determined by the circulation of the spin momentum and can thus be expressed in terms of the Poynting vector by

$$\mathbf{J}^{\text{spin}} = \int \mathbf{j}_{\text{local}}^{\text{spin}} d^2\mathbf{r} = 1/c^2 \int [\mathbf{r} \times \mathcal{P}^{\text{spin}}] d^2\mathbf{r}. \quad (2.38)$$

Note that the integration is performed over the cross-sectional plane of the fiber and thus yields the spin angular momentum per unit length.

In Fig. 2.7 (d)-(f) the angular momentum density $\mathbf{j}_{\text{local}} = \mathbf{j}_{\text{local}}^{\text{orb}} + \mathbf{j}_{\text{local}}^{\text{spin}}$ and its spin and orbital parts are plotted for the quasi-linearly polarized HE_{11} mode which has its main axis of polarization along the x axis. These quantities only exhibit nonzero transverse components (x and y components), i.e., there is no component in the z direction. Note that the integral of the local spin and orbital angular momentum is zero for the quasi-linearly polarized HE_{11} mode. Thus, their sum, i.e., the total angular momentum per unit length $\mathbf{J} = \int \mathbf{j}_{\text{local}} d^2\mathbf{r}$, is zero as well.

Here, the consequences of the spin–orbit interaction of the light field are apparent: In contrast to paraxial light fields, where there is no SOI, the direction of the spin angular momentum density is position-dependent and in general not parallel to the propagation direction of the fields [62, 64]. For the present case of quasi-linearly polarized light fields, it is even orthogonal to the propagation direction [51]. Furthermore, $\mathbf{j}_{\text{local}}^{\text{spin}}$ points in opposite directions on opposite sides of the fiber. This effect is often referred to as the spin-Hall effect of light [29, 31, 51, 65]. It is important to emphasize that the angular momentum density $\mathbf{j}_{\text{local}}$ and its components point in opposite directions for a change of the light field’s propagation direction.

All these properties of the spin–orbit coupled light manifest in the unique polarization of the nanofiber-guided modes that have been discussed in the previous chapter 2.2. The most important properties of the modes’ polarization are summarized in table 2.1, where the normalized polarization components in the spherical tensor basis of the nanofiber-guided modes given by $\xi_j = \mathcal{E}_j^2 / |\mathcal{E}^* \mathcal{E}|^2$ with $j \in (\sigma^+, \pi, \sigma^-)$ are shown. Thus, ξ_j represents the part of the guided mode that is σ^+ , π , and σ^- polarized.

2.3.2 Maximizing the spin–orbit interaction

In order to increase the local spin density $\mathbf{j}_{\text{local}}^{\text{spin}}$, I will restrict myself to its electrical part only. This is justified since I only investigate the interaction of the electric part of the light field with the atoms. The electric part of $\mathbf{j}_{\text{local}}^{\text{spin}}$ is proportional to the ellipticity vector

$$\epsilon = \frac{\text{Im} [\mathcal{E}^* \times \mathcal{E}]}{|\mathcal{E}|^2}, \quad (2.39)$$

which I will use in the following calculations. Here, I consider a quasi-linearly polarized light field with its main axis of polarization along the x axis. In Fig. 2.8 (a) $|\epsilon|$ is plotted as a function of the V-parameter $V = 2\pi \cdot a/\lambda_0 \cdot \sqrt{n_1^2 - n_2^2}$ where the ratio a/λ_0 has been varied.

main direction of polarization	propagation direction	ξ_{σ^-}		ξ_{σ^+}		ξ_{π}	
		left	right	left	right	left	right
$p = x$	$+z$	92.1 %	7.9 %	7.9 %	92.1 %	0 %	0 %
	$-z$	7.9 %	92.1 %	92.1 %	7.9 %	0 %	0 %
$p = y$	$+z$	0.0 %	0.0 %	0.0 %	0.0 %	100 %	100 %
	$-z$	0.0 %	0.0 %	0.0 %	0.0 %	100 %	100 %

Table 2.1: Fractions, ξ_{σ^+} , ξ_{π} , and ξ_{σ^-} , of the nanofiber-guided mode that are σ^+ , π , and σ^- polarized, respectively, evaluated at the position of the atoms. Here, “left” stands for the position at $x = -480$ nm and $y = 0$ nm and “right” stands for the position at $x = +480$ nm and $y = 0$ nm. The main direction of polarization of the quasi-linearly polarized HE_{11} mode and its propagation direction are indicated as well.

The ellipticity is shown at the surface of the fiber at ($x = a$ and $y = 0$ nm) (solid red line) and 230 nm away from the fiber’s surface at ($x = a + 230$ nm and $y = 0$ nm) (solid black line). For $\lambda_0 \ll a$ the magnitude of the ellipticity approaches the theoretical limit for grazing incidence of a light field at a dielectric surface of $\epsilon_g = (2n_1\sqrt{n_1^2 - n_2^2})/(2n_1^2 - n_2^2) \approx 0.95$ [34]. Here, $n_1 = 1.4525$ is the refractive index of silica and $n_2 = 1$ the one of vacuum. When the V -parameter exceeds $V = 2.405$, the waveguide reaches the multimode regime. At this point, the magnitude of the ellipticity reaches $\epsilon \approx 0.9$. For a wavelength of $\lambda_0 = 852$ nm this corresponds to a fiber radius of $a = 309$ nm.

The ellipticity can also be increased by changing the refractive index of the core medium n_1 , see Fig. 2.8 (b). But for the given radius $a = 250$ nm and $\lambda_0 = 852$ nm already for $n_1 > 1.64$ the fiber is no longer single-mode. Nevertheless, at this limit the ellipticity reaches $\epsilon \approx 0.94$. In general, the magnitude of the ellipticity vector $|\epsilon|$ can vary from -1 to $+1$. The minimum represents fully σ^- -polarized light and the maximum fully σ^+ -polarized light with respect to a quantization axis which is aligned parallel to ϵ . This means that at the position specified above $(1 + \epsilon)/2 \approx 97\%$ of the light field is σ^+ polarized.

2.4 Tapered optical fiber with a nanofiber waist

In the previous sections, the propagation of a light field in optical nanofibers and the structure of its electric field have been discussed. The nanofibers need to have a radius on the order of the wavelength of the light field to provide such a strong evanescent field as shown in the previous sections. In order to realize a nanofiber based dipole trap, the light field has to be coupled into such a nanofiber. However, the coupling should be efficient in order to efficiently interface the trapped atoms.

Here, we realized the nanofiber as the waist of a tapered optical fiber (TOF). In Fig. 2.9, a schematic picture of a TOF is shown. A light field is coupled into a standard optical fiber¹ and propagates until it reaches the taper region, where the diameter of the fiber is decreasing.

¹In this experiment, a “Liekki 6/125 Passive” was used, with a cladding diameter of 125 μm and an effective mode field diameter of 6 μm .

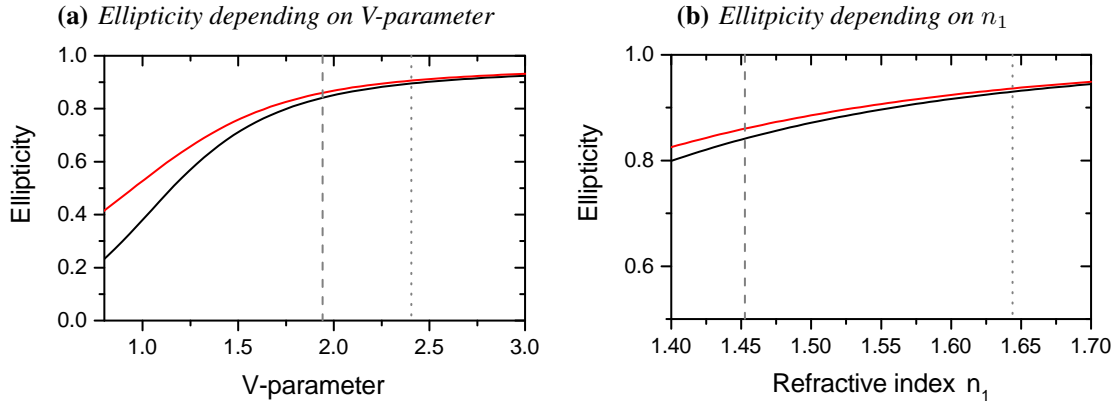


Figure 2.8: The ellipticity depending on (a) the V-parameter for varying a/λ_0 and (b) the refractive index of the fiber n_1 . The ellipticity is plotted at the fiber's surface $x = a$ and $y = 0$ nm (solid red line) and 230 nm away from the surface (solid black line). The gray dashed line indicates the current configuration and the gray dotted line the limit for single-mode operation. In (a) the parameters $n_1 = 1.4525$ and $n_2 = 1$ were used for the calculations. In (b) the radius of the fiber was set to $a = 250$ nm and the wavelength of the light field to $\lambda_0 = 852$ nm.

While propagating through the taper, the light field is first compressed and, for core diameters smaller than the wavelength of the light field, expands again, leaves the core, and is guided by the cladding. The mode transformation in the taper region has been studied in detail in [66]. At the waist, the fiber reaches a diameter of about 500 nm and the evanescent field of the guided light protrudes in the surrounding vacuum. The shape of the taper is of uttermost importance [67] to guarantee an adiabatic transformation of the weakly guided fundamental mode of the standard fiber to the strongly guided fundamental mode at the waist of the TOF. After propagating through the waist, the light passes another taper region and is transformed back to the weakly guided fundamental mode of the unstretched fiber. For cautiously designed taper regions transmission of up to 99% [68] and higher [69] have been realized.

Production of tapered optical fibers

The TOF used here has been produced using the so-called flame brushing technique. A principle sketch of a fiber pulling rig [70, 71], that produces those fibers, is shown in Fig. 2.10. The fiber is mounted on a high-precision translation stage and heated from below with a hydrogen-oxygen flame. The translation stage moves the fiber in an oscillatory way over the flame while it simultaneously stretches and therefore thins the fiber. In order to reproducibly fabricate tapered optical fibers with a predefined shape of the taper region and the waist the whole production process is computer controlled² [73].

The TOF is then fixed on an aluminum mount and put into a vacuum chamber. It is very important for the whole procedure to take place in a dust-free environment, so that the waist of

²For more characteristics of the nanofiber used in the experiments here see [72].

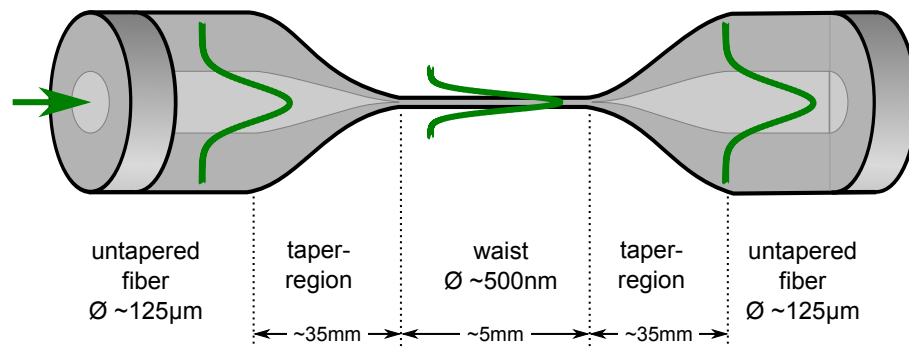


Figure 2.9: Schematic of a tapered optical fiber, where the light gray area indicates the core and the darker gray region indicates the cladding of the fiber. A light field is coupled into the fiber (green arrow) and propagates, guided by the core, inside the fiber shown by the sketched intensity profiles (green curves). At the taper transition the core vanishes and the light is now guided by the cladding. At the waist, the light field protrudes out of the fiber in the surrounding vacuum.

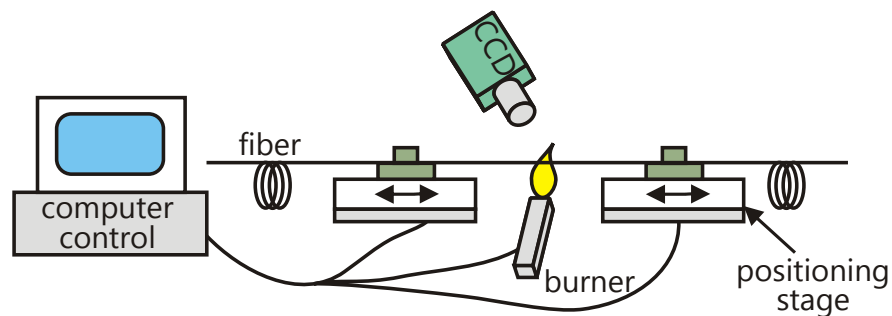


Figure 2.10: Schematic of a fiber pulling rig implementing the flame brushing technique. The picture shows the computer that controls the movement of the positioning stages, the hydrogen oxygen flame, the fiber mounted on the positioning stages, and a CCD camera for monitoring the fiber diameter.

the TOF stays clean. If this is respected, it is possible for the vacuum-clad fiber to guide optical powers of a few 100 mW without showing degradation or fusing [74]. For creating a nanofiber based dipole trap, this is an important property since the powers of the trapping light field can reach several tens of mW.

Atom–light interaction

In order to investigate and harness the quantum nature of neutral atoms they have to be isolated from the environment and the relevant internal and external degrees of freedom have to be controlled. An unintended interaction of the atoms with the environment alters the quantum state of the atom, leads to decoherence, and therefore has to be avoided. In our experiments, we want the atoms to interact with fiber-guided light fields. Therefore, we need to bring the atoms very close to the surface of the nanofiber. This can be realized by storing the atoms in a nanofiber-based optical dipole trap. Except for the interaction with the trapping light fields, the atoms will then ideally be isolated from the environment. To understand the working principle of these traps, the dispersive interaction between atoms and light fields has to be studied.

In the first section of this chapter, I will focus on the level structure of cesium 133. In the next section, I describe the dispersive interaction of the cesium atom with light fields. I will calculate the atomic polarizabilities and the light shifts due to the ac Stark interaction. I then calculate the dipole trapping potentials for nanofiber-guided light fields for cesium atoms. The section is concluded by studying how the eigenenergies and the eigenstates of the atoms are altered in the dipole trap. In the last section, I study fictitious magnetic fields that arise due to the ac Stark interaction.

3.1 Hyperfine interaction

Cesium is an alkali-metal atom and has only one stable isotope with an atomic mass of 133 [75]. Alkali atoms are of particular interest because they have electronic transitions in the optical domain and a simple hydrogen-like level scheme. In addition, they possess closed transitions which makes it possible to conveniently cool, trap, and manipulate them with laser light fields. Alkali atoms have fully occupied shells except for the outermost shell with only one valence electron. The closed shells do not contribute to the angular momentum. Thus, the spin angular momentum \mathbf{S} and the orbital angular momentum \mathbf{L} of the atom is solely governed by the contributions of the valence electron. The atomic state can be written in the Russel Saunders

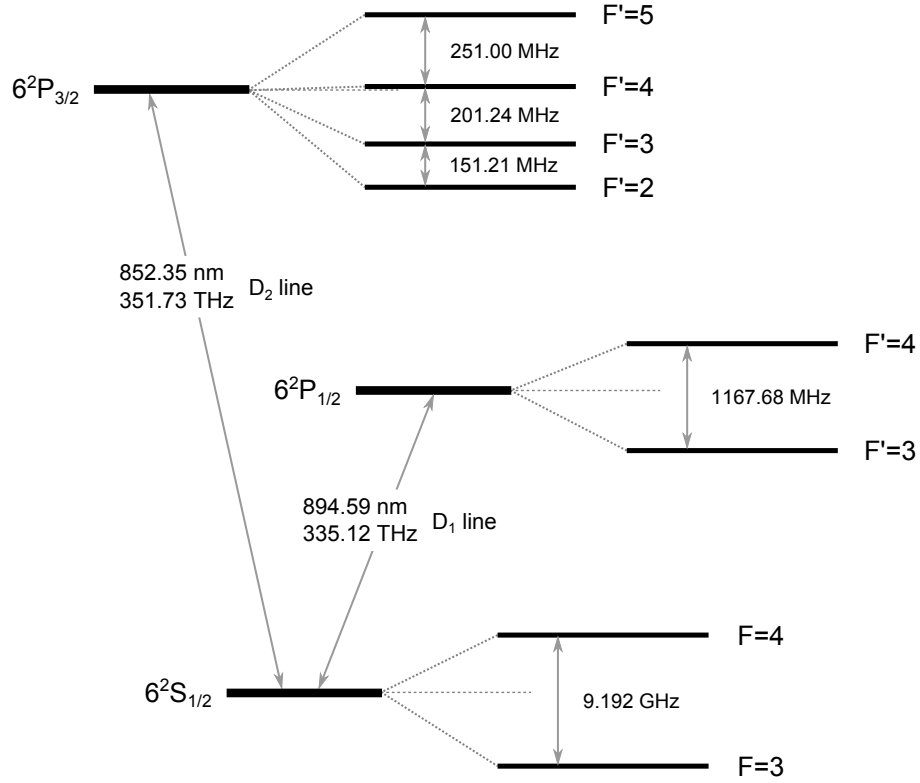


Figure 3.1: Level scheme of cesium for the D₁ and D₂ line showing the transition frequencies for the different levels.

notation

$$n^{2S+1}L_J, \quad (3.1)$$

where n represents the principal quantum number and $\mathbf{J} = \mathbf{L} + \mathbf{S}$ is the total angular momentum. The spin-orbit coupling leads to the fine structure of the atomic energy levels, where J can take values in the range $|L - S| \leq J \leq L + S$. Furthermore, the total electronic angular momentum \mathbf{J} is coupled to the nuclear spin \mathbf{I} and both form the total angular momentum $\mathbf{F} = \mathbf{I} + \mathbf{J}$, which leads to the hyperfine structure. The nuclear spin of Cs is $I = 7/2$ and $S = 1/2$ due to the presence of only one valence electron. In figure 3.1 the level scheme¹ of atomic cesium for the D₁ and the D₂ lines and the corresponding transition frequencies are shown.

The hyperfine structure interaction operator V^{hfs} is diagonal in the $|nJFm_F\rangle$ basis and is

¹An energy level with the orbital angular momentum $L = 0$ is called “S” (sharp) and with the angular momentum $L = 1$ is called “P” (principal)

given by [76]

$$V^{\text{hfs}} |nJFm_F\rangle = \left(\frac{1}{2} \hbar A_{\text{hfs}} G + \hbar B_{\text{hfs}} \frac{\frac{3}{2} G(G+1) - 2I(I+1)J(J+1)}{2I(2I-1)2J(2J-1)} \right) |nJFm_F\rangle, \quad (3.2)$$

with $G = F(F+1) - I(I+1) - J(J+1)$. Here, m_F is the magnetic quantum number, i.e., the projection of \mathbf{F} onto the quantization axis. It can take $2F+1$ different values in the usual way ($m_F = -F, -F+1, \dots, 0, \dots, F-1, F$). The hyperfine constants A_{hfs} and B_{hfs} can be found in [75, 77] and are $A_{\text{hfs}} = 2\pi \cdot 2298.1579$ MHz, $B_{\text{hfs}} = 0$ MHz for the $6^2S_{1/2}$ ground state and $A_{\text{hfs}} = 2\pi \cdot 50.2883$ MHz, $B_{\text{hfs}} = -2\pi \cdot 0.4934$ MHz for the $6^2P_{3/2}$ excited state. An interesting feature of cesium 133 is that the energetic splitting of the hyperfine ground states is used to define the second in SI-units. Therefore, this splitting is defined to be exactly 9192.631770 MHz [78, 79].

3.2 AC Stark shift and atomic polarizability

In this section, the focus lies on the dispersive interaction of an atom with a classical light field. In 1914, Johannes Stark first discovered that an electric field can shift and split the spectral lines of atoms or molecules, which is nowadays known as the Stark effect. Here, we discuss the so-called ac Stark effect that occurs for interaction of atoms with alternating electric fields, like light fields. The derivation given here follows closely [76].

3.2.1 AC Stark interaction

In the dipole approximation, the interaction of an atom with an electric field is described by the operator

$$V^E = -\mathbf{E} \cdot \mathbf{d}, \quad (3.3)$$

where \mathbf{E} is the electric field and \mathbf{d} is the atomic dipole operator. The electric field has the form

$$\mathbf{E} = \frac{1}{2} \mathcal{E} e^{-i\omega t} + c.c., \quad (3.4)$$

where $\mathcal{E} = \mathcal{E} \mathbf{u}$ is the positive electric field envelope, that is composed of the field amplitude \mathcal{E} and the polarization unit vector \mathbf{u} , both of which are in general complex quantities. The angular frequency of the electric field is given by ω and *c.c.* denotes the complex conjugate of the preceding term. Thus, the interaction operator can be written in the form

$$V^E = -\frac{1}{2} \mathcal{E} \mathbf{u} \cdot \mathbf{d} e^{-i\omega t} - \frac{1}{2} \mathcal{E}^* \mathbf{u}^* \cdot \mathbf{d} e^{i\omega t}. \quad (3.5)$$

We consider the case where the light is far from resonance with the atom. Furthermore, we assume that the interaction with the light results in a change of the eigenenergies that is small compared to the fine structure splitting, i.e., J is a good quantum number. The change δE_a of

the free eigenenergy $\hbar\omega_a$ of an atomic state $|a\rangle$ is then calculated by applying the perturbation theory. Treating the effect of the light field as a first order perturbation leaves, except for a few atoms like hydrogen, the eigenenergy unchanged [80]. For second order perturbation theory, the change of the eigenenergy for the eigenstate $|a\rangle$ is in general nonzero and can be written as

$$\delta E_a = -\frac{|\mathcal{E}|^2}{4\hbar} \sum_b \operatorname{Re} \left(\frac{|\langle b | \mathbf{u} \cdot \mathbf{d} | a \rangle|^2}{\omega_b - \omega_a - \omega - i\gamma_{ba}/2} + \frac{|\langle a | \mathbf{u} \cdot \mathbf{d} | b \rangle|^2}{\omega_b - \omega_a + \omega + i\gamma_{ba}/2} \right). \quad (3.6)$$

Here, $|b\rangle$ is an eigenstate with the eigenenergy $\hbar\omega_b$. The linewidth of the transition $|a\rangle \rightarrow |b\rangle$ is given by $\gamma_{ab} = \gamma_a + \gamma_b$, with $\gamma_{a,b}$ being the spontaneous decay rates of the eigenstates $|a\rangle$ and $|b\rangle$, respectively. Equation (3.6) shows that the ac Stark shift depends quadratically on the electric field and therefore linearly on the field's intensity.

We rewrite the shift as an expectation value $\delta E_a = \langle a | V^{EE} | a \rangle$, where the effective operator for the ac Stark interaction V^{EE} is then given as [76]

$$V^{EE} = \frac{|\mathcal{E}|^2}{4} [(\mathbf{u}^* \cdot \mathbf{d})R_+(\mathbf{u} \cdot \mathbf{d}) + (\mathbf{u} \cdot \mathbf{d})R_-(\mathbf{u}^* \cdot \mathbf{d})], \quad (3.7)$$

with

$$\begin{aligned} R_+ &= -\frac{1}{\hbar} \sum_b \frac{1}{\omega_b - \omega_a - \omega - i\gamma_{ba}/2} |b\rangle \langle b|, \\ R_- &= -\frac{1}{\hbar} \sum_b \frac{1}{\omega_b - \omega_a + \omega + i\gamma_{ba}/2} |b\rangle \langle b|. \end{aligned} \quad (3.8)$$

The effective operator V^{EE} correctly describes the level shifts and the level mixing of degenerate and non-degenerate states. A rigorous derivation of V^{EE} can be found in [80–83].

To study the effect of an external light field on a realistic multilevel atom, an interaction Hamiltonian H_{int} has to be introduced. Since the atomic states are perturbed by both, the hyperfine interaction V^{hfs} and the ac Stark interaction V^{EE} , the combined Hamiltonian reads:

$$H_{\text{int}} = V^{\text{hfs}} + V^{EE}. \quad (3.9)$$

This Hamiltonian has to be diagonalized in order to find the new eigenstates and eigenenergies of the system.

Since we only consider the case where J is a good quantum number, we can examine the light shifts in each single fine structure manifold $|nJ\rangle$ separately. The interaction operator given in Eq. (3.7) can then be written in terms of the hyperfine basis states $|nJFm_F\rangle$ and takes the form

$$V^{EE} = \sum_{Fm_F F'm'_F} V_{Fm_F F'm'_F}^{EE} |nJFm_F\rangle \langle nJF'm'_F|, \quad (3.10)$$

with the matrix elements

$$V_{Fm_F F' m'_F}^{EE} = \frac{1}{2} |\mathcal{E}|^2 \sum_{\substack{K=0,1,2 \\ q=-K,\dots,K}} \alpha_{nJ}^{(K)} \{\mathbf{u}^* \otimes \mathbf{u}\}_{Kq} (-1)^{J+I+K+q-m_F} \\ \times \sqrt{(2F+1)(2F'+1)} \begin{pmatrix} F & K & F' \\ m_F & q & -m'_F \end{pmatrix} \begin{Bmatrix} F & K & F' \\ J & I & J \end{Bmatrix}. \quad (3.11)$$

Here, we introduced here the reduced dynamical polarizability $\alpha_{nJ}^{(K)}$ of rank K . The Wigner 3- j and the Wigner 6- j symbols are denoted by the last two expressions in round brackets and curly brackets, respectively. The expression $\{\mathbf{u}^* \otimes \mathbf{u}\}_{Kq}$ are the compound tensor components defined as

$$\{\mathbf{u}^* \otimes \mathbf{u}\}_{Kq} = \sum_{\mu, \mu'=-1,0,1} (-1)^{q+\mu'} u_\mu u_{-\mu'}^* \sqrt{2K+1} \begin{pmatrix} 1 & K & 1 \\ \mu & -q & \mu' \end{pmatrix}, \quad (3.12)$$

where u_μ are the spherical tensor components (see section 2.2) of the polarization vector \mathbf{u} . The ac Stark interaction operator (3.10) can further be written in the form

$$V^{EE} = -\frac{1}{4} |\mathcal{E}|^2 \left\{ \alpha_{nJ}^s - i\alpha_{nJ}^v \frac{[\mathbf{u}^* \times \mathbf{u}] \cdot \mathbf{J}}{2J} + \alpha_{nJ}^T \frac{3[(\mathbf{u}^* \cdot \mathbf{J})(\mathbf{u} \cdot \mathbf{J}) + (\mathbf{u} \cdot \mathbf{J})(\mathbf{u}^* \cdot \mathbf{J})] - 2J^2}{2J(2J+1)} \right\} \quad (3.13)$$

that consists of the sum of three parts, called the scalar, vector and tensor component of the interaction operator. In this equation, we introduced the scalar (α_{nJ}^s), vector (α_{nJ}^v), and tensor (α_{nJ}^T) part of the conventional dynamical polarizability:

$$\alpha_{nJ}^s = \frac{1}{\sqrt{3(2J+1)}} \alpha_{nJ}^{(0)} \\ \alpha_{nJ}^v = -\sqrt{\frac{2J}{(J+1)(2J+1)}} \alpha_{nJ}^{(1)} \\ \alpha_{nJ}^T = -\sqrt{\frac{2J(2J-1)}{3(J+1)(2J+1)(2J+3)}} \alpha_{nJ}^{(2)} \quad (3.14)$$

where the reduced dynamical scalar ($K=0$), vector ($K=1$), and tensor ($K=2$) polarizabilities $\alpha_{nJ}^{(K)}$ are given by

$$\alpha_{nJ}^{(K)} = (-1)^{K+J+1} \sqrt{2K+1} \sum_{n'J'} (-1)^{J'} \begin{Bmatrix} 1 & K & 1 \\ J & J' & J \end{Bmatrix} |\langle n'J' | \mathbf{d} | nJ \rangle|^2 \\ \times \frac{1}{\hbar} \operatorname{Re} \left(\frac{1}{\omega_{n'J'} - \omega_{nJ} - \omega - i\gamma_{n'J'nJ}/2} + \frac{(-1)^K}{\omega_{n'J'} - \omega_{nJ} + \omega + i\gamma_{n'J'nJ}/2} \right). \quad (3.15)$$

The three different parts of the ac Stark interaction operator given in Eq. (3.13) influence the atomic levels in the following way: The scalar part results in a global shift on all the sublevels of

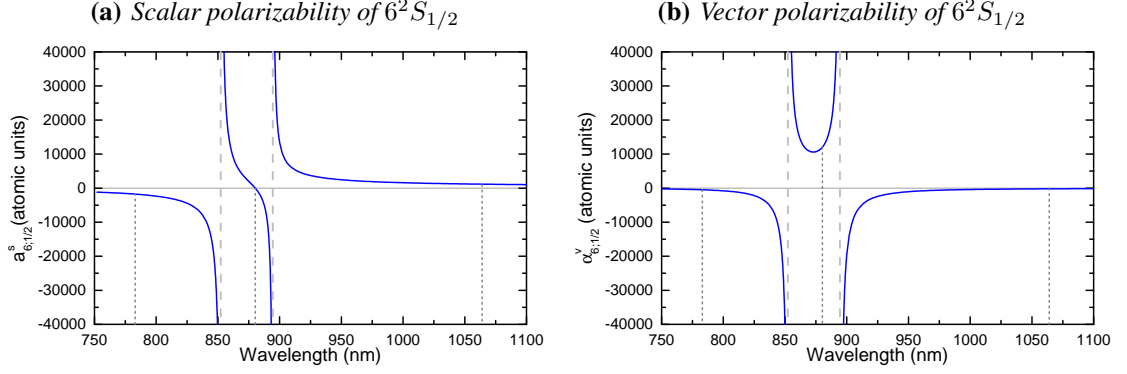


Figure 3.2: (a) Scalar and (b) vector polarizability of the $6^2S_{1/2}$ ground state of ^{133}Cs as a function of the wavelength. The dotted lines indicate the wavelengths of the two far detuned trapping laser at 783 nm and 1064 nm used in the experiments described here and the tune-out wavelength at 880.2524 nm.

a hyperfine multiplet and only depends on $|\mathcal{E}|^2$. The vector part acts on the magnetic sublevels m_F of one hyperfine level. The cross product ($\mathbf{u}^* \times \mathbf{u}$) of the polarization vector of the electric field makes the vector part nonzero only for light fields with a polarization that exhibits a nonzero ellipticity. In terms of spherical tensor components, this means $u_{-1} \neq u_{+1}$. For states, with total angular momentum $J = 1/2$, e.g., the ground state of alkali atoms like cesium, the tensor part in the interaction operator vanishes. This is due to the fact that the Wigner $6-j$ symbol in Eq. (3.15) is zero for $J = 1/2$ and $K = 2$.

Note that Eq. (3.15) only fixes the real part of the complex polarizability. The imaginary part of the complex polarizability is related to the scattering rate of the atom and is given in [84]. Furthermore, for far detuned light, one can neglect the contribution of the linewidth $\gamma_{n'J'nJ}$ of the considered transition in Eq. (3.15).

Let us take a closer look at the form of the parts of the conventional dynamical polarizability for atomic cesium. The atomic polarizability given in Eq. (3.14) is calculated for the ground state and is shown in Fig. 3.2. For this calculation, only the contributions of the $6^2S_{1/2} \rightarrow (6-40)^2P_{1/2}$ and $6^2S_{1/2} \rightarrow (6-40)^2P_{3/2}$ transitions only are taken into account. The tabled values for the transition energies and the dipole matrix elements $|\langle n'J' | \mathbf{d} | nJ \rangle|^2$ are listed in [76]. Two resonances are visible (see Fig. 3.2) at the wavelengths 852 nm and 894 nm representing the D_2 and the D_1 line, respectively. An interesting feature is revealed between the two resonances at 880.2524 nm: the scalar component of the polarizability vanishes whereas the vector component remains nonzero. This wavelength is called a tune-out wavelength [85]. At this wavelength the contributions of the scalar polarizabilities from the D_2 and D_1 transitions cancel each other.

In Fig. 3.3, the polarizability of the excited $6^2P_{3/2}$ is shown. For its calculation, the contributions of the $6^2P_{3/2} \rightarrow (6-40)^2S_{1/2}$, $6^2P_{3/2} \rightarrow (5-42)^2D_{3/2}$, and $6^2P_{3/2} \rightarrow (5-42)^2D_{5/2}$ transitions are taken into account. With these plots, in conjunction with the ground state polarizabilities, it is possible to determine, for example, the so-called magic wavelength, where the scalar polarizability of the ground and the excited state have the same value and their energy

Wavelength	ground states $6^2S_{1/2}$		excited states $6^2P_{3/2}$		
	$\alpha_{6,1/2}^s$ (a.u.)	$\alpha_{6,1/2}^v$ (a.u.)	$\alpha_{6,3/2}^s$ (a.u.)	$\alpha_{6,3/2}^v$ (a.u.)	$\alpha_{6,3/2}^T$ (a.u.)
1064 nm	1164.03	-198.64	-57.35	276.17	527.41
880.25 nm	0.00	12031.10	-3666.31	-8236.62	2246.71
783 nm	-1761.63	-479.96	136.51	2418.42	-363.99

Table 3.1: Scalar, vector and tensor part of the dynamical atomic polarizabilities for the three far off-resonant light fields used in the experiment. All values are given in atomic units.

levels therefore experience the same shift in first order approximation. Here, the blue-detuned magic wavelength is 686.3 nm and the red-detuned magic wavelength is 935.2 nm [76]. The terminology “blue-detuned” (“red-detuned”) refers to wavelengths that are shorter (longer) than those of the D-line transitions.

In our experiment, we use three off-resonant light fields: a red- and a blue-detuned light field for trapping the atoms and a light field at the tune-out wavelength. The polarizabilities for these light fields are summarized in table 3.1. The calculated polarizabilities are given in atomic units. The conversion to SI units requires multiplication by the factor $(ea_0)^2/E_h$, where e is the charge of one electron, a_0 is the Bohr radius, and $E_h = m_e e^4 / (4\pi\epsilon\hbar)^2$ is the Hartree energy with the electron mass m_e .

3.3 A two-color dipole trap

In the previous sections, the theoretical background regarding the character of the evanescent field of nanofiber-guided light modes and the interaction of far detuned light fields with atoms has been given. With these ingredients, it is possible to describe and to build a nanofiber-based two-color dipole trap for cesium atoms.

In the previous section, we learned that the ac Stark interaction changes the eigenenergy of atomic levels. For the ground state of cesium atoms and linearly polarized light, we only have to consider the scalar part of the ac Stark interaction. Since the scalar part is proportional to the intensity of the light field, we can generate a trapping potential by spatially modulating the intensity of the light field. A common way to achieve this is to use a strongly focused laser beam [86]. Another method that has been first theoretically discussed in [36, 37] and first experimentally realized in [38] uses the spatially varying evanescent fields that are guided in an optical nanofiber. Here, the basic properties of such a nanofiber-based two-color dipole trap for atomic cesium will be discussed.

3.3.1 Dipole trap for neutral cesium atoms

The atoms should be trapped close to the surface of the nanofiber in order to maximize overlap of the interaction cross section of the atom with the fiber-guided light fields. Furthermore, we want to realize strong three-dimensional confinement to prevent collisions between the trapped atoms and to fix them at a defined position with respect to the fiber.

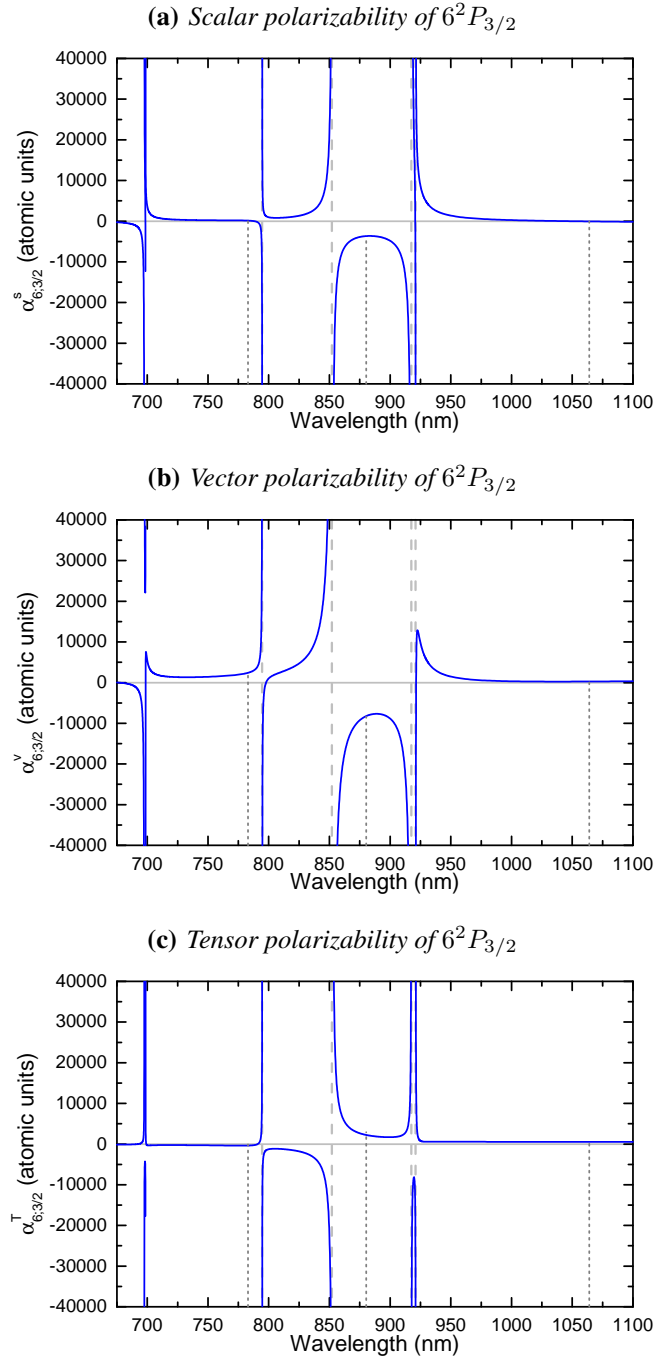


Figure 3.3: (a) Scalar, (b) vector, and (c) tensor polarizability of the $6^2P_{3/2}$ excited state of cesium 133 as a function of the wavelength. The dotted lines indicate the wavelengths of the two far detuned trapping lasers at 783 nm and 1064 nm used in the experiments described here and the tune-out wavelength for the ground state at 880.2524 nm.

In order to fulfill these requirements, we first need an attractive potential to bring the atoms close to the nanofiber. A red-detuned light field sent through the fiber creates such an attractive potential, since the scalar ground state polarizability of the cesium atoms is positive for this wavelength. To prevent the atom of getting adsorbed on the surface, we sent a blue-detuned light field ($\alpha_{6,1/2}^s < 0$) in the nanofiber that creates a repulsive potential for the atoms. This is necessary since the spectral properties of adsorbed atoms would be drastically altered. To calculate the spatial potential, the interaction Hamiltonian that is given in Eq. (3.10) is diagonalized. In Fig. 3.4.(a) the potentials created by the red-detuned light field, U_{red} , by the blue-detuned light field, U_{blue} , and the total potential, $U_{\text{tot}} = U_{\text{red}} + U_{\text{blue}} + U_{\text{vdW}}$, are plotted as a function of the radial position from the fiber surface. Note that in this plot, the van der Waals potential, U_{vdW} , which is caused by surface interaction of the fiber and the atoms [36,57] is also taken into account. The parameters that are used to calculate the results presented here are summarized in table 3.2.

The red-detuned light field clearly generates an attractive potential, i.e., the potential decreases for $r \rightarrow a$ [Fig. 3.4 (a)]. The blue-detuned light field generates a repulsive potential. Due to the fact that the decay constants of the evanescent field is wavelength-dependent, the evanescent field of the blue-detuned light field is more strongly confined to the fiber than the evanescent field of the red-detuned light field. For the given powers of the trapping light fields, this causes U_{tot} to have a minimum that is located at a distance of around $r - a = 234$ nm from the fiber surface and that has a depth of $U_{\text{tot,min}} \approx 140 \mu\text{K } k_B = 2.9 \text{ MHz } h$. Here, k_B and h are Boltzmann's and Planck's constant, respectively, and the zero of the energy scale corresponds to an atom in free space in the absence of light fields, i.e., far from the fiber.

The azimuthal confinement is achieved by the azimuthally asymmetric intensity distribution of a quasi-linearly polarized light field (see Fig. 2.5.(c) in the previous chapter). The total potential in the x - y plane is plotted in Fig. 3.4.(b), where the spatially varying potential around the fiber is apparent. In order to maximize the azimuthal confinement, both light fields are quasi-linearly polarized while their main directions of polarization are orthogonal with respect to each other: the red-detuned light field is polarized along the x axis and the blue-detuned light field along the y axis.

The remaining spatial degree of freedom is along the fiber axis. Confinement in this direction is realized by sending the red-detuned light field from both sides into the fiber, thereby creating a standing wave. In 3.4.(c) the trapping potential along the fiber is shown. The full three-dimensional confinement resulting from these settings is shown in Fig. 3.4.(d). The fiber and the equipotential surfaces of the single trapping sites are presented to scale. The trapping sites form two diametric one-dimensional arrays along the nanofiber.

Note that at the exact trapping minimum of the ground states only the scalar polarizability contributes to the total potential since both light fields are perfectly linearly polarized at the trapping minimum making the vector part zero: The blue-detuned light field has its main axis of polarization along the y axis and is therefore completely linearly polarized along the x axis. The red-detuned light field is everywhere completely linearly polarized since the ellipticity vectors of the two counter-propagating light fields are anti-parallel and thus cancel each other [45].

The calculated trapping frequencies for the potentials shown in Fig. 3.4 are 119 kHz, 85 kHz, and 186 kHz for the radial, azimuthal, axial direction respectively. Although the trap is strongly

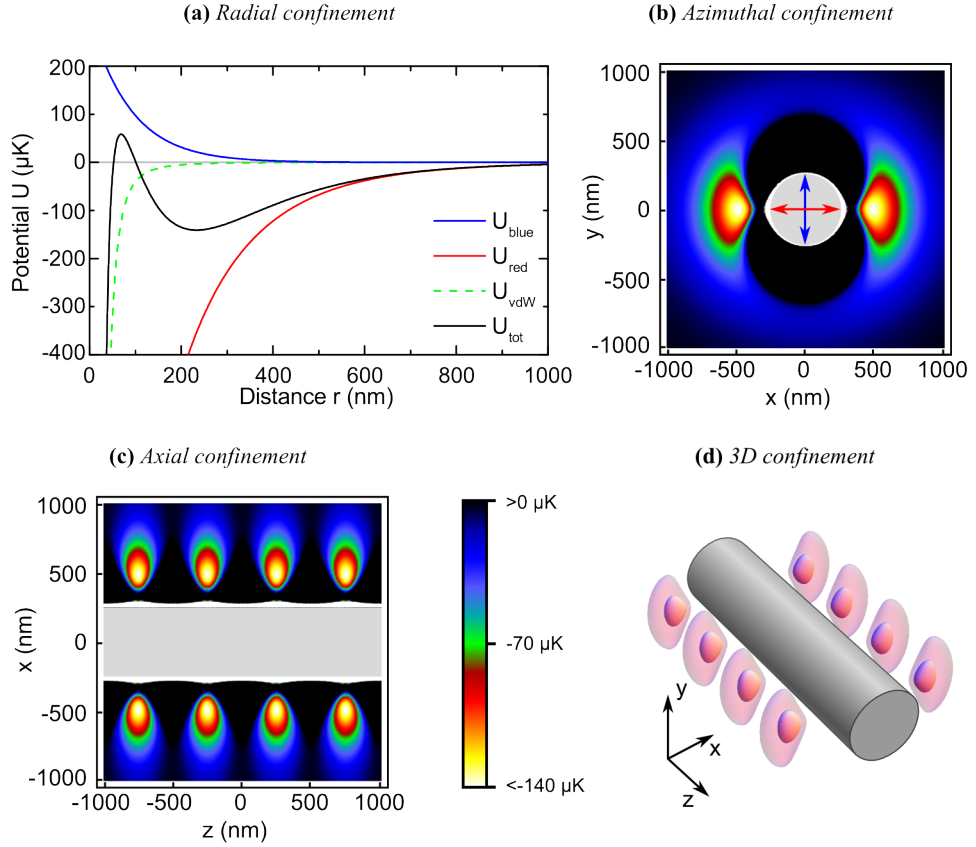


Figure 3.4: (a) The potentials induced by the blue-detuned light field, U_{blue} (blue line), the red-detuned light field, U_{red} (red line), the van der Waals interaction, U_{vdW} (dashed green line), and the resulting total potential, $U_{\text{tot}} = U_{\text{blue}} + U_{\text{red}} + U_{\text{vdW}}$ (black line) as a function of the radial distance $r - a$ from the fiber surface. (b) Density plot of the total potential in the x - y plane. The red and blue arrows indicate the main direction of polarization of the red- and the blue-detuned light fields, respectively. The gray disk symbolizes the fiber. (c) Density plot of the total potential in the x - z plane. The gray rectangle indicates the fiber. (d) To-scale three-dimensional sketch of the nanofiber and the two resulting diametric one-dimensional arrays of trapping sites. The red-shaded areas display equipotential surfaces at $25 \mu\text{K}$ and $75 \mu\text{K}$ above the local minimum of the potential.

	Wavelength	Power	Quasi-linear polarization	Propagation
Red-detuned light field	1064 nm	2×0.77 mW	along x axis	standing wave
Blue-detuned light field	783 nm	8.55 mW	along y axis	running wave

Table 3.2: Parameters of the trapping light fields used to calculate the energy shifts presented in this thesis.

anharmonic, the given trap frequencies are obtained by a quadratic fit assuming the trapping potential to be harmonic close to the minimum.

3.3.2 Eigenstates and eigenenergies at the trapping minimum

In the experiment, the optical transition frequency of the D_2 line of nanofiber-trapped atoms is found to be inhomogeneously broadened [38, 72]. The reason for this broadening lies in the state-dependent light shifts of the excited states due to the tensor part of the ac Stark interaction in conjunction with the fact that the trapped atoms are initially not prepared in the same Zeeman substate. We will see in this section that the m_F substates in the excited $6^2P_{3/2}$ state of the trapped atoms are, in general, not good quantum numbers. In order to drive specific optical transitions in the atom, one has to define a convenient quantization axis. Experimentally, this is often achieved by applying an external magnetic field and choosing the quantization axis along this field. It is therefore of interest to study the shift of the energy levels due to the ac Stark interaction in dependence of the Zeeman interaction caused by the external magnetic field. In the following I will calculate the eigensystem of the ground and excited states at the spatial position of the minimum of the trapping potential.

In Fig. 3.5 the decomposition of the eigenvectors $|\psi\rangle$ into the $|F, m_F\rangle$ -basis for the $6^2S_{1/2}$ ground state and the $6^2P_{3/2}$ excited state is shown when no external magnetic field is applied. The eigenvectors are column vectors and are sorted by their eigenenergy. For eigenvectors which have degenerate eigenenergies I used the order that corresponds to the order when a magnetic field is applied which is strong enough to lift the degeneracy of the eigenenergies. For the calculation we considered the coupling of a complete hyperfine multiplet, e.g., $F = 3$ and $F = 4$ for the ground state and $F' = 2$ to $F' = 5$ for the excited state. For the ground state, although there is no magnetic field applied, the eigenstates are well defined: each eigenvector has only one nonzero entry and, thus, m_F is a good quantum number. Note that the negative Landé factor $g_{F=3} = -1/4$ of the $F = 3$ ground state manifests in the order of the eigenvectors. In contrast, for the excited $6^2P_{3/2}$ multiplet [Fig. 3.5 (b)] each eigenvector is a superposition of several sublevels of one hyperfine level and the eigenstates cannot be assigned to a specific m_F . Therefore, m_F is no longer a good quantum number.

In order to suppress the mixing an external magnetic field is applied. In Fig. 3.6, the decomposition of the eigenvectors into the m_F basis for the excited states are plotted for four different values of the magnetic field. In a magnetic field of $B = 3$ G [Fig. 3.6 (b)] m_F is already a good quantum number for the $F' = 2$ state. But it takes a magnetic field of ≈ 10 G to make m_F a good quantum number for $F' = 4$ and $F' = 5$ as well. Nevertheless, for magnetic fields higher

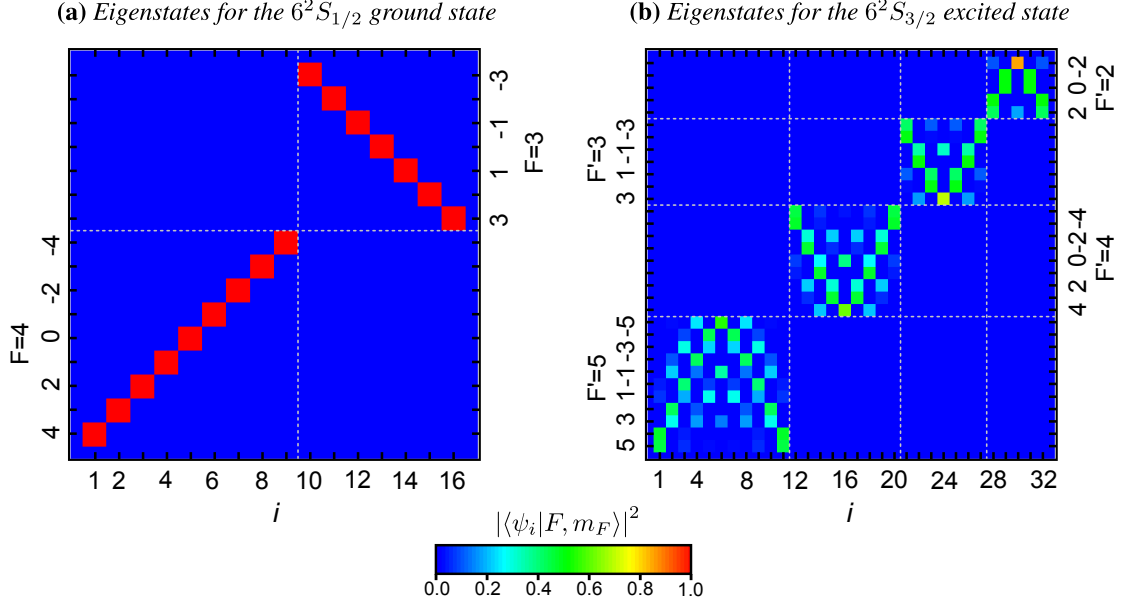


Figure 3.5: Eigenvectors $|\psi_i\rangle$ for (a) the $6^2S_{1/2}$ ground state and (b) the $6^2P_{3/2}$ excited state of an atom that is located at the trap minimum. The eigenvectors decomposed into the m_F basis are presented as column vectors and are sorted by their eigenenergy from left (high) to right (low). The eigenvectors are normalized to 1 and the value of their entries is color-coded. The gray dashed lines separate the eigenvectors for different hyperfine states. There is no external magnetic offset field applied.

than 30 G the levels can no longer be grouped by F as the system leaves the anomalous Zeeman regime and starts to enter the hyperfine Paschen-Back regime [87], i.e., the level shifts due to the Zeeman interaction reach the same order of magnitude as the hyperfine splitting. Note that the mixing of the $F' = 3$ substates is, to first order, not influenced by the magnetic field since its Landé factor $g_{F'=3} = 0$. In this hyperfine state, m_F does not, even for magnetic fields higher than 10 G, become a good quantum number.

In Fig. 3.7 the magnetic field dependence of the corresponding eigenenergies is shown for the ground and excited states of trapped Cs atoms. In Fig. 3.7 (a) and (b), the eigenenergies for the two ground states ($F = 3$, $F = 4$) are plotted. They clearly show the linear dependence one would expect for the Zeeman interaction for low magnetic fields. The shift of the states for $B_{\text{off}} = 0$ is due to the scalar ac Stark interaction of the trapping light fields with the atom.

For the excited hyperfine states, see (c) to (f), the energies of the sublevels are even for zero offset field non-degenerate. This clearly shows the influence of the tensor part of the atomic polarizability. For increasing magnetic fields, the eigenenergy of the sublevels changes: some sublevels are still energetically almost degenerate until for high magnetic fields the linear dependence of the eigenenergy on the magnetic field can be observed, as it is expected for pure Zeeman interaction. Note that the Landé factor is $g_{F'=3} = 0$ for the excited hyperfine state $F' = 3$. Thus, the sublevels do not linearly depend on the magnetic field. For higher magnetic

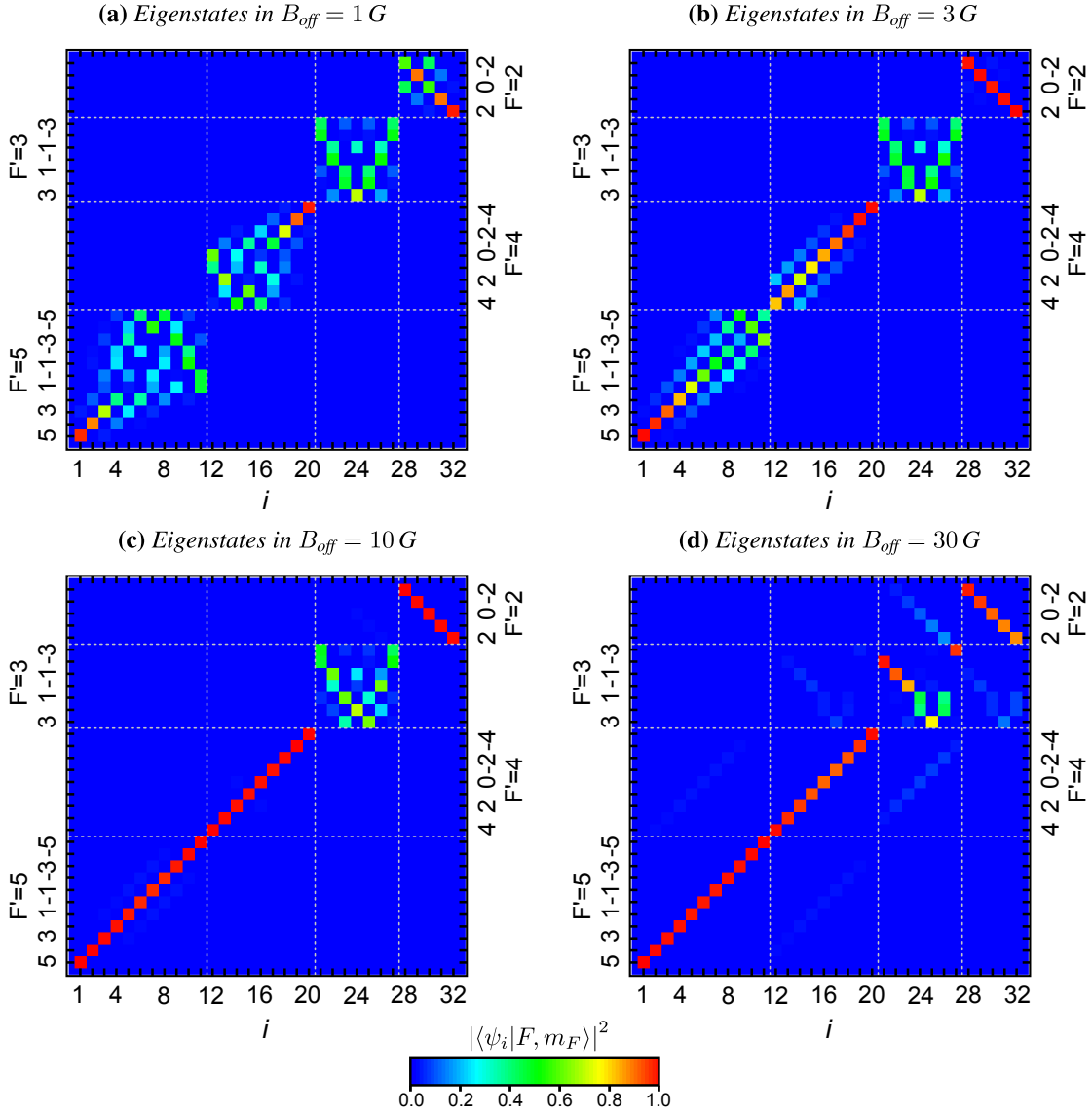


Figure 3.6: Decomposition of the eigenvectors $|\psi_i\rangle$ into the m_F basis for the $6^2P_{3/2}$ excited state in the presence of an external magnetic field of (a) $B_{\text{off}} = 1 \text{ G}$, (b) $B_{\text{off}} = 3 \text{ G}$, (c) $B_{\text{off}} = 10 \text{ G}$, and (d) $B_{\text{off}} = 30 \text{ G}$. The eigenvectors are presented as column vectors and are sorted by their eigenenergy from left (high) to right (low). The eigenvectors are normalized to 1 and the value of their entries is color-coded. The gray dashed lines separate the eigenvectors for different hyperfine states.

fields, however, they show the second order quadratic dependency on the magnetic field.

With these results one can conclude, that, for the ground state of an atom directly at the trapping minimum, the interaction of the atom with the trapping light fields has no severe effects. Since there is no tensor and vector component of the ac Stark interaction, the states are just modified by the scalar component acting on the complete substructure of the $6^2S_{1/2}$ in the same way. However, away from the trapping minimum, the vector component of the ac Stark interaction does not vanish and has to be considered as well [88].

For the excited states, the tensor component plays a major role and the interaction has a severe influence on the optical addressability of these states. However, with a high magnetic field, it should be possible to drive defined Zeeman substate transitions. This is essential for the implementation of quantum protocols in quantum optics experiments. The only exception is the $F' = 3$ manifold which is mixed by the interaction with the trapping light field and not sensitive to the magnetic field in first order. Thus, for this state, m_F is not a good quantum number for any given magnetic field.

3.4 Fictitious magnetic fields

In this section, I will take a closer look on the effect of the vector part of the ac Stark interaction operator (see Eq. (3.13)) on the atoms. The vector part described by the operator

$$V_{\text{vec}}^{EE} = \frac{1}{4} |\mathcal{E}|^2 i\alpha_{nJ}^v \frac{[\mathbf{u}^* \times \mathbf{u}] \cdot \mathbf{J}}{2J} \quad (3.16)$$

only occurs, as stated before, when the light field is to some degree elliptically polarized. Another important fact is, that the vector component can be treated as a fictitious magnetic field [89, 90], meaning that its effect on the atoms adds to the effect of an external magnetic field. The interaction of an atom with a real external magnetic field \mathbf{B} is described by the following Zeeman-Hamiltonian [91]

$$H_{\text{Zeeman}} = -\boldsymbol{\mu} \cdot \mathbf{B} = \mu_B g_J \mathbf{B} \cdot \mathbf{J}, \quad (3.17)$$

where $\boldsymbol{\mu}$ is the magnetic moment of the atom, $\mu_B = \frac{e\hbar}{2m_e c}$ is the Bohr magneton, and g_J is the Landé factor for the fine structure level $|nJ\rangle$. For varying magnetic fields, the second equality is valid if $\boldsymbol{\mu}$ can adiabatically follow the direction of the local magnetic field [84, 92]. Now, the vector part of the ac Stark interaction operator can be written in terms of a fictitious magnetic field \mathbf{B}_{fict} [76]:

$$V_{\text{vec}}^{EE} = \mu_B g_{nJ} \mathbf{B}_{\text{fict}} \cdot \mathbf{J}, \quad (3.18)$$

with

$$\mathbf{B}_{\text{fict}} = \frac{\alpha_{nJ}^v}{8\mu_B g_{nJ}} i [\boldsymbol{\mathcal{E}}^* \times \boldsymbol{\mathcal{E}}]. \quad (3.19)$$

In the special case where the perturbation of the ac Stark effect is small compared to the hyperfine splitting, \mathbf{F} is a good quantum number and Eq. (3.18) takes the form

$$V_{\text{vec}}^{EE} = \mu_B g_{nJF} \mathbf{B}_{\text{fict}} \cdot \mathbf{F}. \quad (3.20)$$

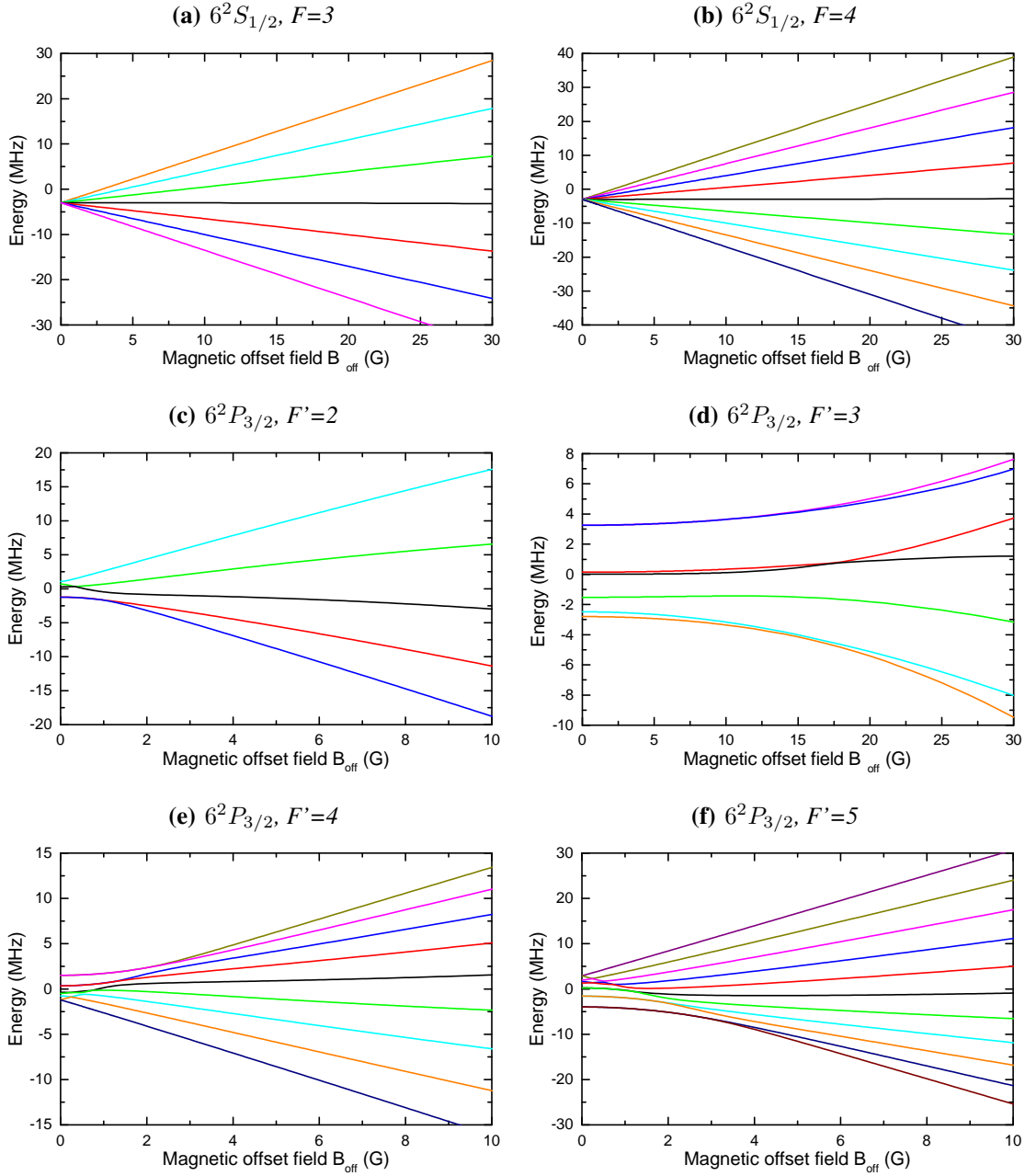


Figure 3.7: Eigenenergies of the Zeeman sublevels in dependency of an external magnetic field for (a) and (b) the hyperfine ground states, and (c) to (f) the hyperfine excited states. For high magnetic fields, the eigenenergies can be identified with the m_F level: black line $m_F = 0$, red line $m_F = +1$, green line $m_F = -1$, blue line $m_F = +2$, cyan line $m_F = -2$, etc. Note that the plot range of B_{off} varies from (a) to (f). For details see text.

The Landé factors that are used in the above equations are given by [76, 93]

$$g_{nJF} = g_{nJ} \frac{F(F+1) + J(J+1) - I(I+1)}{2F(F+1)} \quad (3.21)$$

and

$$g_{nJ} = g_L \frac{J(J+1) + L(L+1) - S(S+1)}{2J(J+1)} + g_S \frac{J(J+1) + S(S+1) - L(L+1)}{2J(J+1)}. \quad (3.22)$$

The orbital and the spin g-factors of the electron are $g_L = 1$ and $g_S \simeq 2.0023193$, respectively. We can conclude from the vector form of Eq. (3.18) and Eq. (3.20) that the fictitious magnetic field simply can be added to any real magnetic field that is present in the system. Note that \mathbf{B}_{fict} depends on J only and is therefore the same for all hyperfine levels in one fine structure manifold $|nJ\rangle$. However, this also means that the fictitious magnetic field exerted by a given external light field is, in contrast to a conventional external magnetic field, different for every $|nJ\rangle$ manifold.

Here, we will investigate the fictitious magnetic field \mathbf{B}_{fict} for cesium atoms that is induced by nanofiber-guided light fields. In section 2.2, we have seen that the light of the evanescent field of the quasi-linearly polarized HE_{11} mode can be elliptically polarized. This fact leads to a fictitious magnetic field. Since for quasi-linearly polarized modes the transverse components of the electric field are in phase with each other and are $\pi/2$ phase shifted with respect to the longitudinal component, it follows that the fictitious magnetic field only has transverse components: $B_{\text{fict},z} = 0$.

In Fig. 3.8 the fictitious magnetic field of a quasi-linearly polarized light field experienced by a cesium atom in the $6^2S_{1/2}$ ground state is plotted. The plot shows the magnitude $|\mathbf{B}_{\text{fict}}|$ as a density plot. The white arrows additionally show the direction of \mathbf{B}_{fict} . Note that \mathbf{B}_{fict} points in opposite direction on opposite sides of the fiber. This follows directly from the fact, that the ellipticity vector $\boldsymbol{\epsilon} = i(\boldsymbol{\mathcal{E}} \times \boldsymbol{\mathcal{E}}^*)/|\boldsymbol{\mathcal{E}}|^2$ of the light field propagating in the fiber points in opposite direction on opposite sides of the fiber.

As shown in Fig. 3.8 (a), $|\mathbf{B}_{\text{fict}}|$ can be as large as 70 G/mW at the surface of the fiber for a light field at 880 nm. At the position of the atoms, there is still a fictitious magnetic field of ≈ 5 G/mW. Taking into account the distance of $\approx 1 \mu\text{m}$ between the atomic ensembles in conjunction with the fact that \mathbf{B}_{fict} points in opposite direction on opposite sides of the fiber, this leads to extreme gradients of up to 100 000 G/mW/cm.

Figure 3.8 (a) shows \mathbf{B}_{fict} for a light field with a wavelength of 880.25 nm, i.e., the tune-out wavelength for Cs. In (b), the same is plotted for the blue-detuned trapping light field with a wavelength of 783 nm. But here, its main direction of polarization is set to be along the y axis. The magnitude of the fictitious magnetic field is reduced by a factor of 25 with respect to \mathbf{B}_{fict} induced by the light field at the tune-out wavelength although the local ellipticities of both light fields is almost the same. This is directly related to the wavelength-dependent vector polarizability, where $|\alpha_{6,1/2,880 \text{ nm}}^v / \alpha_{6,1/2,783 \text{ nm}}^v| \simeq 25$. In addition, one has to take the wavelength-dependent decay constant of the evanescent field at the position of the trapping minimum into account. Note as well, that \mathbf{B}_{fict} points into opposite directions for the two light fields. This stems from the opposite sign of $\alpha_{6,1/2,880 \text{ nm}}^v$ and $\alpha_{6,1/2,783 \text{ nm}}^v$.

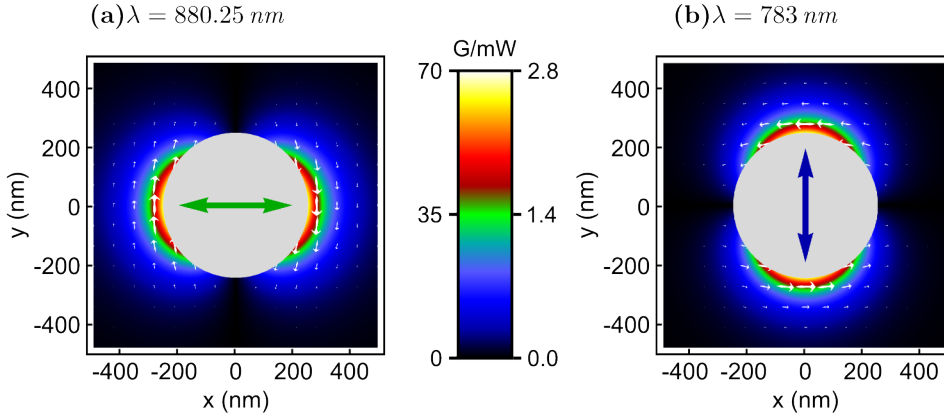


Figure 3.8: The magnitude $|\mathbf{B}_{\text{fict}}|$ of the fictitious magnetic field for a light field with a wavelength of (a) $\lambda = 880.2524 \text{ nm}$ and (b) $\lambda = 783 \text{ nm}$ is presented as a density plot of a cut through the x - y plane. The white arrows show the direction of \mathbf{B}_{fict} . The color scale shows the magnetic field in Gauss per mW of power of the light field sent into the fiber. For (a) the scale shows values from 0 G/mW to 70 G/mW, whereas for (b) the values vary from 0 G/mW to 2.8 G/mW. The green and the blue double arrows show, as in the plots before, the main direction of polarization. The light fields propagate in the z direction.

The blue-detuned trapping light field is purely linearly polarized at the position of the trapping minimum, since its main direction of polarization is along the y axis, see Fig. 3.4 (b). However, there is still a fictitious magnetic field gradient induced by the blue-detuned light field in the azimuthal direction. This magnetic field gradient leads to m_F state-dependent potentials for the ground state, which is thoroughly studied in [88]. Note that the red-detuned trapping light field at a wavelength of 1064 nm exerts no fictitious magnetic field on the atoms: A balanced standing wave formed out of two counter-propagating quasi-linearly polarized modes is purely linearly polarized at every point in space.

In chapter 5, I will discuss how the fictitious magnetic fields induced by nanofiber-guided light fields can be used to manipulate the trapped atoms.

Nanofiber-based trapping and interfacing neutral cesium atoms

4.1 Introduction

A nanofiber-based two-color dipole trap for neutral cesium atoms was suggested in [36, 37] and first experimentally realized in our group [38]. In the meanwhile, several other groups realized this trap as well [46, 49]. This system is well suited for the implementation of quantum hybrid systems [11]. The latter combine the advantages of two worlds: on one side, photons are excellent for transporting quantum information over long distances, and, on the other side, trapped atoms or ions are very well suited for storing and processing quantum information owing to their long coherence times [94–96]. By using the nanofiber trap to interconnect long coherence time systems via optical fiber links, the prerequisites for such a hybrid system can be ideally matched: The atoms are efficiently interfaced with resonant light fields enabling interrogation or manipulation of the atoms. The large optical densities of higher than 10 [38] that are realized with only a few thousand trapped atoms, coherence times in the order of several milliseconds [43], and excellent spatial control [42, 50] are the qualifying properties of this system. Thus, it should be possible to realize devices like quantum memories [15] and quantum repeaters [14, 97] in a quantum network.

In this chapter, I will first present the experimental setup. In particular, I will introduce the different components that are required to realize a two-color nanofiber-based optical dipole trap for neutral cesium atoms. In the next section, I will show how to characterize the trapped atomic ensemble by presenting the experimental methods that are used for measuring their optical density, their lifetime in the trap, the absolute number of trapped atoms, and their coherence times. In this context, I will show that the lifetime and the coherence times of the trapped atoms are interconnected.

4.2 Experimental setup

The experimental setup consists of several parts that will be described in more detail. In the first section, I will present the vacuum setup with the vacuum chamber where the tapered optical fiber (TOF) is mounted. In the next section, I will introduce the magneto-optical trap (MOT) that is used to trap and precool the cesium atoms. In this context I will describe how the atoms are loaded from the MOT into the dipole trap. In the following section, the laser setup that is needed to realize the two-color dipole trap is presented. In the last section, I will describe the detection setup for measuring photons that are resonant with the Cs atoms and are used to probe them.

4.2.1 Vacuum setup

For successful operation of the MOT and the dipole trap, it is mandatory to minimize the collision rate of the trapped Cs atoms with the background gas. Therefore, all the experiments are carried out in an ultra-high vacuum (UHV) environment created in a stainless steel chamber. In figure 4.1 a sketch of the vacuum chamber is shown. The chamber has a volume of approximately 7000 cm^3 [57] and has several CF (ConFlat) flanges. A turbo-molecular pump¹ and an ion getter pump² are used to evacuate the chamber. For standard operation, the turbo-molecular pump is turned off and the vacuum pressure of approximately $5 \cdot 10^{-9} \text{ mBar}$ is sustained by the ion getter pump only. The tapered optical fiber (TOF) is placed in the center of the chamber. The TOF, which waist is $\approx 5 \text{ mm}$ long, has a nominal diameter of 500 nm and is mounted on a holder that can be moved up and down (i.e. in the y direction) with micrometer precision. The feedthrough for the TOF, implemented as a Teflon ferrule with two holes for the fiber going into and out of the chamber, is put in a Swagelok connector [98] to guarantee a sealed chamber.

Three Cs dispensers³ that are used separately to release atomic cesium vapor, are mounted with a T-piece to the chamber. From this background gas, the Cs atoms are trapped and precooled around the nanofiber in the middle of the chamber with a magneto-optical trap (MOT) which will be described in the next section. The other flanges on the vacuum chamber are viewports that are anti-reflection coated for a wavelength of 852 nm and that allow optical access for, e.g., the light fields forming the MOT. Furthermore, a microscope objective [99] is mounted inside the chamber to image the trapped atoms, i.e., to record their fluorescence signal. More details about the vacuum setup can be found in [57, 72].

4.2.2 Magneto-optical trap

The energy of the thermal Cs atoms released by the dispensers is too high to trap them directly in the nanofiber-based dipole trap. Furthermore, since the dipole potential is conservative, a cooling would be required even for atoms that are cold enough. Thus, a magneto-optical trap is used to cool and spatially confine the neutral atoms. The cooling is done optically only by scattering near-resonant light, thereby dissipating the kinetic energy of the atoms: A light field

¹TMU-200-M-P DN-100-CF-F-3P by Pfeiffer Vacuum GmbH

²Starcell 150 Dual by Varian Inc.

³CS/NF/12.8/40 FT 10+10 by SAES Advanced Tech. SPA

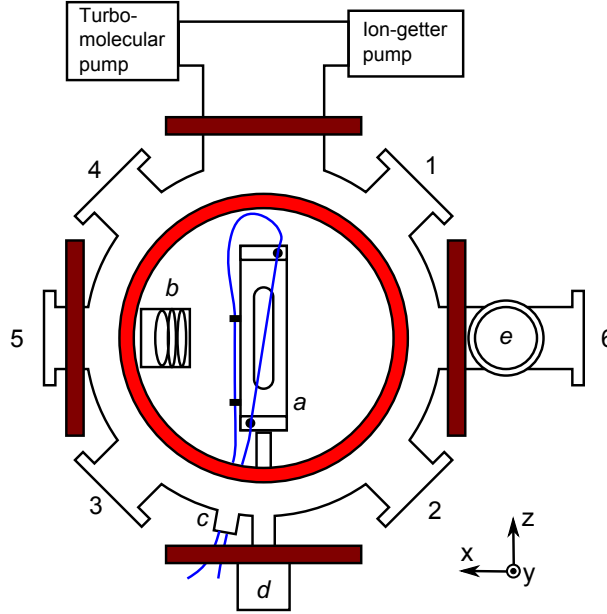


Figure 4.1: Sketch of the vacuum chamber (top view). The TOF (blue line) enters the chamber through c and is glued on a mount a . The mount can be moved in the y direction via the screw d and a joint inside the chamber (not shown). The atoms and the waist of the TOF can be observed through the viewport 5 via a microscope objective b . The Cs dispensers are placed at e . The laser beams creating the MOT enter the chamber through the viewports 1 to 4 and from above and below the chamber, i.e., from the $\pm y$ direction (not shown in the picture). An additional viewport 6 can be used to couple further light fields into the chamber. The red ring represents one of the two coils above and below the vacuum chamber that are used for creating the magnetic field gradient for the MOT. The rectangles in brown are the coils that are used to compensate stray magnetic fields, like the earth magnetic field.

that is slightly detuned from resonance exerts a velocity depending scattering force on an atom. For two counter-propagating light fields and a small atom velocity v , this radiation pressure force is proportional to the velocity: $F_{\text{scat}} = -\beta v$. The damping coefficient β is maximal for red-detuned light fields $\delta = \omega_L - \omega_0 = -\Gamma/2 < 0$, with the frequency of the light field, ω_L , and the frequency of the atomic transition, ω_0 . The scattering force thus acts as a friction that decelerates the atom and cools it. The system of two counter-propagating beams can be easily expanded in three dimensions by employing six beams from all three directions of space and, therefore, forming a so-called three-dimensional optical molasses [93].

In conjunction with an inhomogeneous field $B = B' \cdot z$, the atoms can not only be cooled but additionally spatially confined. In Fig. 4.2, the principle of the confinement is shown in one dimension for two counter-propagating beams: The inhomogeneous magnetic field is, for example, negative for $z < 0$ and positive for $z > 0$. For the excited state of an atom with, e.g., $J_e = 1$, the magnetic sublevels are split due to Zeeman interaction. A σ^+ -polarized light field with a frequency ω_L that is red-detuned with respect to the free space atomic resonant

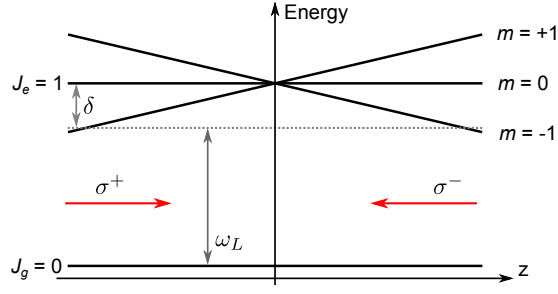


Figure 4.2: Principle configuration for a MOT in one dimension. The solid lines are the atomic levels for the ground ($J = 0$) and the excited ($J = 1$) state. The substates are shifted due to the inhomogeneous magnetic field. The red arrows represent the σ^\pm -polarized light fields propagating along the $\pm z$ direction, respectively. The dashed line represents the frequency ω_L of the light fields that is detuned by δ from the atomic resonance at the center of the trap.

$\delta = \omega_L - \omega_0$ is propagating along the $+z$ direction. If the atom is positioned at $z < 0$, it experiences a restoring force towards $z = 0$ since the σ^+ -polarized light that drives the shifted $|J_g = 0, m_J = 0\rangle \rightarrow |J_e = 1, m_J = +1\rangle$ transition is resonant with the atom. If the atom is placed at $z > 0$, it is resonant with the σ^- -polarized light field propagating in the $-z$ direction. Thus, the atom experiences again a force towards $z = 0$ which leads to spatial confinement. This concept can be expanded to three dimensions using the six laser light beams for the optical molasses and a magnetic quadrupole field that has its zero in the center where the six beams cross each other. Note that this scheme is not limited to the simple level scheme that is described here but also works for any $J_g \rightarrow J_e = J_g + 1$ transition. [93].

In our system the cooling light field is provided by a commercially available laser system⁴, composed of a frequency-seeded tapered amplifier. The frequency of this laser is stabilized to atomic cesium via a Doppler-free saturation spectroscopy [100]. The frequency of this light field is slightly red-detuned with respect to the $F = 4 \rightarrow F' = 5$ transition of the D_2 line. Due to off-resonant excitations, it is possible that the cooling light field excites the atoms to the $F' = 4$ level from where they can decay to the $F = 3$ ground state and where they are consequently lost from the cooling cycle. Therefore, a repumping laser⁵ light, which is resonant with $F = 3 \rightarrow F' = 4$ transition, is needed. This laser is stabilized via a polarization spectroscopy [100] on the desired transition. The light fields of both lasers are overlapped and coupled into a so-called “fiber port cluster”⁶. In the cluster, the beams are split into six beams and are balanced in power. Optical fibers guide the six light fields to the six viewports, where the beams are sent into the vacuum chamber crossing each other in the center of the chamber. The beams have $1/e^2$ -diameter of 13 mm [72] and the total powers are 70 mW and 220 μ W for the cooling and the repumping light fields, respectively.

The magnetic quadrupole field for the MOT is provided by two coils placed above and below

⁴The tapered amplifier is a TEC400 and the seeding laser is a TEC500, both manufactured by Sacher Lasertechnik GmbH.

⁵Lynx TEC100 manufactured by Sacher Lasertechnik GmbH

⁶Fiber port cluster 1 to 6 for 852 nm by Schäfter + Kirchhoff

the chamber that are in anti-Helmholtz configuration. While operating the MOT, they provide a maximal magnetic field gradient of 3.5 G/cm at 8 A [101]. Since the experiment is not shielded from external magnetic fields, like the magnetic field of the earth, they have to be compensated for. For this purpose, there are two magnetic field coils in the x direction and two magnetic field coils in the z direction. In the y direction, we directly move the fiber with the translation stage to the position of the atoms in the MOT.

In order to load the atoms from the MOT into the fiber-based dipole trap, the magnetic quadrupole field is ramped down and the cooling laser is further red-detuned from resonance. With this standard technique which is typically used to load steep dipole traps, the temperature of the atoms in our trap is reduced from $\approx 100 \mu\text{K}$ in the MOT to $\approx 28 \mu\text{K}$ in the dipole trap [72]. For further details on the MOT setup, see [57, 72, 101].

The two magnetic field coils that provide the magnetic quadrupole field for the MOT can be switched electronically to Helmholtz configuration. Thus, they can also provide a homogeneous magnetic offset field along the y axis with a magnitude of maximally $B_{\text{off}} = 28 \text{ G}$. Although the two coils are not geometrically in Helmholtz configuration, the magnetic field in the middle of the chamber, i.e., at the position of the trapped atoms, is approximately homogeneous [101].

4.2.3 Nanofiber-based dipole trap

To realize the nanofiber-based dipole trap, we use a far blue- and a far red-detuned light field, as described in section 3.3. The red-detuned light field has to be sent into the fiber from both directions to create a standing wave. In addition to these light fields, we use resonant and near-resonant light fields to probe and manipulate the trapped atoms. They all have to be combined so that they can be coupled simultaneously into the TOF. When they leave the TOF again, they have to be split up so that only the resonant probe light field can be detected. Each light field can be turned on and off separately and its power can be controlled via an AOM.

The TOF is not polarization maintaining since it is produced from a non-polarization maintaining fiber. In particular, the birefringence in the taper region alters the polarization of any guided light field. In order to ensure that the light fields are quasi-linearly polarized at the waist of the TOF, we provide the following measures: First, the polarization of the light is made purely linear before coupling it into the TOF. This linear polarization can be turned via a halfwave plate. Then, the light field passes through a Berek compensator [102] and is then coupled in the TOF. With this plate, we can precompensate for the birefringence of the fiber, i.e., set the polarization of the light field in a way that it is quasi-linearly polarized at the waist of the TOF.

In figure 4.3, a sketch of the beam paths for the two trapping laser fields is shown. The red-detuned light field with a wavelength of 1064 nm is provided by a Nd-YAG laser⁷. The light field is split by a polarizing beam splitter (PBS₂) and sent from both sides into the TOF. The powers of the two light fields propagating in opposite directions through the fiber are balanced via a halfwave plate (HW₁) in front of PBS₂. The polarization of both light fields is “cleaned” to be purely linear by two polarizers (PBS₃ and PF₁⁸).

⁷Excelsior 1064-650 manufactured by Spectra Physics

⁸LPVIS 050-MP by Thorlabs Inc.

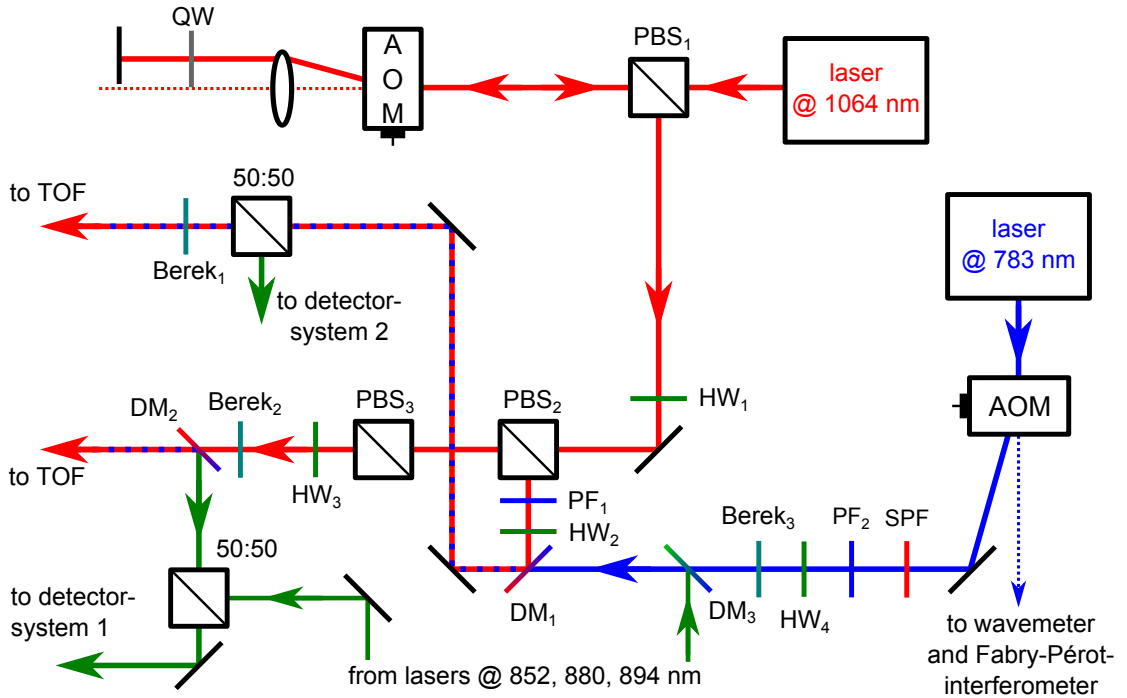


Figure 4.3: Simplified sketch of the beam paths for the red- and blue-detuned trapping light fields. The sketch shows the following optical elements: acousto-optical modulators (AOM), polarizing beam splitters (PBS), non-polarizing symmetric beam splitters (50:50), Berek compensator plates (Berek), half- and quarterwave retardation plates (HW and QW), polarization filter (PF), short-pass filter (SPF), and dichroic mirrors (DM).

The blue-detuned light field at a wavelength of 783 nm is provided by a diode laser⁹. Its polarization is controlled by a polarization filter (PF₃), a halfwave plate ($\lambda/2_4$), and a Berek compensator (Berek₃), in order to ensure quasi-linear polarization at the waist of the TOF. The blue-detuned light field is overlain with the red-detuned light field with a dichroic mirror (DM₁). Before that, it passes a short-pass filter (SPF)¹⁰, in order to block the amplified spontaneous emission background of the laser diode that is resonant with the D-lines of atomic cesium.

Additional light fields, which are resonant or close to resonance with the D-lines of Cs can be coupled into the TOF via a dichroic mirror (DM₃)¹¹. Then, these light fields have the same propagation direction as the blue-detuned light field. To have these light fields counter-propagating with respect to the blue-detuned light field, they can be coupled into the TOF with a 50:50 beam splitter. The polarizations of these light fields are as well controlled by $\lambda/2$ -plates and Berek compensators (not shown in Fig. 4.3). The light that is resonant with the atoms and coupled out of the two ends of the TOF is directed to two detectors, respectively.

⁹DL100/02479 manufactured by Toptica Photonics AG

¹⁰XIS0810-Shortpass by Asahi Spectra, with a transmission of 89,6 % at 783 nm

¹¹DMSP 805 by Thorlabs Inc.

Obtaining quasi-linearly polarized light in the nanofiber

In this section I will briefly introduce the method that is used to align the polarization of light fields that are launched into the TOF so that they are quasi-linearly polarized at the nanofiber. It relies on the detection of light that is scattered by imperfections at the surface of the nanofiber and inhomogeneities in the bulk silica. Here, we assume that the imperfections are point-like dipole emitters so that the local polarization of the fiber-guided mode is conserved. We record the Rayleigh-scattered intensity in a direction orthogonal to the fiber with a CCD camera. Using the example of the blue-detuned light field, we obtain a sinusoidal signal with the camera by turning its main axis of polarization with a half-wave plate (HW_4 in Fig. 4.3). The visibility of this Rayleigh-scattered pattern is a direct measure of the linearity of the polarization and is increased by tilting the Berek compensator (Berek_3) that thus compensates for the birefringence of the TOF. By reaching maximal visibility, we therefore have the best possible approximation of quasi-linearly polarized light at the nanofiber. We use this method as well to fix the main direction of polarization of the nanofiber-guided light fields. The direction can be aligned with a precision of a few degrees at best. Here, systematic errors, like the numerical aperture of the camera that always provides a finite azimuthal resolution, play a crucial role. More details on this method can be found in [39]. In chapter 5.4, I will present a method that can be performed additionally in order to obtain an even higher control of the polarization of the nanofiber-guided light fields.

4.2.4 Detection system

Since the light that propagates in the nanofiber is strongly transversely confined, the intensity in the evanescent field is very high: already a few hundred pW is sufficient to reach saturation intensity at the position of the trapped atoms. Therefore, we only use very weak light fields on the order of a few pW of optical power to probe the atoms. For the detection of these weak light fields, which are resonant with the D_2 line, there is one single photon counter module (SPCM)¹² placed at each output of the TOF. To prevent non-resonant light to get to the SPCM, the light is filtered by several stages. First, we use dichroic mirrors which reflect the red-detuned trapping light field at 1064 nm and transmit only shorter wavelengths. To block the blue-detuned trapping light field at 783 nm as well, there is a band-pass filter¹³ around 852 nm with full width at half maximum (FWHM) of its transmission of 12.5 nm. With these measures, all the photons that are far from resonance can be filtered out.

However, a major issue is the presence of resonant and near-resonant photons. These photons stem from Raman scattering processes in the glass fiber itself induced by the blue-detuned trapping laser field at 783 nm. In general, when photons undergo an inelastic scattering process with molecules they can emit so-called Stokes photons having a lower energy than the incident photons [100]. In a solid material, the energy difference of the incoming photon and the Stokes photon is carried away by phonons in the material. The energetic shift of the Stokes photons relative to the energy of the incident or pump photons is called Stokes shift and is a material-

¹²SPCM-AQRH-14-FC by Excelitas Technologies GmbH & Co.KG

¹³Semrock LL01-852-12,5 (MaxLine Laser Line Filter)

dependent property. For a silica-core single mode fiber the spectrum for Stokes shifted photons is given in [103].

In our group¹⁴ the Raman Stokes spectra for the same type of fiber that is used here, the Liekki Passive 6/125, has been measured. From these measurements, the characteristic value of Stokes photons at the resonance of cesium (852 nm) turns out to be (0.04 ± 0.01) pW/(m·mW·nm) for pump photons with a wavelength of 783 nm. This means, for each milli-Watt of power of the blue-detuned trapping light field inside the fiber, we get 0.04 pW of Raman light at 852 nm per meter of optical fiber per nanometer wavelength interval in the region around 852 nm. The same amount of light counter-propagates with respect to the propagation direction of the blue-detuned light field because the spontaneous Raman scattering process is isotropic.

Without any filter, these Stokes photons would produce a large background of several tens of pW per mW of power of the blue-detuned light field on all the signals that should be measured with the SPCMs. Therefore, a volume Bragg grating¹⁵ (VBG) was inserted in the beam path that leads to the detectors. It replaces a line filter [104] used in previous experiments [101]. The reflection Bragg grating has a very high on-resonance transmission of 94 % and a spectral width of only 0.12 nm [105]. Thanks to the VBG, we could reduce the amount of detected Stokes photons to only 0.10 ± 0.01 photon per mW of the blue-detuned trapping light field in a time window of $1 \mu\text{s}$. This matches very well with the Raman Stokes spectrum taken independently¹⁴: with the fiber length of 5 m, one predicts 0.10 ± 0.03 photons per mW of the blue-detuned trapping light field in $1 \mu\text{s}$ in a spectral window of 0.12 nm. With these measures, the amount of background photons is suppressed to a level, at which the SPCMs are not saturated by Stokes photons and a signal of a few pW can be easily distinguished from the background level.

4.3 Characterization of nanofiber-trapped atoms

The theoretical description of a nanofiber trap has been given in the previous chapters. In this section, I will characterize the trapped atoms. Figure 4.4 shows a sketch of the parts of the experimental setup that are needed for trapping and manipulating the atoms with light fields, microwave (MW) radiation, and external magnetic fields.

The atoms are strongly confined in the two linear diametric arrays of trapping sites along the fiber. Due to the strong confinement of the atoms, the interaction of nanofiber-guided light fields and the trapped atoms takes place in the Lamb-Dicke regime (Lamb–Dicke parameter: $\eta < 0.11$). Due to the collisional blockade effect [106] during the molasses phase while loading the dipole trap, there is at most one atom per trapping site and a mean occupation number of at most 0.5 atoms per trapping site can be reached [39]. The initial temperature of the trapped atoms corresponds to a low mean motional quantum number on the order of $\langle n \rangle = 3$ and results in a small trapping volume [39].

¹⁴Project work by Daniel Weiss, 2013

¹⁵RBG-582-94 #Q06-34-A3 manufactured by OptiGrate Corp.

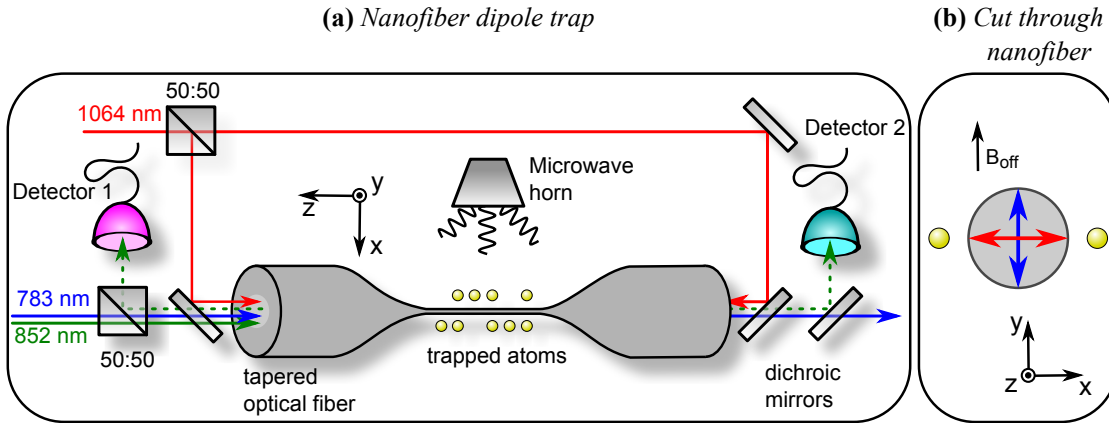


Figure 4.4: Simplified sketch of the experimental setup. In (a) the tapered optical fiber (TOF), the laser beam paths, and the trapped atoms (yellow spheres) at the waist of the nanofiber are shown. Detector 1 (2) measures the light that propagates in the $+z$ ($-z$) direction. The microwave radiation (MW) is tunable around the transition frequency of the two hyperfine ground states. (b): transverse cut through the nanofiber. The red and the blue arrow show the main direction of polarization of the red-detuned and the blue-detuned quasi-linearly polarized trapping light fields, respectively. An external magnetic offset field B_{off} can be applied along the y direction.

4.3.1 Spectroscopy and saturation

An important method to obtain information about the trapped atoms is transmission spectroscopy. To obtain such a spectrum, the transmission of a resonant light pulse at a given frequency is measured. After averaging this signal for several experimental runs, the frequency of the light pulse is changed and its transmission is again measured. In this manner, the frequency is scanned over the $|F = 4\rangle \rightarrow |F' = 5\rangle$ transition of the D_2 line. In Fig. 4.5 (a), a typical transmission spectrum is shown. The center of the spectrum is significantly shifted (by ≈ 9 MHz) with respect to the free-space resonance, due to light shifts of the ground and excited state induced by the ac Stark interaction. As seen in chapter 3.3.2, the magnetic sub-states of the $F' = 5$ level are energetically splitted. Thus, for fitting this inhomogeneously broadened spectrum, all possible transitions have to be taken into account. The fit function is therefore the sum of several saturated Lorentzian line profiles describing the different transitions taking into account their relative strengths. This fit directly returns an optical density of $\text{OD} = 13 \pm 2$ [38].

The OD depends on the coupling efficiency of the nanofiber-guided light field to the atoms. This efficiency is related to the local intensity at the atomic position and thus depends crucially on the radial distance of the trapped atoms to the fiber. Furthermore, it depends on the strength of the driven transition and on the main direction of polarization of the guided mode because the intensity of the quasi-linearly polarized HE_{11} mode varies strongly in the azimuthal direction, see chapter 2. Due to the finite temperature of the atoms, their position cannot be determined directly. The OD is therefore not a reliable measure to determine the absolute atom number. Nevertheless, for one given set of parameters (power, polarization, and propagation direction of

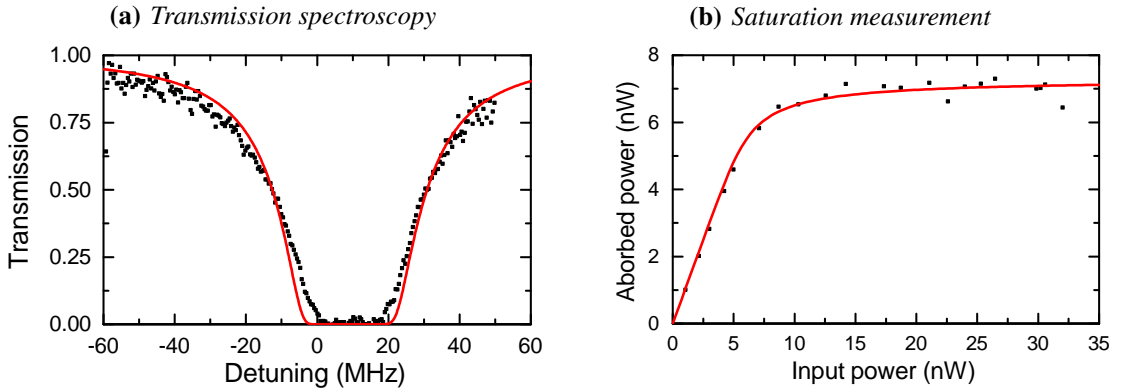


Figure 4.5: (a) Transmission spectrum of nanofiber-trapped atoms. The transmission is recorded in dependency of the frequency detuning of the probe with respect to the free-space resonance. The red line is a fit taking all possible light-shifted transitions between the $F = 4$ state and the $F' = 5$ state into account. (b) Saturation measurement to determine the absolute number of trapped atoms. The amount of absorbed and scattered power is plotted in dependency of the power of a resonant light pulse that is sent into the fiber. The red solid red line is a fit that yields the total atom number, here ≈ 2000 . These figures are taken from [38].

the trapping light fields) the OD is proportional to the atom number and we thus use this method routinely in our experiments after an initial calibration measurement, see below.

A typical experimental sequence in which the transmission spectroscopy is used is structured in the following way: After loading the atoms from the magneto-optical trap into the dipole trap, they are optically pumped into the $F = 4$ ground state manifold. Then, we record a transmission spectrum by scanning the frequency of the probe light field within a typically 5 ms-long pulse over ≈ 100 MHz over the $F = 4 \rightarrow F' = 5$ transition. Here, we perform a frequency sweep in order to obtain the optical density within one experimental run. Next, the desired experiment is performed. For example, the atoms are transferred from one hyperfine ground state to the other by exposing them to microwave (MW) radiation. Subsequently, another transmission spectrum of the $F = 4$ manifold is recorded. The optical density obtained from this spectrum is proportional to the number of atoms in this manifold and yields the actual signal, i.e., how many atoms have been transferred via the MW-pulse from $F = 4$ to $F = 3$. Furthermore, by taking the ratio of the optical densities obtained by the transmission spectra at the beginning and the end of the sequence, the effect of shot-to-shot fluctuations of the atom number in our trap is canceled.

Saturation measurement

In order to determine the absolute number of trapped atoms, it is necessary to perform a saturation measurement: A short ($\approx 2 \mu\text{s}$ -long) resonant light pulse is sent into the nanofiber and its transmission is recorded. We compare this transmission with the transmission of a reference light pulse that is sent through the fiber without atoms in the dipole trap. Thus, we can deter-

mine the amount of light that is absorbed and scattered by the trapped atoms. The power of the light pulses is increased in different experimental realizations. In this manner, we record the amount of absorbed and scattered light by the atoms in dependency of the input power. In Fig. 4.5 (b), the outcome of such a saturation measurement is shown. The data points can be described by a generalized Beer-Lambert law [38, 72] that takes into account the varying power of the light field due to absorption along the atomic ensemble. A fit of this function yields that the absorbed power saturates at ≈ 7.3 nW. From the fact that a single fully saturated Cs atom radiates about $P_{\text{Cs}} = 3.8$ pW of optical power, we can conclude that ≈ 2000 atoms were trapped and contributed to the signal.

Lifetime

The mean time the cesium atoms remain trapped in the nanofiber-based trap is an important time scale. To determine this lifetime, the OD of the atomic ensemble is measured for different waiting times after the loading of the dipole trap. Note that although the OD might not be a good measure since the temperature of the atomic ensembles is changing throughout the measurement, the experimental data can be well described by the expected exponential decay. Fig. 4.6 shows a typical outcome of such a measurement. The data points are fitted with an exponential decay $f(t) = e^{-t/\tau}$, returning the decay constant τ as the characteristic lifetime of the trapped atoms. In this figure, the lifetimes of the atoms in two different trapping configurations is shown. The lifetime for a trap depth of $354 \mu\text{K}$, corresponding to the trap presented in [38], is $\tau = 57 \pm 2.7$ ms. For a more shallow trap with a depth of $157 \mu\text{K}$, the lifetime was found to be $\tau = 170 \pm 3.8$ ms. The different trap depths have been obtained by proportionally changing the power of the blue-detuned trapping light field P_{Blue} and the power of the red-detuned trapping light field P_{Red} , i.e., $P_{\text{Blue}}/P_{\text{Red}} = \text{const.}$ The powers to obtain the trapping potential presented in [38] with a depth of $354 \mu\text{K}$ are $P_{\text{Blue}} = 25$ mW and $P_{\text{Red}} = 2.2$ mW per beam for the standing wave.

The dependency of the lifetime on P_{Blue} is shown in Fig. 4.7. One can see that the lifetime is almost constant at ~ 50 ms for $P_{\text{Blue}} > 20$ mW. For lower powers, the lifetime increases up to ~ 170 ms. For the two data points on the very left the error on the lifetime is much bigger than for the other measurements: for these shallow traps almost no atoms could be trapped anymore, so the signal was very weak.

The lifetime we expect from losses due to collisions with the background-gas is on the order of seconds [107]. A possible explanation for the deviation of this value and our experimental results can be given by considering the mechanical vibration modes of the fiber in conjunction with the anharmonicity of our trap: In typical tapered optical fibers there exist high- Q torsional modes (Q -factor of $\approx 2.5 \cdot 10^4$) that are thermally excited [74, 108]. The frequency of the fundamental torsional mode depends on the shape of the taper transition and the length of the waist of the TOF and is ≈ 150 kHz for our fiber radius profile. This mechanical vibration optomechanically couples to the nanofiber-guided light fields. In our case, the blue- and the red-detuned trapping lasers then can exhibit polarization and phase fluctuations at a few hundred kHz. Since the trapping potential is anharmonic, the trap frequencies are not “sharp” and well defined, but can be better described as frequency bands. Therefore, it is very likely that the high- Q torsional modes lie in such a frequency band. Thus, due to the coupling of the torsional modes

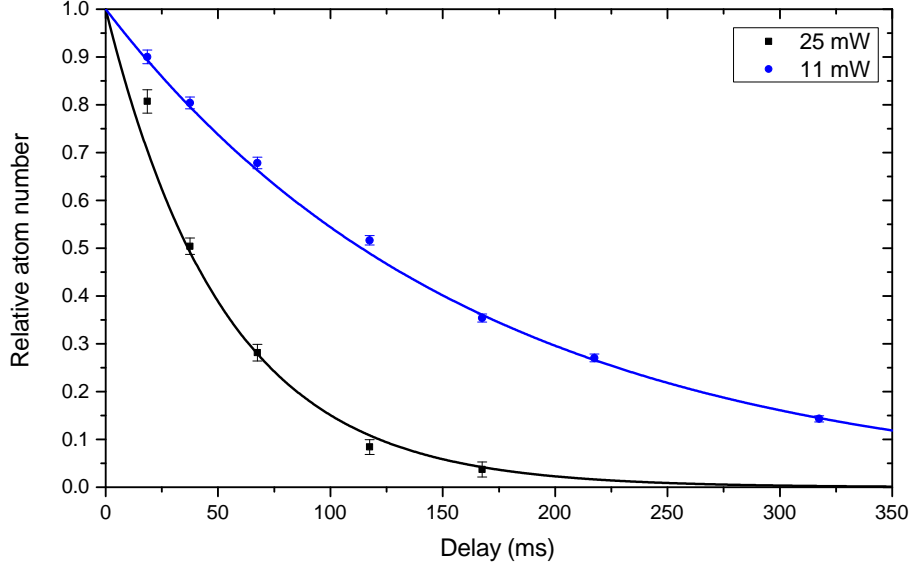


Figure 4.6: Measurement of the lifetime of the atoms in the dipole trap. The relative atom number is plotted as a function of the time the atoms were stored in the trap. The solid lines are fits by an exponential decay returning the characteristic decay constant. The black (blue) data points are lifetime measurements for atoms in a trap obtained with $P_{\text{Blue}} = 25 \text{ mW}$ ($P_{\text{Blue}} = 11 \text{ mW}$) yielding a lifetime of $\tau = 57 \pm 2.7 \text{ ms}$ ($\tau = 170 \pm 3.8 \text{ ms}$). Each data point has been averaged over 40 experimental realizations.

to polarization of the trapping light fields and therefore to the azimuthal degree of freedom, a heating of the atoms would be inevitable and the lifetime of the atoms in our trap would be limited.

The presence of these torsional modes might be an explanation of the drastic change of the lifetime in dependency of the trap depth as well. In order to change the trap depth, the powers of the red and the blue trapping light fields have to be varied. This leads to a change of both the trap frequencies and the frequencies of the torsional modes: The trap frequencies change because the curvature of the potential changes when the trap depth is changing. The frequency of the torsional mode depends on the properties of the nanofiber, like its length or its elastic modulus. Both properties are depending on the temperature which is changed when the power of the blue-detuned trapping light field is varied by tens of mW [109]. In the measurement presented here, the power of the blue-detuned light field varied from 4 mW to almost 40 mW. Thus, by changing the powers of the trapping light fields, the band of trap frequencies might move in frequency space and, at some point, overlaps with the well-defined frequency of a torsional mode. In this case the atoms would start to get heated more efficiently.

A final answer to the question of the cause of the drastic change in lifetime can only be given by further experiments and thorough simulations of the trap frequencies. In the following, we simply made use the fact that the lifetime is strongly increased for lower trapping powers. Accordingly, we chose the powers of the trapping light fields to be 8.5 mW for the blue-detuned

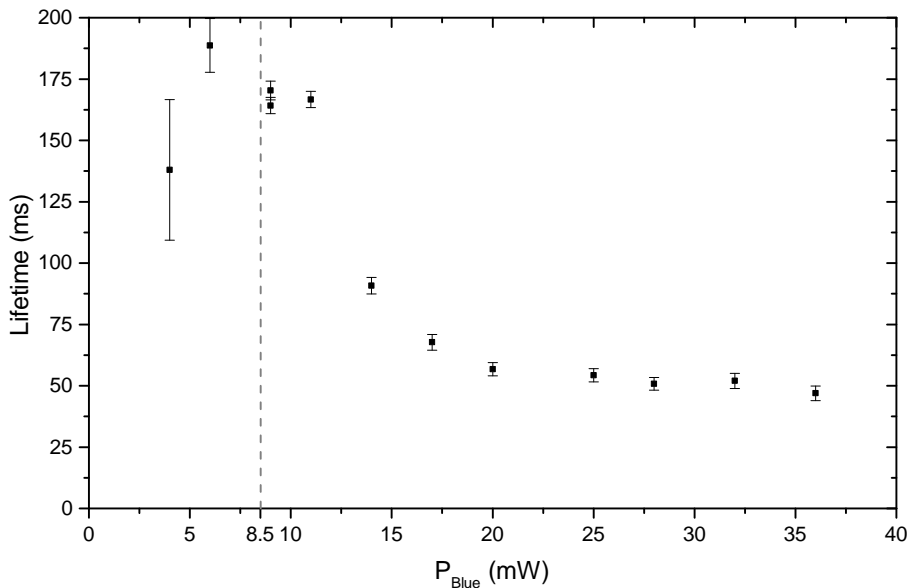


Figure 4.7: Measured lifetime of the trapped atoms as a function of P_{Blue} . The dashed line indicates the power $P_{\text{Blue}} = 8.5$ mW that is used in the following.

light field and 0.77 mW per beam for the red-detuned standing wave, yielding a trap depth of ≈ 140 μK .

4.3.2 Coherence properties

In order to perform quantum optics experiments and to use our system, e.g., for storing quantum information, it has to exhibit good coherence times. In general, the proximity to the nanofiber and the possible presence of, e.g., patch potentials [110] and Johnson noise [111] might hamper good coherence properties. But despite these objections we demonstrated that this system has good ground state coherence times in the order of milliseconds [43].

We use a tunable microwave (MW) field at 9.2 GHz to drive transitions between the two cesium hyperfine ground states. A MW horn positioned outside the vacuum chamber directs the MW radiation to the trapped atoms. The measurements of the ground state coherence times presented in the following were performed on the $|F = 3, m_F = 0\rangle \rightarrow |F = 4, m_F = 0\rangle$ clock transition, i.e., the least magnetic field-sensitive transition, and should thus yield the highest coherence times. In order to lift the degeneracy of the magnetic sublevels, an external magnetic offset field is applied along the y axis. The magnetic field is provided by the same coils that are used to supply the quadrupole field for the MOT. To provide the homogeneous magnetic field, the coils are switched from anti-Helmholtz configuration to Helmholtz configuration. In addition, the magnetic field is necessary to prevent the atoms to change their internal state: In our trap the atoms move in state-dependent potentials due to strong fictitious magnetic field gradients induced by the vector light shift of the blue-detuned trapping light field [88]. The fictitious magnetic field exhibits a strong gradient with a zero-crossing. At this point, the ground

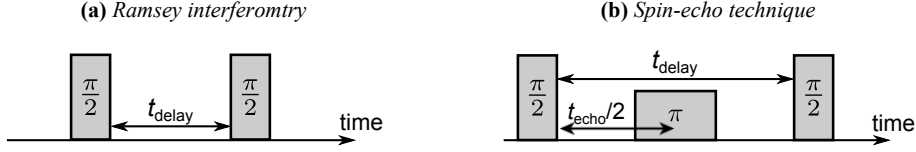


Figure 4.8: (a) Principle of Ramsey interferometry: Atoms, initially prepared in the $|F = 3, m_F = 0\rangle$ state, are prepared in a superposition with $|F = 4, m_F = 0\rangle$ by means of a first MW $\pi/2$ pulse which is near-resonant with the corresponding transition. After a waiting time t_{delay} , the atoms are subjected to a second MW $\pi/2$ pulse. Finally the population in $|F = 4, m_F = 0\rangle$ is measured. (b) Principle of the spin-echo technique: Between the two MW $\pi/2$ pulses a π pulse is applied leading to a rephasing of the atomic spins. At $t_{\text{delay}} = t_{\text{echo}}$ the atomic spins have rephased and a revival of the Ramsey fringes is expected.

state potentials are degenerate. Thus, spin flips between adjacent magnetic sublevels occur. These spin flips can be prevented by applying a magnetic offset field [88], which removes the degeneracy point of the ground-state potentials. Experimentally, we found that a homogenous field of 3 G is sufficient to avoid spin flips [43].

From Ramsey interferometry performed on the clock transition, we deduced the reversible dephasing time T_2^* . For this measurement, the population transfer from the $|F = 3, m_F = 0\rangle$ to the $|F = 4, m_F = 0\rangle$ state was measured in dependency of the time between two MW $\pi/2$ pulses [see Fig. 4.8 (a)]. The resulting fringes decay in a characteristic time $T_2^* = 0.6$ ms [43]. This time is limited by an inhomogeneous broadening mechanism of the clock transition. The broadening stems from the finite initial temperature of the atoms in the trap in conjunction with a vibrational-state-dependent transition frequency: Atoms that occupy different vibrational states accumulate different phases while evolving during the Ramsey measurement leading to a decrease of the amplitude of the fringes [43]. We showed that this dephasing is reversible by means of the spin-echo technique [see Fig. 4.8 (b)]: A MW π pulse is applied in between two $\pi/2$ pulses at a certain time $t_{\text{echo}}/2$. With this technique, it is possible to induce a revival of the Ramsey fringes at t_{echo} . The amplitudes of the echo signals decrease with increasing echo times t_{echo} . The decay constant of the amplitudes corresponds to the irreversible dephasing time T_2' .

Figure 4.9 shows the evolution of the coherence $\mathcal{C}(t)$ as a function of the echo time as presented in [43]. In this context, the quantity $\mathcal{C}(t)$ is a measure of the coherence of the superposition of $|F = 3, m_F = 0\rangle$ and $|F = 4, m_F = 0\rangle$ that can vary between 0 and 1, and is obtained by fitting the amplitudes of the spin echo signals and by theoretically modeling the evolution of the density matrix of the atomic states (for details see [43]). From this measurement, we can infer the irreversible dephasing time, T_2' , to be larger than 3.7 ms. The loss of coherence is directly related to the heating rate in our system. A simulation of the evolution of the coherence that assumes a heating rate of 3 mK/s is also shown in Fig. 4.9.

In continuation of the experiments presented in [43], Fig. 4.9 also shows the coherence derived from the result of the spin-echo measurement for a trap with a depth of 140 μK (i.e., $P_{\text{Blue}} = 8.5$ mW and $P_{\text{Red}} = 0.77$ mW per beam). As expected, the coherence is preserved for longer times since the heating rate is lower. A detailed analysis of the coherence time depending

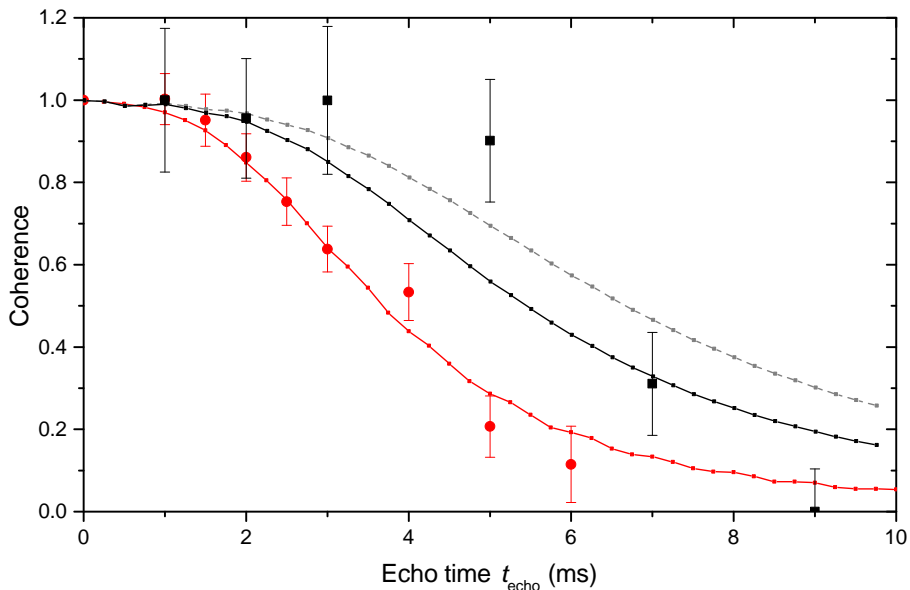


Figure 4.9: Comparison of the evolution of the coherence depending on the echo time for a trap with a depth of $\approx 400 \mu\text{K}$ (large red disks) and with a depth of $140 \mu\text{K}$ (large black squares). The small red squares are obtained by simulating the coherence for a heating rate of 3 mK/s as in [43]. The small black squares and the dashed gray squares are obtained by simulating the coherence for the shallow trap for a heating rate of 0.4 mK/s and 0.8 mK/s , respectively.

on the trapping light fields is beyond the scope of this thesis, but we can already conclude that these measurements are in agreement with the fact that, here, the heating rate must be significantly lower than for the trap with shorter lifetime. In Fig. 4.9, the evolution of the coherence is simulated for a heating rate of 0.4 mK/s and 0.8 mK/s describing the data much better than a heating rate of 3 mK/s .

4.3.3 Manipulation of first order magnetic field-sensitive states

Adiabatic rapid passage

An alternative way to transfer population between $|F = 3, m_F\rangle$ and $|F = 4, m_F\rangle$ employs the so-called “adiabatic rapid passage” (ARP). Compared to a transfer of population that is achieved by applying a microwave π -pulse, ARP is very robust against fluctuations of experimental parameters like the resonant Rabi frequency Ω_0 and the detuning δ . For example, in the case of broadened transitions for which a π -pulse is not efficient, it is still possible to transfer almost 100 % of the population via ARP [112].

To explain how ARP works [113], let us consider the interaction between a two-level atom

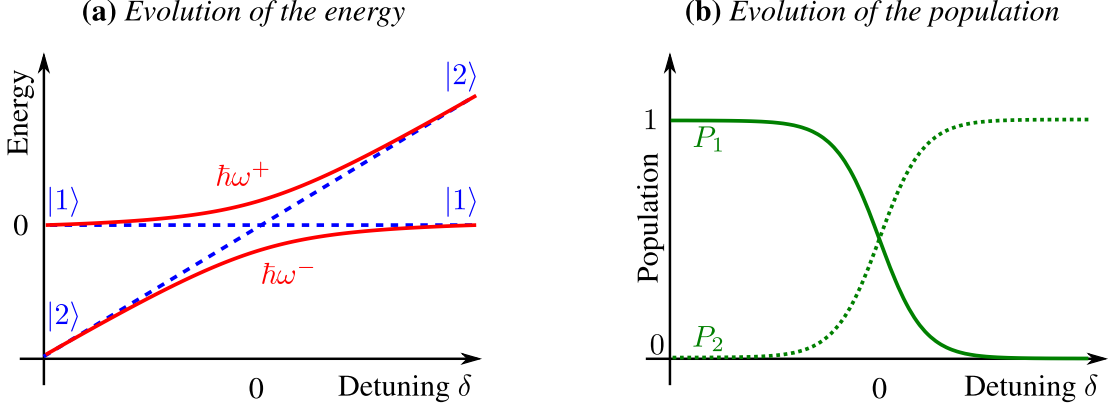


Figure 4.10: (a) The energy of the dressed states (solid red lines) and the bare states (blue dashed lines) plotted as a function of the detuning δ . (b) The population P_1 of the state $|1\rangle$ (solid line) and the population P_2 of the state $|2\rangle$ (dotted line) are plotted as a function of the detuning δ [113].

and an electromagnetic field. The Hamiltonian in the rotating-wave approximation reads

$$H = \frac{\hbar}{2} \begin{bmatrix} 0 & \Omega_0(t) \\ \Omega_0(t) & -2\delta(t) \end{bmatrix}. \quad (4.1)$$

Here, $\Omega_0(t)$ is the resonant Rabi frequency and $\delta = \omega - \omega_0$ is the detuning of the frequency of the field ω with respect to the transition frequency ω_0 of the two atomic levels, $|1\rangle$ and $|2\rangle$. The eigenstates of this system are called dressed states and are

$$\begin{aligned} |+\rangle(t) &= \sin[\theta(t)] |1\rangle + \cos[\theta(t)] |2\rangle, \\ |-\rangle(t) &= \cos[\theta(t)] |1\rangle - \sin[\theta(t)] |2\rangle, \end{aligned} \quad (4.2)$$

with the mixing angle $\theta(t)$ which is defined by $\tan[2\theta(t)] = \Omega_0(t)/\delta(t)$. The eigenenergies corresponding to the dressed states $|\pm\rangle$ are $\hbar\omega^\pm = \frac{\delta}{2} \pm \frac{\hbar}{2}\sqrt{\Omega_0(t)^2 + \delta(t)^2}$.

Let us consider for the ARP that the frequency ω of the electromagnetic field is detuned from the resonance frequency ω_0 of the atomic transition. Then, the detuning is slowly scanned through the resonance, $\delta(t) = \alpha \cdot t$ (with α being an arbitrary constant) from very large negative values ($\delta < 0$, $|\delta| \gg \Omega_0$) to very large positive values ($\delta > 0$, $|\delta| \gg \Omega_0$), or vice versa. The Rabi frequency is kept constant, $\Omega_0 = \text{const.} \neq 0$. In Fig. 4.10 (a), the energies of the dressed and bare states are plotted as a function of the detuning. In contrast to the bare states, the coupling prevents the dressed states from crossing at $\delta = 0$. For large positive or negative detunings their energies approach the energies of the bare states. While the detuning is swept, the mixing angle $\theta(t)$ evolves from $\pi/2$ to 0, which changes the composition of the dressed states according to Eqs. (4.2). Thus, starting in state $|1\rangle$, when the change of the detuning is slow enough, the system evolves adiabatically and stays in the dressed eigenstate $|+\rangle$. Eventually, it ends up in $|2\rangle$. In

Fig 4.10 (b), the population of the bare states is plotted as a function of the detuning. It shows that the sweep of the detuning causes a complete transfer of the population from state $|1\rangle$ to $|2\rangle$, or vice versa. In order to adiabatically transfer the atomic population via this method from one state to the other, the change of the detuning must fulfill the adiabaticity criterion [114]:

$$\frac{d}{dt}|\delta| \ll \Omega_0^2. \quad (4.3)$$

Note that the exact shape of the time evolution of the detuning is not crucial for the transfer.

We have successfully implemented the ARP technique in our system: We load the cesium atoms in the two-color dipole trap in the $F = 3$ hyperfine ground state. While applying a homogenous magnetic field of 3 G to selectively address the Zeeman substates, we sweep the frequency of the MW source over the $|F = 3, m_F = -3\rangle \rightarrow |F = 4, m_F = -3\rangle$ π -transition. After this, a transmission spectrum of the $F = 4$ to $F' = 5$ transition is taken in order to determine the transferred population in the previously unoccupied $F = 4$ state. The sweep span is kept constant at 200 kHz. We found from separate measurements that the detuning has to be at least ± 100 kHz in order to transfer all the atoms. The number of transferred atoms is normalized to the maximally achieved transfer via the π -pulse method (Rabi oscillations) on the $|F = 3, m_F = -3\rangle \rightarrow |F = 4, m_F = -3\rangle$ π -transition. In Fig. 4.11, the normalized number of transferred atoms is shown as a function of the sweep time of the frequency for the π -transition and the $|F = 3, m_F = -3\rangle \rightarrow |F = 4, m_F = -4\rangle$ σ^- -transition.

Via ARP, it is possible to transfer the atoms from one specific Zeeman substate to another with a very high efficiency. Even for the σ -transition, where it was found to be almost impossible to transfer the atomic population with a π -pulse [101], we can achieve a high transfer efficiency. Furthermore, we can deduce from this measurement that the optimal sweep time is different for different transitions. It is thus necessary to characterize and to optimize the parameters of the ARP for every transition. Note that the sweep speed of 200 kHz in 0.1 ms shows the most efficient transfer for the $|F = 3, m_F = -3\rangle \rightarrow |F = 4, m_F = -3\rangle$ π -transition and fulfills the adiabaticity criterion stated in Eq. (4.3). A reason why it is almost not possible to transfer atomic population with a MW π pulse on a σ -transition in our system has not been found yet. An explanation could be that the fraction of the MW radiation that is σ -polarized is very small. Thus, the required π -pulses would be very long and not efficient due to the limited coherence time.

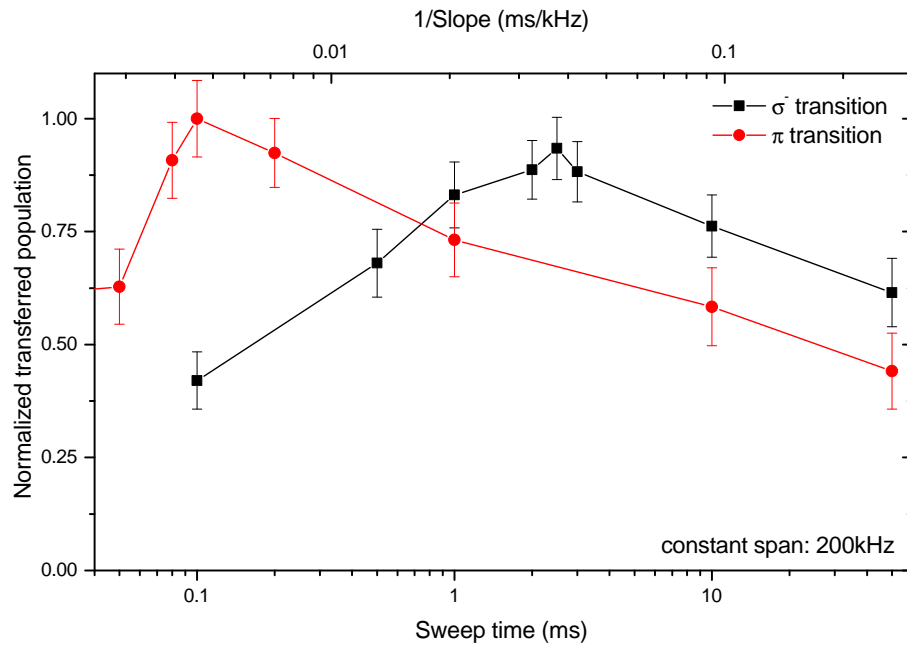


Figure 4.11: Atomic population transferred from the $F = 3$ to the $F = 4$ hyperfine state with adiabatic rapid passage as a function of the time the frequency sweep takes. The frequency span is kept constant at $\Delta = \pm 100$ kHz. The red (black) data points shows the ARP for the $|F = 3, m_F = -3\rangle \rightarrow |F = 4, m_F = -3\rangle$ π -transition ($|F = 3, m_F = -3\rangle \rightarrow |F = 4, m_F = -4\rangle$ σ^- -transition).

Discerning and selectively manipulating nanofiber-trapped atoms

In the previous chapter, we have seen that the trapping sites of the two-color dipole trap form two diametric linear arrays along the optical nanofiber. The trapped atoms are therefore arranged in two spatially separated ensembles that, in general, interact simultaneously with all light fields that propagate through the nanofiber. In this chapter, I will show that the two atomic ensembles can be simultaneously and independently manipulated with fiber-guided light fields. This would not be possible with conventional light fields, but can be realized thanks to the extraordinary polarization pattern of strongly confined nanofiber-guided light. With the techniques I present in this chapter, we gain full control over the azimuthal position of the trapped atoms around the nanofiber. This means, we can selectively address one atomic ensemble on only one side of the fiber to perform experiments with.

In the first part of this chapter, I will explain how to prepare the trapped atoms in a given Zeeman substate using optical pumping schemes involving fiber-guided light. Furthermore, I will show that it is possible to optically prepare one atomic ensemble in one state and, simultaneously, the other ensemble in another state. In the second part, I will study how fictitious magnetic fields can be used to selectively manipulate the two atomic ensembles and to perform state preparation. The majority of the experiments that I present in this chapter are published as an article in Physical Review A [50].

5.1 Introduction

For what follows in this chapter, it is important to introduce an unambiguous nomenclature concerning the spatial arrangement of the two atomic ensembles relative to the nanofiber. In figure 5.1, the nanofiber and the trapped atoms are sketched. All the atoms are trapped in the x - z plane, i.e., $y = 0$. We will refer to the atomic ensemble that is trapped on the positive half-space $x > 0$ as the “right ensemble” or the atoms that are trapped on the “right side” of the nanofiber.

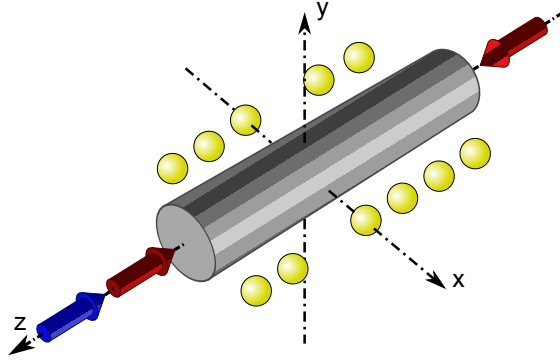


Figure 5.1: Sketch of the optical nanofiber (gray cylinder) and the trapped atoms (yellow spheres). The atoms are trapped in linear arrays forming one ensemble on the “right side” of the fiber ($x > 0$) and one ensemble on the “left side” of the fiber ($x < 0$). The propagation directions of the blue-detuned and red-detuned trapping light fields are indicated by the blue and red arrows, respectively. A homogeneous magnetic offset field can be applied along the y axis.

Following this definition we will refer to other atomic ensemble that is trapped on the negative half-space $x < 0$ as the “left ensemble” or the atoms that are trapped on the “left side” of the nanofiber. Here, we choose the quantization axis along the y axis, i.e., the axis along which an homogenous magnetic field can be applied.

5.2 Optical Pumping

For performing experiments with ensembles of atoms, it is often useful that their internal state is the same. In this case one speaks of a polarized ensemble. The interaction of the atoms with resonant light fields can lead to a change of the internal state of the atom and thus to a redistribution of the atomic population over the hyperfine and Zeeman sublevels. This redistribution is referred to as optical pumping [115, 116].

In our nanofiber-based dipole trap, the trapped atoms are initially optically pumped into one hyperfine ground state, where they are distributed over the Zeeman sublevels. Note that we experimentally observed that the distribution over the Zeeman substates depends on the respective hyperfine manifold: When the atoms are loaded in the $F = 4$ manifold, followed by the application of a homogeneous magnetic field which allows us to spectrally separate the Zeeman substates, the atoms preferentially end up in the negative m_F states. In contrast, they preferentially end up in the positive m_F states when they are loaded in the $F = 3$ manifold [101].

In this section, I will present experiments that demonstrate optical pumping of nanofiber-trapped cesium atoms with fiber-guided light fields. I will show, in the first part, how optical pumping into a first order magnetic field-insensitive Zeeman state is realized. In the second part, optical pumping of the trapped atoms into the outermost Zeeman states is shown. In this context, I will show that the presented scheme allows us to simultaneously optically pump one atomic ensemble into one outermost Zeeman state and the other ensemble into the other outermost state.

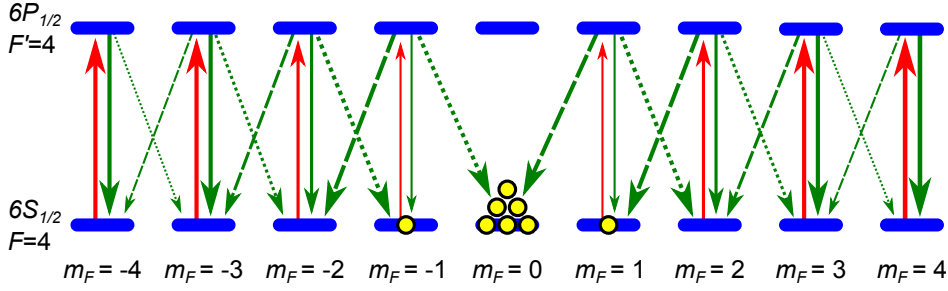


Figure 5.2: Optically pumping the atoms into the $|F = 4, m_F = 0\rangle$ state: The solid, dotted, and dashed arrows represent π , σ^- , and σ^+ transitions, respectively. The relative strength of a transition is roughly indicated by the thickness of the arrow. The red arrows represent the excitation light resonant with the $|F = 4\rangle \rightarrow |F' = 4\rangle$ transition of the D_1 line and the green arrows represent the spontaneous emission process. The yellow spheres indicate the population of atoms that accumulates mostly in $m_F = 0$. Note that the $m_F = 0 \leftrightarrow m_F = 0$ transition is dipole-forbidden.

5.2.1 Optical pumping into $m_F = 0$

A possible way to perform optical pumping is to transfer the atoms into a so-called dark state in which they are decoupled from the excitation light field [93]. To realize optical pumping into the magnetic substate $m_F = 0$ of the $F = 4$ manifold, we employ the fact that the π -transition $|F = 4, m_F = 0\rangle \leftrightarrow |F' = 4, m_F = 0\rangle$ is dipole-forbidden. In figure 5.2, this method is depicted: π -polarized light excites the atoms in all $m_F \neq 0$ states. Since there is a finite probability for the excited atoms to decay towards $m_F = 0$, they will eventually all end up in this state after some scattering processes. For the transition described here, the relative probability to undergo a σ transition towards the $m_F = 0$ state is even higher than towards the outermost $m_F = \pm F$ states. Thus, after only a few scattering processes, most atoms will be prepared in the $m_F = 0$ state [117].

For the implementation of this scheme in our system, we have to consider the following: In chapter 3.3.2 we saw that, for atoms trapped in the nanofiber-based dipole trap, m_F , in general is not a good quantum number for the $6P_{3/2}$ excited state. This is caused by the tensor part of the ac Stark operator that describes the coupling of the atoms with the trapping light fields. However, the $6P_{1/2}$ excited state of the D_1 line has a total angular momentum $J = 1/2$ and since the tensor part of the ac Stark interaction therefore vanishes, m_F is still a good quantum number. For the considered optical pumping process, we need to drive specific transitions between the m_F states and we therefore use a light field that is resonant with the D_1 line. The light with a wavelength of 894 nm is provided by a homemade external cavity diode¹ laser (ECDL). Its frequency is stabilized with a grating and locked on the $|6S_{1/2}, F = 4\rangle \rightarrow |6P_{1/2}, F' = 4\rangle$ hyperfine transition via a polarization spectroscopy. The light field is attenuated by several filters and finally propagates in the nanofiber with a power of ≈ 8 pW. This yields $s = I/I_{\text{sat}} = 0.04$

¹L904P010 by Thorlabs

for the saturation parameter at the trapping minimum.

The optical pumping light field has to be π -polarized at the position of the atoms in order to realize the presented pumping scheme. Therefore, we choose the light field to be quasi-linearly polarized in the nanofiber and set its main direction of polarization along the y axis, which leads to the desired polarization at the position of the atoms at the minimum of the trap (see Fig. 2.6 in chapter 2.2).

Atoms which are excited by the optical pumping light field to the $|6P_{1/2}, F' = 4\rangle$ state have a high probability of 58 % to decay in the $|6S_{1/2}, F = 3\rangle$ ground state. These atoms are lost from the optical pumping process and thus have to be repumped to the $F = 4$ hyperfine ground state. For optically repumping the atoms, we employ the repumper beam that is used for the magneto-optical trap and is shone in simultaneously with the optical pumping light field to pump the atoms into $m_F = 0$. During the whole optical pumping process, an external magnetic field of 3 G is applied along the y axis to prevent the atoms to undergo spin flips.

In order to have a measure for the efficiency of the optical pumping process, we studied Rabi oscillations on the $|F = 4, m_F = 0\rangle \leftrightarrow |F = 3, m_F = 0\rangle$ clock transition: Initially, the atoms are prepared in the $F = 4$ hyperfine manifold. The optical pumping light field is resonant with the Stark shifted $|F = 4\rangle \rightarrow |F' = 4\rangle$ transition and was turned on for 500 μs . The repumper light field illuminated the atoms at the same time and was kept on for additional 2 ms in order to make sure that no atom remains in the $F = 3$ ground state. Then, a MW pulse with a length $t_{\text{MW pulse}}$ that is resonant with the clock transition was applied to transfer the atoms from $|F = 4, m_F = 0\rangle$ to $|F = 3, m_F = 0\rangle$. To remove all the atoms that remained in $F = 4$, an external push-out laser [118] was shone on the atoms for 10 μs . The push-out laser is σ^- -polarized and drives the closed $|F = 4\rangle \rightarrow |F' = 5\rangle$ transition of the D₂ line. It thus resonantly heats and expels the addressed atoms from the trap. At this point, only atoms that have been transferred by the MW pulse from $|F = 4, m_F = 0\rangle$ to $|F = 3, m_F = 0\rangle$ remained trapped. A consecutive repumping laser brought these atoms back to the $F = 4$ state. Then, the $F = 4$ manifold was probed via transmission spectroscopy in order to determine the number of transferred atoms. In Fig. 5.3, the results of this measurement with and without optical pumping is shown. The number of atoms that have been transferred by the MW pulse is plotted as a function of the pulse length. We normalized this number to the total number of atoms in the $F = 4$ manifold after optical pumping. In order to obtain this reference, we performed an additional measurement where we probed the $F = 4$ manifold directly after the optical pumping procedure via transmission spectroscopy.

From the results of the measurement, which are plotted in Fig. 5.3, we can conclude that $43\% \pm 1\%$ of the atomic population in the $F = 4$ manifold is prepared in the $|F = 4, m_F = 0\rangle$ state. This number could be further increased to $67\% \pm 6\%$, by carefully aligning the polarization of the optical pumping light field. For comparison, without optical pumping, only $1.6\% \pm 0.6\%$ of the population in the $F = 4$ manifold is found in $|F = 4, m_F = 0\rangle$. This means that we could increase the number of atoms in $m_F = 0$ by a factor of up to ≈ 40 . As a possible drawback of this method the atoms are presumably heated by the pumping light fields, thereby reducing the coherence times. However, this effect has not been confirmed yet.

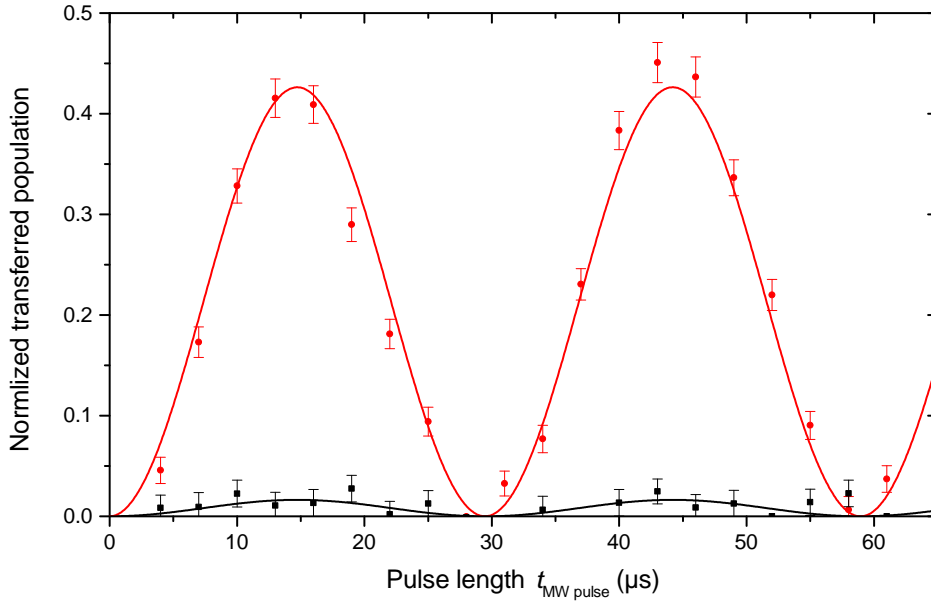


Figure 5.3: Rabi oscillations on the clock transition with (red dots) and without (black squares) a preceding optical pumping procedure towards $m_F = 0$. The solid lines are the result of a global fit $f(t) = A/2(1 - \cos[\pi \cdot t \cdot \Omega_0])$. The fit yields the amplitude $A = 0.426(8)$ ($A = 0.016(6)$) of the red (black) curve and the shared Rabi frequency $\Omega_0 = 33.9(3)$ kHz. Thanks to optical pumping, the number of atoms in $m_F = 0$ could be increased by a factor of 26 ± 3 in this measurement.

Loss of atoms in an external magnetic field

During the optical pumping process, we observed a loss of atoms from the trap that is much higher than what would be expected by taking the lifetime of the atoms in the trap into account. It turned out that the atoms escape from the trap under the following condition: the atoms are optically pumped from one hyperfine ground state to the other ($F = 3 \leftrightarrow F = 4$) with an external or fiber-guided light field while a homogeneous magnetic field is applied. As an example, we recorded the number of atoms after optically pumping them from the $F = 4$ to the $F = 3$ state in the presence of a homogeneous external magnetic field. For this purpose, we initially prepared the atoms in the $F = 4$ manifold. Then, the external magnetic field was applied and the atoms were optically pumped via a 5 ms long pulse to the $F = 3$ manifold. In this case, the optical pumping was performed with the MOT cooler light field, although it is resonant with the $F = 4$ to $F = 5$ transition. After turning the external magnetic field off again, the atoms were transferred back to $F = 4$ where they were probed via transmission spectroscopy. The result of this measurement is shown in Fig. 5.4 where the number of atoms, normalized to the number of atoms measured without applying an external magnetic field, is plotted in dependence of the magnitude of the external magnetic field. The measurement shows a drastic loss of atoms of up to 85 % during the pumping process in the presence of a magnetic field. Furthermore, the measurements reveal that the magnetic field at which the loss of atoms is maximal depends on

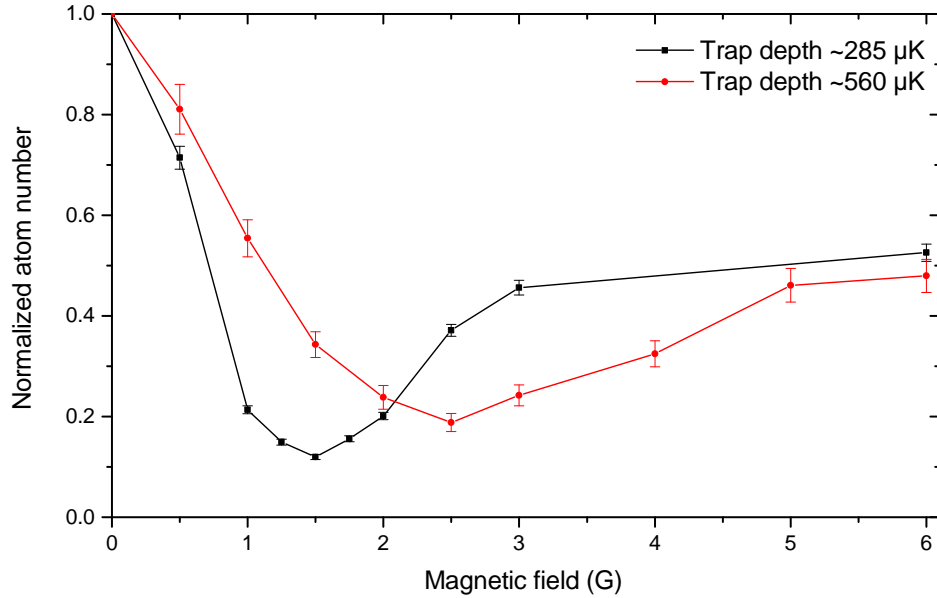


Figure 5.4: Number of atoms that remain in the trap after the atoms are optically pumped from one hyperfine ground state to the other in dependence of the applied external magnetic field. The measurement was performed for a trap depth of $\approx 220 \mu\text{K}$ (black points) and $\approx 560 \mu\text{K}$ (red points). The corresponding powers of the trapping light fields are 13.5 mW (27.2 mW) for the blue-detuned light field and $2 \times 1.35 \text{ mW}$ ($2 \times 2.7 \text{ mW}$) for the red-detuned light field.

the trapping parameters, e.g., the trap depth.

This effect has been observed in other steep dipole traps as well, e.g., in microtraps [119]. However, the cause of this effect is still under investigation. In [88], it is described in detail that in our trap the minima of the trapping potentials of the $m_F \neq 0$ Zeeman sublevels of the hyperfine ground states are spatially shifted in the azimuthal direction due to the fictitious magnetic field induced by the blue-detuned trapping light field. In fact, due to the opposite sign of the Landé factors, the minima of the $|F = 4, m_F\rangle$ potentials are shifted in the opposite direction than the minima of the $|F = 3, m_F\rangle$ potentials. Therefore, an atom that is at the trapping minimum in a given m_F state in $F = 4$ and that undergoes a transition to $F = 3$ might end up in a higher vibrational level when the quantum number of the m_F sublevel does not change. However, this effect should vanish for high magnetic fields.

5.2.2 Optical pumping into the outermost Zeeman states

In order to prepare the trapped atoms in an outermost Zeeman substate $m_F = \pm F$ of a given F -manifold, we can optically pump them with σ^\pm -polarized light driving $m_{F'} - m_F = \pm 1$ transitions towards a F' state with $F' = F + 1$. In this situation, the optical pumping process does not rely on pumping the atoms into a dark state, but rather on driving a cycling transition where the atom always decays to the state it has been excited from [117]. This method is depicted

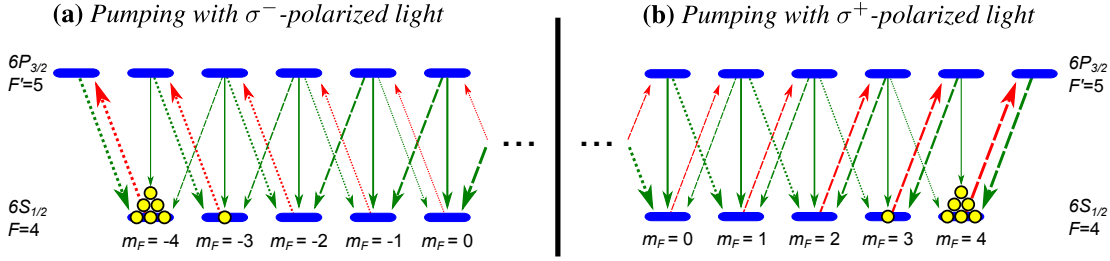


Figure 5.5: Optical pumping with (a) σ^- -polarized light and (b) σ^+ -polarized light. The solid, dotted, and dashed arrows represent π , σ^- , and σ^+ transitions, respectively. The relative strength of a transition is roughly indicated by the thickness of the arrow. The red arrows represent the excitation light resonant with the D_2 line and the green arrows represent the spontaneous emission process. The yellow spheres indicate the population of atoms that accumulate mostly in (a) $m_F = -4$ or (b) $m_F = +4$.

in Fig. 5.5 (a) and (b) for a σ^- -polarized and a σ^+ -polarized pumping light field, respectively.

With an external σ^\pm -polarized light field, all the atoms trapped along the fiber can be pumped in the $m_F = \pm F$ state. Nevertheless, a fiber-guided field opens interesting possibilities: The evanescent field of a quasi-linearly polarized nanofiber-guided light field with its main direction of polarization along the x axis is almost fully σ^+ -polarized on one side of the fiber and almost fully σ^- -polarized on the opposite side (see section 2.2). Taking advantage of this property, one and the same light field allows us to simultaneously optically pump the two atomic ensembles in two different outermost m_F states, respectively.

To demonstrate this, the atoms are prepared in the $F = 4$ manifold where they are initially distributed over all m_F states. In order to physically define the required quantization axis, we apply a magnetic offset field along the y axis. We set $B_{\text{off}} = 28$ G in order to clearly optically separate the two outermost transitions. This allows us to quantify the efficiency of the optical pumping process via transmission spectroscopy. We apply this comparatively large magnetic field already for the optical pumping sequence, although the latter could be performed in much lower magnetic fields. However, changing B_{off} takes several milliseconds and we want to avoid this delay since it would lead to a loss of signal due to the finite lifetime of the atoms.

For the optical pumping process, we launch a quasi-linearly polarized pump light field into the nanofiber that is resonant with the ac Stark shifted $F = 4 \rightarrow F' = 5$ transition of the D_2 line. To provide the desired polarization at the position of the atoms, its main direction of polarization is along the x axis, i.e., in the plane containing the atoms. In order to address all the Zeeman substates, the frequency of the pump light field is scanned in 1 ms over 135 MHz. A transmission spectrum of a subsequent probe pulse is recorded by sweeping its frequency continuously in 5 ms over 135 MHz.

The recorded number of transmitted photons is plotted in Fig. 5.6, see red dots. It is normalized to the number of transmitted photons of a reference probe pulse that is recorded without trapped atoms. The power of the pumping and probing light fields is 4 pW to minimize the heating and the resulting loss of the atoms. In the spectrum, two resonances can be identified as dips

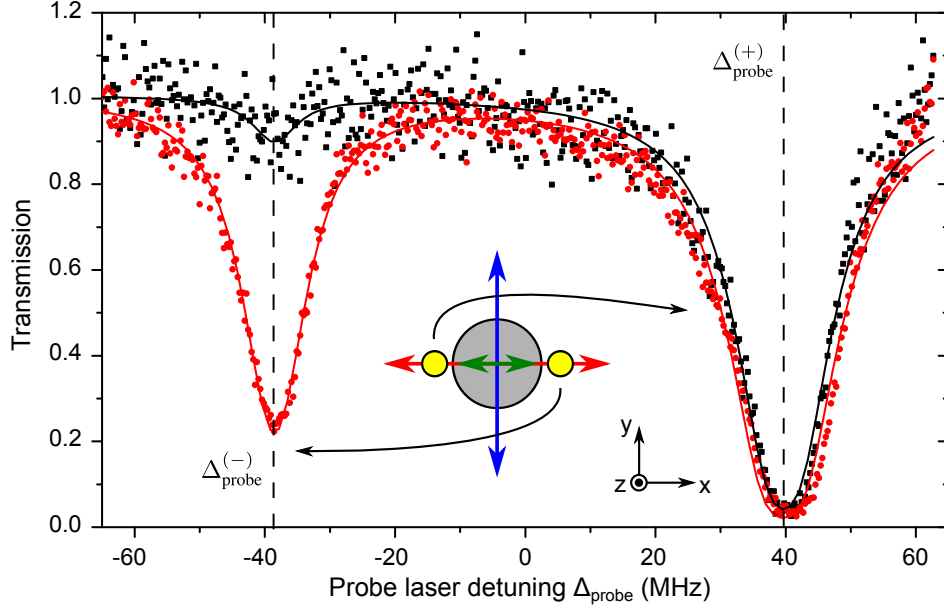


Figure 5.6: Transmission spectrum of the probe light field recorded in a magnetic field of $B_{\text{off}} = 28$ G. The two transmission dips at $\Delta_{\text{probe}}^{(\pm)}$ stem from the two atomic ensembles trapped on the left side ($x < 0$) and on the right ($x > 0$) of the nanofiber, as indicated by the yellow disks. The black (red) data points are recorded with (without) applying the push-out laser to remove the atomic ensemble at $x > 0$ from the trap. The solid lines are fits to the measured data points. The red, blue, and green double arrows in the sketch indicate the main direction of polarization of the red-detuned, the blue-detuned, and pumping/probing light field, respectively.

in the transmission. This transmission spectrum is fitted with the following function

$$T(\Delta_{\text{probe}}) = \exp \left[- \sum_{k=+,-} \frac{\text{OD}_k}{1 + \frac{4(\Delta_{\text{probe}} - \Delta_{\text{probe}}^{(k)})^2}{\Gamma^2}} \right]. \quad (5.1)$$

The exponent takes two Lorentzian line profiles into account that correspond to two atomic resonances at a probe field detuning $\Delta_{\text{probe}}^{(\pm)}$. The two Lorentzians have a common linewidth Γ and individual optical densities OD_{\pm} . From the fit, we find the two resonances to be at $\Delta_{\text{probe}}^{-} = -38.55(7)$ MHz and $\Delta_{\text{probe}}^{+} = 39.82(8)$ MHz with a linewidth of $\Gamma = 8.3(2)$ MHz and an optical density of $\text{OD}_{-} = 1.55(6)$ and $\text{OD}_{+} = 4.6(3)$, respectively.

The linewidth is slightly larger than the natural linewidth of cesium $\Gamma_{\text{nat}} = 5.2$ MHz. This deviation can be explained by taking into account that the transition is inhomogeneously broadened due to the light shifts induced by the trapping light fields. Assuming the temperature of the atoms to be $T = 50$ μK , which is in reasonable agreement with previous measurements [39], we calculate the radial probability distribution of the position of the atom in the trap (in the

		ramp up B-field	optical pumping	pushout	optical pumping	wait	probing
Time		25 ms	1 ms	5 ms	1 ms	2 ms	5 ms
Magnetic field	28 G 0 G						
Pump/Probe light field	ON OFF						
Pump/Probe frequency	67 MHz -67 MHz						
Repump light field	ON OFF						
Pushout light field	ON OFF						

Figure 5.7: Experimental sequence to optically pump the two atomic ensembles into the $|F = 4, m_F = \pm 4\rangle$ states, respectively. The dashed line in the row of the push-out light field shows that the push-out light field is turned on at the indicated instance if one atomic ensemble is to be removed from the trap.

$|F = 4, m_F = \pm 4\rangle$ state). We then calculate the linewidth of the inhomogeneously broadened transition and find $\Gamma_{T=50 \mu\text{K}} = 8.01(6)$ MHz. This value matches well with the fitted linewidth.

The difference of the fitted frequencies of the two resonances $\Delta_{\text{probe}}^{(+)} - \Delta_{\text{probe}}^{(-)} = 78.4(1)$ MHz perfectly agrees with the splitting between the two outermost σ^+ and σ^- transitions of the $F = 4 \rightarrow F' = 5$ transition of 78.4 MHz for $B_{\text{off}} = 28$ G [120]. This endorses our interpretation that the atomic ensembles indeed have been transferred by the pumping light field to the outermost $|F = 4, m_F = -4\rangle$ and $|F = 4, m_F = +4\rangle$ states. Here, the optical pumping light field was propagating in the $-z$ direction. Thus, the optical pumping light field was σ^+ - (σ^- -) polarized on the left (right) side of the nanofiber. Therefore, the atomic ensemble trapped on the left (right) side has been transferred to the $|F = 4, m_F = +4\rangle$ ($|F = 4, m_F = -4\rangle$) state.

Furthermore, the fit yields the ODs for the two atomic ensembles. Thus, recording a transmission spectrum in the way that it is presented here, enables us to determine the two optical densities of the two atomic ensembles in one experimental run. The experimental sequence used for the optical pumping process is summarized in Fig. 5.7.

This side-dependent state preparation allows us to selectively address and manipulate the two atomic ensembles independently. We can, for example, expel only one ensemble from the trap. To do so, we illuminate the atoms after the optical pumping pulse for 5 ms with a push-out light field. The frequency of this light field is resonant with the Zeeman-shifted $|F = 4, m_F = -4\rangle \rightarrow |F = 5, m_F = -5\rangle$ cycling transition. It resonantly heats and expels the addressed atoms from the trap. Since the push-out light field might also redistribute the Zeeman-state populations of the atoms we subsequently perform another pumping pulse to ensure that the atoms are in the outermost Zeeman substates. The black data points in Fig. 5.6 correspond to the subsequently recored transmission spectrum. The resulting spectrum now shows the transmission dip at $\Delta_{\text{probe}}^{(+)}$ only, which is almost unaffected by the push-out light field ($\text{OD}_+ = 3.5(2)$).

The transmission dip at $\Delta_{\text{probe}}^{(-)}$ is essentially not visible anymore ($\text{OD}_- = 0.11(1)$). Thus, the atomic ensemble on the right side of the fiber (at $x > 0$) has been almost completely removed from the trap [50]. The fact that the atoms on the left side of the fiber have also been slightly affected by the push-out light field can be attributed to off-resonant excitation and a resulting loss of atoms.

Changed propagation direction of the optical pumping light field

From the data presented in Fig. 5.6, we conclude that the optical density of the atomic ensemble trapped on the left side of the fiber is higher than the OD of the other atomic ensemble, i.e., $\text{OD}_- < \text{OD}_+$. When the propagation direction of the optical pumping light field is changed to the $+z$ direction, the atomic ensemble on the left (right) of the nanofiber is subject to σ^- (σ^+) polarized light. Therefore, by performing the same optical pumping experiment, we expect $\text{OD}_- > \text{OD}_+$ since the atomic ensemble with the higher optical density will now be pumped to the $|F = 4, m_F = -4\rangle$ state. The results of this measurement presented in Fig. 5.8 (blue data points) confirm this prediction. Here, it can be observed that the optical densities of both ensembles for a pumping light field propagating in the $+z$ direction (see blue data points) are smaller than the optical densities obtained from the transmission spectrum where the pumping light field propagated in the $-z$ direction (red data points). Since for both measurements the atoms were prepared in the same way, a possible explanation is that the alignment of the polarization for the probing light field propagating in the $+z$ direction was imperfect. Thus, the light field coupled less to the atoms and the optical density was reduced.

In conjunction with the atomic conveyor-belt presented in [42] the presented techniques give full control over the axial and the azimuthal position of the atoms around the nanofiber. For the experiments I will describe in the next chapter (Ch. 6), the capacity to prepare just one atomic ensemble is essential. Furthermore, it can be very advantageous if one wants to couple nanofiber-trapped atoms with other quantum devices like SQUIDS² [47]. For coupling nanofiber-trapped atoms to whispering gallery resonators like a bottle resonator [121, 122] for performing cavity quantum electro-dynamics experiments [123] the presented technique is useful as well.

5.3 Selective addressing of atoms prepared in the same substate

In this section, I show that it is possible to discern and to selectively address the two atomic ensembles even when they are in the same Zeeman substate. I will first demonstrate the method on the least magnetic field-sensitive state, namely $m_F = 0$. This makes it possible to work with both ensembles in the state with the longest coherence time of our trap [43], while it is still possible to selectively manipulate them. For this purpose, we will make use of light-induced fictitious magnetic fields that arise in our system, see chapter 3.4. We will first investigate the effect of the fictitious magnetic field that is induced by fiber-guided light fields on the $|F = 3, m_F = 0\rangle \leftrightarrow |F = 4, m_F = 0\rangle$ clock transition. In the subsequent section, I will then present two methods that allow us to discern and to selectively manipulate the two atomic ensembles even when they are prepared in the same Zeeman substate [50].

²superconducting quantum interference device

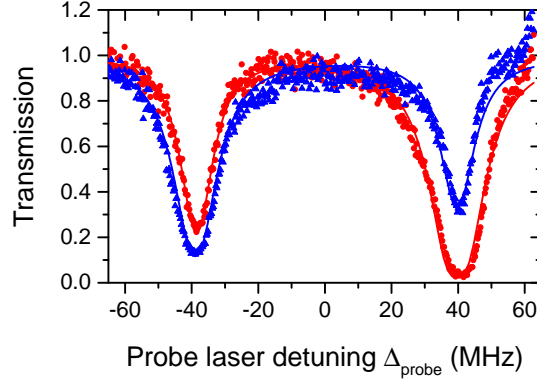


Figure 5.8: Transmission spectrum of the optically pumped ensemble. The optical pumping was performed with the pumping light field propagating in the $-z$ direction (red data points) and in the $+z$ direction (blue data points).

5.3.1 Lifting the degeneracy between the two atomic ensembles

An off-resonant nanofiber-guided light field can induce fictitious magnetic fields on the trapped atoms, as discussed in chapter 3.4. For a quasi-linearly polarized light field, the fictitious magnetic field at the position of the atoms is maximized when the main direction of polarization of the light field is oriented along the x axis (in the plane containing the atoms). The two atomic ensembles are then subject to opposite fictitious magnetic fields, since \mathbf{B}_{fict} has opposite signs on opposite sides of the fiber, see Fig. 5.9 (a). The linear Zeeman effect thus leads to the desired degeneracy for first-order magnetic-field-sensitive transitions.

For transitions that only exhibit a quadratic dependency on the magnetic field, like the $|F = 3, m_F = 0\rangle \rightarrow |F = 4, m_F = 0\rangle$ clock transition, the induced fictitious magnetic fields cannot lift the degeneracy of this transition frequency for the two atomic ensembles. However, an external homogeneous magnetic offset field \mathbf{B}_{off} additionally applied along the $+y$ direction, leads to the desired lift of degeneracy. As depicted in Fig. 5.9 (b), the atomic ensemble trapped on the left side of the fiber experiences a different magnitude of the total magnetic field than the ensemble on the right side. In our experiments, where $|\mathbf{B}_{\text{off}}| > |\mathbf{B}_{\text{fict}}|$, one atomic ensemble experience a total magnetic field of $|\mathbf{B}_{\text{tot}}| = |\mathbf{B}_{\text{off}} + \mathbf{B}_{\text{fict}}| = B_{\text{off}} + B_{\text{fic}}$ and the other atomic ensemble of $|\mathbf{B}_{\text{tot}}| = B_{\text{off}} - B_{\text{fic}}$.

A nanofiber-guided light field that induces the desired fictitious magnetic fields, in general, also induces scalar light shifts. For the nanofiber-based dipole trap, these unwanted scalar shifts would lead to a significant distortion of the trapping potential due to the strong radial intensity gradient of the nanofiber-guided fields [124]. A possibility to circumvent this problem lies in the proper choice of the wavelength of the light field that induces the fictitious magnetic field. As discussed in chapter 3.2.1, at a tune-out wavelength [85], the scalar part of the atomic polarizability vanishes whereas the nonzero vector part leads to the desired fictitious magnetic field. For Cs atoms $\lambda_0 = 880.2524$ nm is a tune-out wavelength [76]. Another way to induce fictitious magnetic fields can be realized by employing the trapping light fields. For the standard

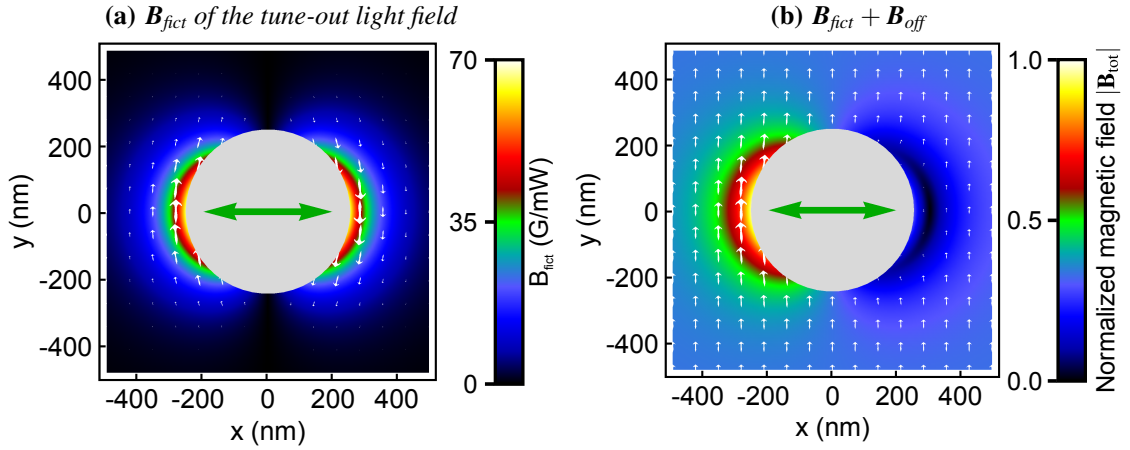


Figure 5.9: (a) Fictitious magnetic field of the quasi-linearly polarized tune-out light field around the nanofiber. At the position of the atoms ($x = \pm 480$ nm and $y = 0$ nm) its magnitude is $|\mathbf{B}_{\text{fict}}| = 5.37$ G/mW. (b) Resulting total magnetic field when the fictitious magnetic field of the tune-out light field is superposed with an additional homogeneous magnetic offset field applied along the y axis. At the position of the atoms ($x = \pm 480$ nm and $y = 0$ nm) the magnitude of the total magnetic field is different. For this plot $|\mathbf{B}_{\text{off}}|$ is chosen to be bigger than $|\mathbf{B}_{\text{fict}}|$ at the position of the atoms. Additionally, the total magnetic field $|\mathbf{B}_{\text{tot}}|$ is normalized to its maximal value.

trapping configuration (see chapter 4) the trapping light fields are perfectly linearly polarized at the position of the atoms and thus do not induce fictitious magnetic fields. However, a slight modification of the imbalance of the power of the two counter-propagating red-detuned light fields, or a tilt of the main direction of polarization of the blue-detuned light field results in $B_{\text{fict}} \neq 0$ at the position of the atoms. At the same time, these small deviations from the standard configuration do not significantly modify the scalar shift and, thus, leave the trapping potential essentially unchanged.

5.3.2 Levelshifts due to fictitious magnetic fields

Here, we study the effect of fictitious magnetic fields induced by a laser at the tune-out wavelength $\lambda_0 = 880.2524$ nm on the clock transition. The light field is provided by a frequency stabilized titanium:sapphire laser³ (Ti:Sa). It is coupled in the tapered optical fiber on the same beam paths as the probing light field at 852 nm (see chapter 4.2.3). The light field is quasi-linearly polarized in the nanofiber with its main direction of polarization along x axis, i.e., in the plane containing the atoms. Therefore, its ellipticity and thus the induced fictitious magnetic field is maximal at the position of the atoms, see chapter 3.4.

In order to measure changes in the transitions frequency of the clock transition, we performed MW spectroscopy. To this end, the atoms are prepared in the $F = 3$ hyperfine ground

³Matisse-TX Light by Sirah Lasertechnik GmbH

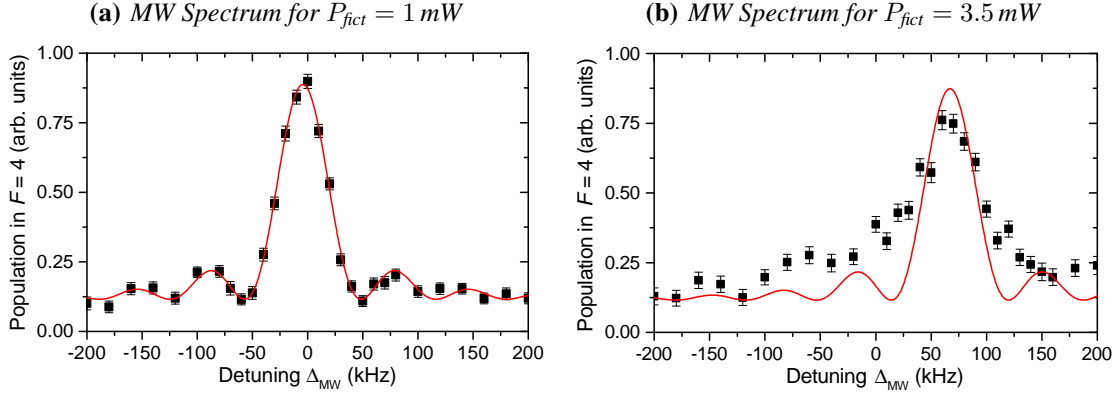


Figure 5.10: MW spectrum of the $|F = 3, m_F = 0\rangle \leftrightarrow |F = 4, m_F = 0\rangle$ transition: the number of transferred atoms is plotted as a function of the detuning Δ_{MW} of the MW pulse. The detuning is taken relative to the clock transition frequency in free space. The solid line is a fit with Eq. (5.2) yielding the detuning at resonance of **(a)** $\Delta_{\text{MW, res}} = -4.3 \pm 0.4$ kHz for $P_{\text{fict}} = 1$ mW and **(b)** $\Delta_{\text{MW, res}} = 67 \pm 3$ kHz for $P_{\text{fict}} = 3.5$ mW. Furthermore, the fit returns the resonant Rabi frequency $\Omega_0/(2\pi) = (33 \pm 1)$ kHz.

state. Then, the light field at the tune-out wavelength is launched with a certain power P_{fict} into the TOF, creating a magnetic field as shown in Fig. 5.9 (a). It has the same magnitude $|B_{\text{fict}}|$ for both atomic ensembles on the two sides of the fiber. In this situation, both sides are degenerate and the frequency of the transition is unequivocally defined. We can spectrally resolve the clock transition by applying a MW π -pulse of a duration of $T = 14.7 \mu\text{s}$. The π -pulse transfers the atoms to the $F = 4$ manifold where the number of atoms is subsequently measured via transmission spectroscopy. In Fig. 5.10 (a), the number of transferred atoms is plotted as a function of the frequency of the MW radiation. With this measurement we can determine the MW resonance frequency of the clock transition with respect to the resonance in free space. We fit the data with the following function that describes the evolution of the population $P_{F=4}(\Delta_{\text{MW}})$ due to the MW radiation [125]

$$P_{F=4}(\Delta_{\text{MW}}) = A \cdot \frac{\Omega_0^2}{\Omega^2} \cdot \sin^2\left(\frac{\Omega \cdot T}{2}\right) + y_0, \quad \text{with } \Omega^2 = (\Delta_{\text{MW}} - \delta)^2 + \Omega_0^2 \quad (5.2)$$

where Ω_0 is the resonant Rabi frequency, T is the duration of the MW pulse, A the amplitude, and y_0 an offset. Here, Δ_{MW} is the detuning of the frequency of the MW radiation with respect to the transition frequency of the clock transition in free space. This fit yields the shifted transition frequency δ of the clock transition relative to its value in free space. Furthermore, the fit shows that the data can be well described by a Fourier-limited line shape. For this measurement, no external magnetic field was applied.

In Fig. 5.11, we plot the resonance frequency of the clock transition as a function of the power P_{fict} of the tune-out light field. A quadratic dependency of the transition on the power is clearly observed. The fit of a quadratic function yields a quadratic dependency of the resonance frequency of $10.2(5)$ kHz/mW². This behavior is expected since $P_{\text{fict}} \propto B_{\text{fict}}$ and the

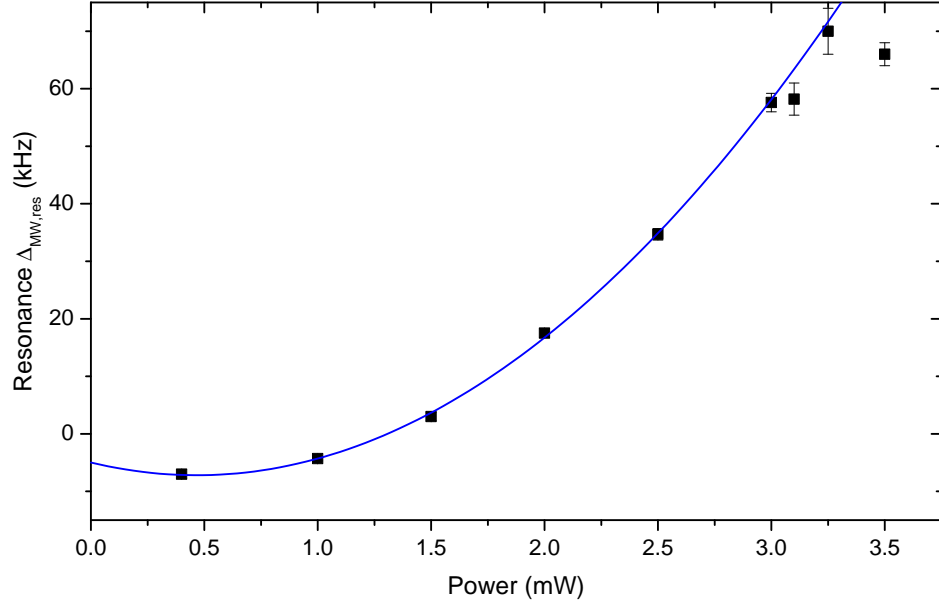


Figure 5.11: Resonance frequency $\Delta_{\text{MW,res}}$ of the clock transition as a function of the power of the tune-out light field. The blue line is a quadratic fit that yields a quadratic shift of the transition of 10.2 kHz/mW^2 and a differential scalar shift of -9.5 kHz/mW .

shift of the clock transition quadratically depends on the magnetic field $\delta = \alpha_0 \cdot B_{\text{fict}}^2$ with the constant $\alpha_0 = 0.427 \text{ kHz/G}^2$ [120]. Thus, we can calculate a light-induced magnetic field of $4.9(1) \text{ G/mW}$ at the position of the trapped atoms. It is in reasonable agreement with the expected 5.35 G/mW obtained by calculating the energy difference between the trapping minima of the $|F = 3, m_F = 0\rangle$ and $|F = 4, m_F = 0\rangle$ states for different values of P_{fict} . For this calculation, the scalar and vector shifts induced by the trapping and tune-out lasers were taken into account. The small discrepancy between the measured and the calculated value can be explained by taking into account that the polarization of the tune-out light field might be not perfectly quasi-linearly polarized. Furthermore, the energy of atoms is not equal to that of the trapping minimum since the atoms are in a low motional state [39]. The fit reveals furthermore a differential scalar shift of $(-9.5 \pm 1.6) \text{ kHz/mW}$ indicated by the finite slope at $P_{\text{fict}} = 0$. This is due to the hyperfine splitting $\Delta\nu_{\text{hfs}} \approx 9.2 \text{ GHz}$ of the $F = 3$ and $F = 4$ manifolds. The tune-out condition cannot be fulfilled for both states. The measured differential scalar shift corresponds to the scalar shift induced by a light field $\Delta\nu_{\text{hfs}}$ away from the tune-out frequency. The three data points obtained for $P_{\text{fict}} > 3 \text{ mW}$ plotted in Fig. 5.11 where not taken into account for the fit. For these powers the induced fictitious magnetic field distorts the trapping potential in a way that leads to a significant broadening of the transition, see Fig. 5.10 (b). I will comment on this fact in chapter 5.3.5.

The usage of fictitious magnetic fields compared to real magnetic fields has the advantage that these fields can be varied as quickly as one can modulate the optical power of the tune-out light field. This means even very high magnetic fields on the order of tens of Gauss can be turned

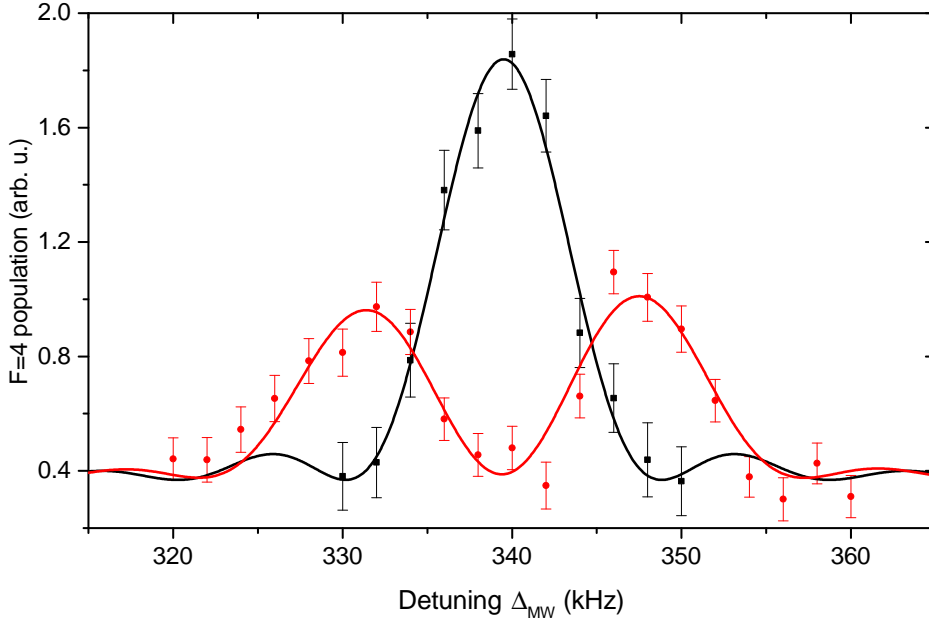


Figure 5.12: MW spectrum of the $|F = 3, m_F = 0\rangle \rightarrow |F = 4, m_F = 0\rangle$ transition with (with-out) applying the light field at the tune-out wavelength shown by the red (black) data points. The number of transferred atoms is plotted as a function of the frequency detuning Δ_{MW} of the MW pulse. The solid lines are a fits yielding the shift of the resonances.

on and off on a timescale much smaller than $1 \mu\text{s}$.

5.3.3 Discerning atoms prepared in $m_F = 0$

As we have seen in the previous section, the fictitious magnetic field induced by the light field at the tune-out wavelength leads to the same frequency shift for both atomic ensembles on the two sides of the nanofiber. In order to lift the degeneracy of the transition frequency of the clock transition for the two atomic ensembles, we now apply an external homogeneous magnetic offset field B_{off} along the $+y$ direction in addition to the fictitious magnetic field, see Fig 5.9 (b).

To demonstrate the lift of degeneracy for the two ensembles on this transition, the following experimental steps were conducted: The Cs atoms are loaded in the $F = 3$ hyperfine manifold. After applying the magnetic offset field of $B_{\text{off}} = 28 \text{ G}$, a $103\text{-}\mu\text{s}$ long MW- π pulse is applied to transfer the atoms that are initially in $|F = 3, m_F = 0\rangle$ to $|F = 4, m_F = 0\rangle$. Note that the power of the MW is lower, compared to the measurements presented in the previous section [see Fig. 5.10 (a)], in order to use longer π -pulses to obtain a higher spectral resolution of $\approx 10 \text{ kHz}$. Here, the resonant Rabi frequency is $\Omega_0/(2\pi) \approx 2.7 \text{ kHz}$. The population of the initially empty $F = 4$ manifold is then measured via transmission spectroscopy. In Fig 5.12, the transferred population as a function of the MW detuning Δ_{MW} is plotted (black data points) when $B_{\text{fict}} = 0 \text{ G}$ [50]. The MW spectrum is fitted as described in the previous section (see Eq. (5.2)). One single Fourier limited peak can be observed, showing that in this situation the

two atomic ensembles contribute equally to the signal and are not discernible. The shift of the resonance frequency of $\Delta_{\text{MW, res}} = 339.5(3)$ kHz with respect to the free space detuning is in reasonable agreement with what is expected from the quadratic Zeeman shift of the clock transition $\Delta_{\text{MW, theo}} = (340 \pm 7)$ kHz [120]. For this calculation, we took into account that the experimentally found value for the maximal magnetic offset field is actually $B_{\text{off}} = (28.2 \pm 0.3)$ G [101].

In order to discern the two atomic ensembles, we change the described experimental sequence: before we apply the MW- π pulse, we turn on the light field at the tune-out wavelength with a power of $P_{880} = 100 \mu\text{W}$. The resulting MW spectrum is shown by the red data points in Fig 5.12. The spectrum clearly shows two Fourier limited peaks with a resonance frequency of $\Delta_{\text{MW}}^{(+)} = 347.7(4)$ kHz and $\Delta_{\text{MW}}^{(-)} = 331.1(4)$ kHz, which we identify as the contributions of the two atomic ensembles on both sides of the fiber [50].

Here, we work in the regime $B_{\text{off}} \gg B_{\text{fict}}$, where the shift of the clock transition is given by $\alpha_0(\mathbf{B}_{\text{off}} + \mathbf{B}_{\text{fict}})^2 \approx \alpha_0(B_{\text{off}}^2 \pm 2\mathbf{B}_{\text{off}} \cdot \mathbf{B}_{\text{fict}})$. So the difference of the two transition frequencies is $\Delta_{\text{MW}}^{(+)} - \Delta_{\text{MW}}^{(-)} = 16.6(6)$ kHz = $4|\mathbf{B}_{\text{off}}| \cdot |\mathbf{B}_{\text{fict}}|$. Thus, with large offset fields we can proportionally enhance the splitting. We experimentally observe the expected behavior that the transitions split symmetrically around the resonance obtained without fictitious magnetic field. From the measured splitting in conjunction with the applied offset field, we can deduce the fictitious magnetic field at the position of the atoms to be $B_{\text{fict}} = 0.35$ G. From the calculations that were performed to explain the results of the measurement presented in Fig. 5.11 we would expect $B_{\text{fict}} = 0.535$ G for $P_{880} = 100 \mu\text{W}$. This deviation can be explained by slightly different trapping parameters in conjunction with an uncertainty in P_{880} . For example, if the power of the blue-detuned trapping light field is higher by 6% (i.e. $P_{\text{blue}} \approx 9$ mW) the position of the atoms will be significantly further away from the surface of the fiber ($r \approx 250$ nm) than with $P_{\text{blue}} = 8.5$ mW ($r \approx 230$ nm). In combination with a power $P_{880} \approx 80 \mu\text{W}$ this already leads to a reduced splitting of ≈ 17 kHz.

5.3.4 Selectively addressing magnetic field-sensitive states

In order to induce fictitious magnetic fields at the position of the atoms, we will now study the scheme that solely relies on tilting the main direction of polarization of the blue-detuned trapping light field. We will analyze the effect on the $|F = 3, m_F = -3\rangle \rightarrow |F = 4, m_F = -3\rangle$ transition. Let us introduce the tilt angle $\varphi_B \equiv \pi/2 - \phi_0$ for the main direction of polarization for the blue-detuned light field. Usually, in our setup its main direction of polarization is along the y axis ($\varphi_B = 0^\circ$) and it is therefore purely linearly polarized at the position of the atoms, see chapter 2.2 and 3.3. For $\varphi_B \neq 0^\circ$, the field at the position of the atoms becomes elliptically polarized and thus induces a fictitious magnetic field. In Fig. 5.13, the two spatial components of \mathbf{B}_{fict} pointing in x and y directions are shown in dependence of φ_B . For $\varphi_B < 10^\circ$, we can observe a small y -component and a larger x -component. The latter can be neglected for application of an offset field along the y direction with $B_{\text{off}} \gg B_{\text{fict}, x}$. The y -component of B_{fict} points in opposite directions for the two atomic ensembles. As discussed in the case of the tune-out light field, this leads, in conjunction with the offset field, to a side-dependent total magnetic field ($B_{\text{tot}} = B_{\text{off}} \pm B_{\text{fict}, y}$). Therefore, the Zeeman substate $|F = 3, m_F = -3\rangle$ is

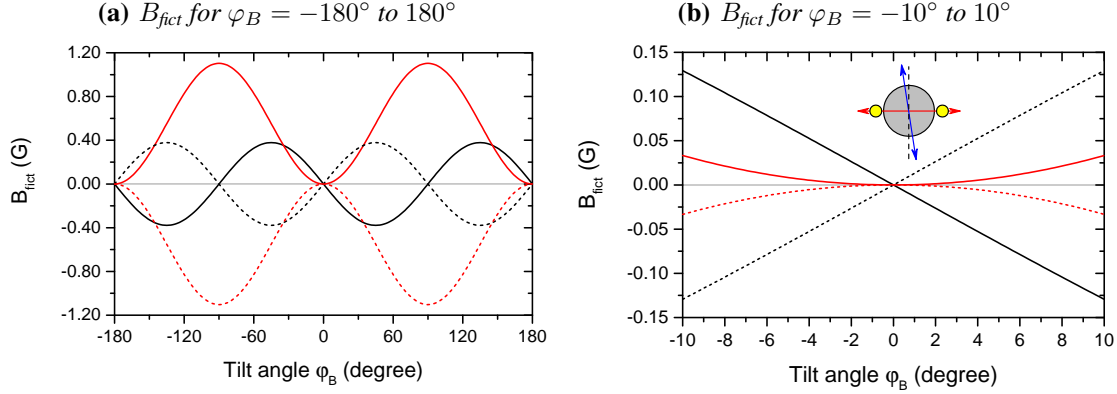


Figure 5.13: (a) Fictitious magnetic field induced by the blue-detuned trapping light field depending on the tilt angle of its main direction of polarization. \mathbf{B}_{fict} is calculated for the typical trapping power of 8.5 mW. The black (red) curves are the x (y) component of \mathbf{B}_{fict} . The solid (dashed) lines represent \mathbf{B}_{fict} at $x = 480$ nm and $y = 0$ nm ($x = -480$ nm and $y = 0$ nm), i.e., at the position of the atoms on the right (left) side of the nanofiber. (b) Expanded view of (a) for small tilt angles φ_B . The inset illustrates the fiber, the atoms (yellow spheres), and main direction of the polarization of the blue- and the red-detuned light field for a tilt angle $\varphi_B \neq 0^\circ$.

	$\varphi_B = 0^\circ$	$\varphi_B = 10^\circ$
ν_{axial}	186 kHz	183 kHz
ν_{radial}	119 kHz	118 kHz
$\nu_{\text{azimuthal}}$	85 kHz	81 kHz
radial trap position	234 nm	238 nm
azimuthal trap position	0°	6.9°

Table 5.1: Parameters of the trapping potential for different tilt angles φ_B of the main direction of the polarization of the blue-detuned trapping light field, with $P_{\text{blue}} = 8.5$ mW and $P_{\text{red}} = 2 \times 0.77$ mW. The radial position of the minimum of the trapping potential is given from the fiber surface. The change of the azimuthal position of the trapping minimum is given relative to the azimuthal position of the unperturbed trap.

shifted differently for the two atomic ensembles. Furthermore, for small tilt angles ($\varphi_B < 10^\circ$) the trapping potential is virtually not changed, see the trapping parameters in Tab. 5.1.

We will combine the side-dependent optical pumping technique presented in chapter 5.2.2 and MW spectroscopy to demonstrate that we can address the atoms of only one atomic ensemble that are in $|F = 3, m_F = -3\rangle$ with MW radiation. For the experiment, we load the atoms in the dipole trap in the $F = 3$ hyperfine ground state. A magnetic offset field $B_{\text{off}} = 3$ G separates neighboring hyperfine transitions by ≈ 1 MHz making them easily resolvable with MW radiation. The atoms that are initially in the $|F = 3, m_F = -3\rangle$ state are transferred with a 40 μs -long π -pulse to the $|F = 4, m_F = -3\rangle$ state. Then, B_{off} is increased to 28 G to perform

the optical pumping sequence explained in section 5.2.2: the transferred atoms that are trapped on the right side of the fiber ($x > a$) are optically pumped to $|F = 4, m_F = -4\rangle$, whereas the transferred atoms that are trapped on the left side of the fiber ($x < a$) are pumped to the $|F = 4, m_F = +4\rangle$. The sequence is concluded by measuring a transmission spectrum of the probing laser as in section 5.2.2. From this transmission spectrum, we can determine the optical densities (OD_{\pm}) of the atomic ensemble trapped on the left and on the right side of the fiber simultaneously, as shown in Fig. 5.6. The ODs we obtain here are proportional to the number of atoms of the two atomic ensembles that have been transferred via the MW pulse at a given MW detuning. We record the ODs for different values of the MW detuning Δ_{MW} and plot them in Fig. 5.14 (a). The OD of the atoms trapped on the right side of the fiber (corresponding to the optical resonance of $\Delta_{\text{probe}}^{(-)}$) is plotted as red data points. The OD of the atoms trapped on the left side of the fiber (corresponding to the optical resonance of $\Delta_{\text{probe}}^{(+)}$) is plotted as black data points. The data points are fitted with the Fourier limited pulse shape [see Eq. (5.2)] to obtain the resonance frequencies for the two atomic ensembles. We will refer with $\Delta_{\text{MW}}^{(-)}$ ($\Delta_{\text{MW}}^{(+)}$) to the resonance for the atomic ensemble on the right (left) side of the nanofiber.

For $\varphi_B = 0^\circ$ [Fig. 5.14 (a)], the MW resonances are $\Delta_{\text{MW}}^{(+)} = -6.384(3)$ MHz and $\Delta_{\text{MW}}^{(-)} = -6.381(1)$ MHz. Here, we transferred the ensembles of both sides of the fiber with one MW π -pulse at the same time. For $\varphi_B = 5^\circ$ [Fig. 5.14 (b)] the MW resonances are found at $\Delta_{\text{MW}}^{(+)} = -6.371(1)$ MHz and $\Delta_{\text{MW}}^{(-)} = -6.403(1)$ MHz corresponding to a splitting of 31.1(8) kHz. Thus, already by tilting the polarization of the blue trapping light field by 5° we can selectively transfer one specific atomic ensemble: the resolution of the performed MW spectroscopy, set by the 40 μs -long π -pulse, is ≈ 25 kHz. The splitting can be further increased by increasing the tilt angle: For $\varphi_B = 8^\circ$ [Fig. 5.14 (c)] the MW resonance frequencies are found at $\Delta_{\text{MW}}^{(+)} = -6.358(1)$ MHz and $\Delta_{\text{MW}}^{(-)} = -6.419(1)$ MHz corresponding to a splitting of 60.7(9) kHz. For this splitting the two atomic ensembles are easily discernible via MW spectroscopy [50].

Theoretically, for $\varphi_B = 8^\circ$, we expect a splitting of the MW transition frequencies of ≈ 20 kHz. This calculation takes the small deformations of the trapping potential by the tilted polarization of the blue-detuned light field into account. When we consider this effect, we see that the position of the minimum is azimuthally displaced and the atoms actually experience a smaller magnetic field than at their original position ($x = \pm 480$ nm and $y = 0$ nm). We assume that the deviation of the expected splitting of 20 kHz with the measured value of 61 kHz is explained by an additional ellipticity of the blue-detuned light field. With the method we use to make fiber-guided light fields quasi-linearly polarized in the nanofiber, we can only ensure that the blue-detuned light field is correctly polarized for $\varphi_B = 0^\circ$ (see chapter 4.2.3). As soon as we turn the main direction of polarization of the quasi-linearly polarized light field, we might introduce a quasi-linearly polarized component that has its main direction of polarization orthogonal to the previous. This can be explained by a small birefringence of some optical components, e.g., dichroic mirrors, on the optical path of the light field before it is coupled into the TOF. Only a small fraction of $2 \cdot 10^{-4}$ of the orthogonal component is sufficient to induce additional fictitious magnetic fields that are strong enough to explain the measured splitting.

In Fig. 5.14, we can observe that the MW transition frequency $\Delta_{\text{MW}}^{(-)}$ of the atomic ensemble

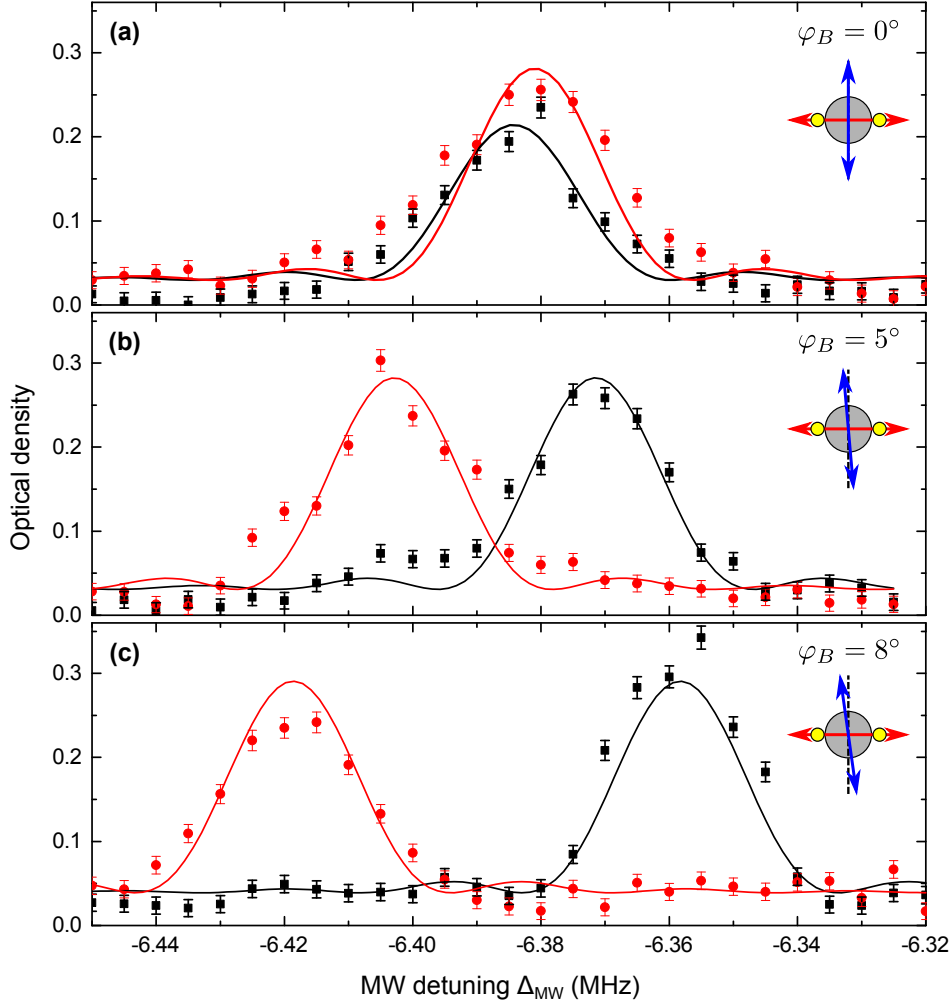


Figure 5.14: Optical density of the atomic ensemble trapped on the left side of the nanofiber (black data points) and of the ensemble trapped on the right side of the nanofiber (red data points) plotted as a function of the detuning of the MW frequency Δ_{MW} . The detuning is given with respect to the free space transition frequency of the $F = 3 \rightarrow F = 4$ hyperfine transition. The resulting spectra are obtained by transferring the atoms from $|F = 3, m_F = -3\rangle$ to $|F = 4, m_F = -3\rangle$ for different tilt angles **(a)** $\varphi_B = 0^\circ$, **(b)** $\varphi_B = 5^\circ$, **(c)** $\varphi_B = 8^\circ$ of the main direction of polarization of the blue-detuned trapping light field. Here, the pumping light field transferring the atoms in the outermost Zeeman substates propagates in the $-z$ direction.

trapped on the right side ($x > a$) of the nanofiber decreases for increasing φ_B . Whereas $\Delta_{\text{MW}}^{(+)}$ of the atomic ensemble trapped on the left side ($x < -a$) of the nanofiber increases for increasing φ_B . This fact is explained by the direction of the fictitious magnetic field induced by the blue-detuned trapping light field. In Fig. 5.13, we can see that $\mathbf{B}_{\text{fict}} \parallel \mathbf{B}_{\text{off}}$ for the ensemble at $x > a$. Thus, the total magnetic field increases for increasing φ_B . This means for the transition

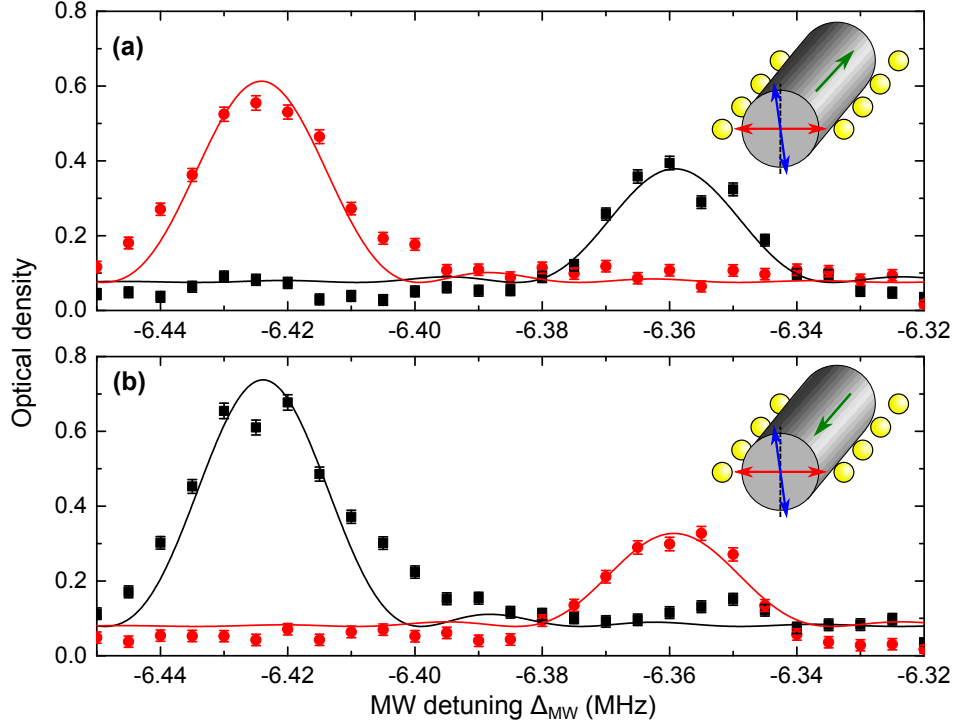


Figure 5.15: MW spectra as in Fig. 5.14 (c) with the optical pumping light field propagating in the (a) $-z$ direction and (b) $+z$ direction.

$|F = 3, m_F = -3\rangle \rightarrow |F = 4, m_F = -3\rangle$ that its transition frequency decreases. In contrast to this, \mathbf{B}_{fict} is anti-parallel to \mathbf{B}_{off} for the ensemble at $x < -a$. Thus, the total magnetic field decreases for increasing φ_B . This means that the transition frequency of the transition $|F = 3, m_F = -3\rangle \rightarrow |F = 4, m_F = -3\rangle$ increases.

Changed propagation direction of the optical pumping light field

Here, I show that the resonance $\Delta_{\text{MW}}^{(-)}$ ($\Delta_{\text{MW}}^{(+)}$) indeed correspond to the atomic ensemble trapped on the right (left) side of the nanofiber. In section 5.2.2, we could demonstrate that it is possible to selectively pump the two atomic ensembles into the different outermost Zeeman substates. In Fig. 5.15 (a), the MW spectrum of the $|F = 3, m_F = -3\rangle \rightarrow |F = 4, m_F = -3\rangle$ transition is again shown for $\varphi_B = 8^\circ$. Here, the optical pump light field propagates in the $-z$ direction: OD₋ (red data points) corresponds to the atoms trapped on right side of the nanofiber ($x > 0$) and OD₊ (black data points) corresponds to the atoms trapped on the left side of the nanofiber ($x < 0$). In Fig. 5.15 (b), the propagation direction of the pumping light field is reversed to the $+z$ direction: OD₋ (red data points) now corresponds to atoms trapped on the left side of the nanofiber and OD₊ (black data points) corresponds to atoms on the right side of the nanofiber. Recall that OD₋ (OD₊) is the optical density of the atomic ensemble that has been pumped to the $|F = 4, m_F = -4\rangle$ ($|F = 4, m_F = +4\rangle$) state. Thus, the resonance $\Delta_{\text{MW}}^{(-)}$ indeed

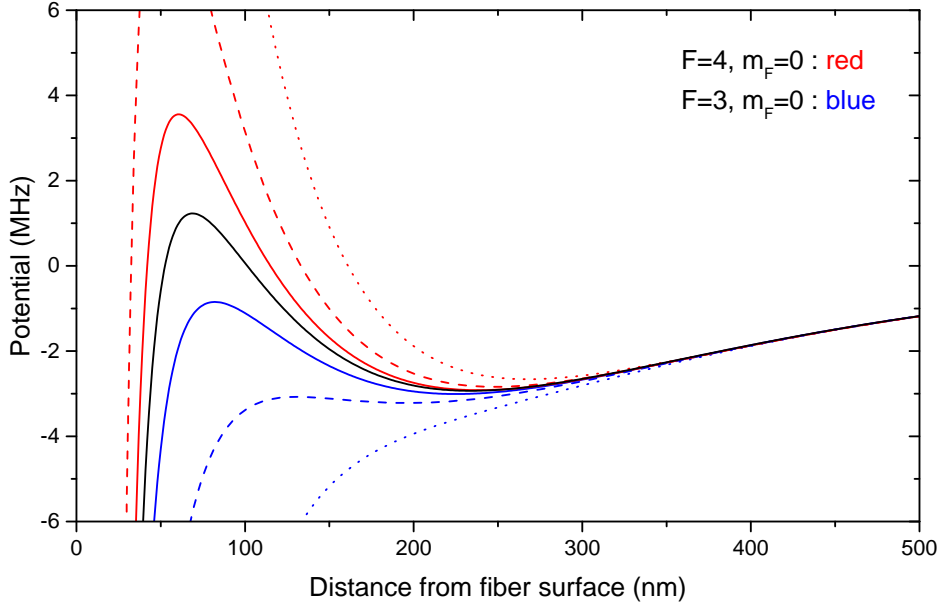


Figure 5.16: Trapping potentials in radial direction of the $|F = 4, m_F = 0\rangle$ ($|F = 3, m_F = 0\rangle$) ground state plotted in red (blue) for different powers P_{880} of the light field at the tune-out wavelength: solid black line $P_{880} = 0$ mW. For the colored solid, dashed, and dotted lines the power is $P_{880} = 3.5$ mW, $P_{880} = 6$ mW, and $P_{880} = 10$ mW, respectively. As shown in Fig. 5.9 (a), the induced fictitious magnetic field is ≈ 70 G/mW at the surface of the nanofiber ($x = a$ and $y = 0$). The plots are calculated for a power $P_{\text{blue}} = 8.5$ mW of the blue-detuned light field and a power $P_{\text{red}} = 2 \times 0.77$ mW of the red-detuned light field.

corresponds to the atomic ensemble on the right side of the nanofiber and can be transferred to $|F = 4, m_F = -4\rangle$ or to $|F = 4, m_F = +4\rangle$ for propagation of the pump light field in the $-z$ or $+z$ direction, respectively.

5.3.5 Limitations of the methods involving fictitious magnetic fields

In the measurements that are presented in the previous sections, we experimentally observed that a fictitious magnetic field of a certain strength distorts the trapping potential significantly. This manifests in a broadening of the MW transition, see, e.g., the broadened $m_F = 0$ to $m_F = 0$ clock transition in Fig. 5.10 (b). We attribute this to the fact that the trapped atoms move radially in a strong gradient of the fictitious magnetic field (see Fig. 5.9). This leads to position-dependent light shifts and, thus, to a distortion of the trapping potential. In Fig. 5.16, the trapping potentials of the $|F = 4, m_F = 0\rangle$ and $|F = 3, m_F = 0\rangle$ ground states are plotted for different powers of the light field at the tune-out wavelength. The plot reveals that the trapping potentials are significantly altered. Furthermore, the plot shows that the radial position of the minima of the trapping potential of the two hyperfine ground state moves in opposite directions. For $|F = 3, m_F = 0\rangle$ high fictitious magnetic fields ($P_{880} > 6$ mW) even lead to an opening of

the trap towards the nanofiber.

A similar behavior is observed on the first-order magnetic-field-sensitive transitions. For example, for the $|F = 3, m_F = -3\rangle$ ground state a fictitious magnetic field induced by $P_{880} \approx 200 \mu\text{W}$ is already sufficient to open the trap. For the method that uses the tilted polarization of the blue-detuned light field to induce fictitious magnetic fields, these distortions occur as well. However, for the measurements presented here (see Fig. 5.14) the transitions were not broadened and we therefore conclude that the deformation of the trap has still been small.

5.4 Optimizing the trapping potential

In the previous section, we have seen that the blue-detuned trapping light field induces fictitious magnetic fields on the trapped atoms when it is not purely linearly polarized at the position of the atoms. These fields are strong enough that their influence on the transition frequencies of the hyperfine ground states can be detected via MW spectroscopy, which we used to discern the two atomic ensembles on the two sides of the fiber. In addition, we can use this as a tool to get a better control over the polarization of the blue-detuned trapping light field. This will help to ensure that the light field is quasi-linearly polarized at the nanofiber and that the main direction of polarization is along the y axis.

In [39], we describe in detail a method to align the polarization of light fields that are launched into the TOF to be quasi-linearly polarized at the nanofiber, see as well chapter 4.2.3. In order to improve the adjustment of the polarization, we can now apply the new technique and observe the different MW transitions frequencies for the two atomic ensembles in dependency of the φ_B . In Fig. 5.17 (a), the result of such an exemplary measurement is shown. From a sinusoidal fit we conclude that the correct angle of the main direction of polarization can be set with a precision of $\approx \pm 0.1^\circ$. The minimal splitting of ≈ 20 kHz that is present in this measurement stems from the fact that for this measurement the polarization of the blue-detuned light field was not perfectly quasi-linearly polarized. With additional adjustment of the Berek compensator that controls the polarization of the blue-detuned light field this splitting was further reduced.

Furthermore, the standing wave of the red-detuned trapping light field can induce a fictitious magnetic field as well when it is not perfectly balanced in terms of power. A balanced quasi-linearly polarized nanofiber-guided standing wave is at every position perfectly linearly polarized [45]. Let the power of one beam of the standing wave be $P_{\text{red},1} = 0.77$ mW while the other beam has a power of $P_{\text{red},2} = f \cdot P_{\text{red},1}$. In Fig. 5.17 (b), the fictitious magnetic field induced at the level of the atoms by the red-detuned standing wave is shown in dependency of the imbalance factor f . Thus, with this tool we can balance the power of the red-detuned standing wave very precisely and thus reduce residual fictitious magnetic field at the positions of the atoms as well.

However, even for a perfectly aligned trap we still expect a broadened $|F = 3, m_F = -3\rangle \leftrightarrow |F = 4, m_F = -3\rangle$ transition. A MW spectrum of this transition is shown in Fig. 5.18, where the number of transferred atoms into the $F = 4$ manifold is plotted as a function of the MW detuning. Since the Landé-factors of the two hyperfine ground states have opposite signs, the fictitious magnetic field induced by the blue-detuned light field at azimuthal positions $\varphi \neq 0, \pi$ act differently on these states. This leads to the fact that the trapping potential of the

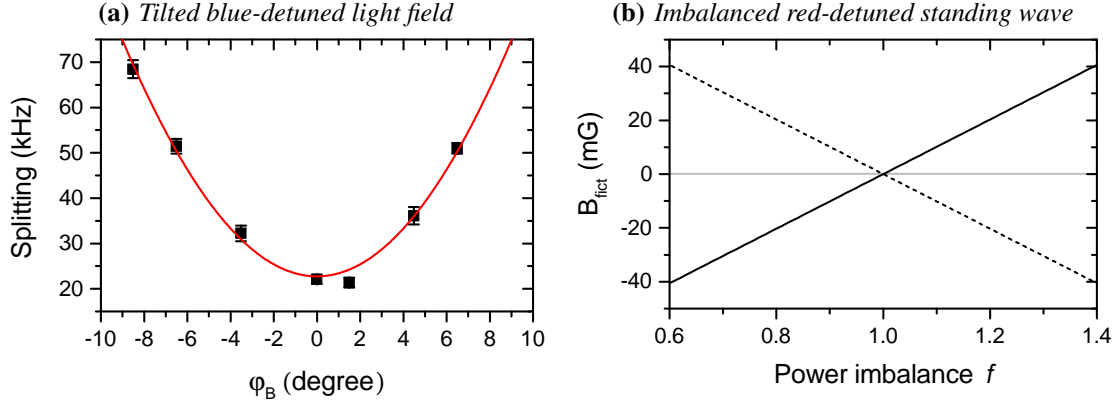


Figure 5.17: (a) The difference of the transition frequencies of the $|F = 3, m_F = -3\rangle \leftrightarrow |F = 4, m_F = -3\rangle$ transition depending on the tilt angle φ_B of the main direction of the polarization of the blue-detuned light field. (b) Calculation of the induced fictitious magnetic field by a red-detuned standing wave that consists of two light fields with different powers. The solid (dashed) line represents B_{fict} for the atoms trapped at $x = 480$ nm and $y = 0$ nm ($x = -480$ nm and $y = 0$ nm).

$|F = 3, m_F = -3\rangle$ state has a different shape than the trapping potential of the $|F = 4, m_F = -3\rangle$ state. When we approximate these trapping potentials to be harmonic, we get an azimuthal trapping frequency for $|F = 3, m_F = -3\rangle$ of ≈ 97 kHz and for $|F = 4, m_F = -3\rangle$ of ≈ 87 kHz. Since the atoms in the trap have a finite temperature, they are distributed over various vibrational states [43]. Thus, we expect a broadened MW transition. Here, we calculated a MW spectrum by furthermore taking the Franck-Condon factors for the different vibrational states into account. In Fig. 5.18, we plot the calculated spectrum for a temperature of the atomic ensemble $T = 10 \mu\text{K}$ (red solid line). Here, we shifted the frequency of the data points to match the center of the calculated spectrum and normalized them to its height. We find that the spectrum for the accurately aligned trap is in good agreement with the theoretically expected shape.

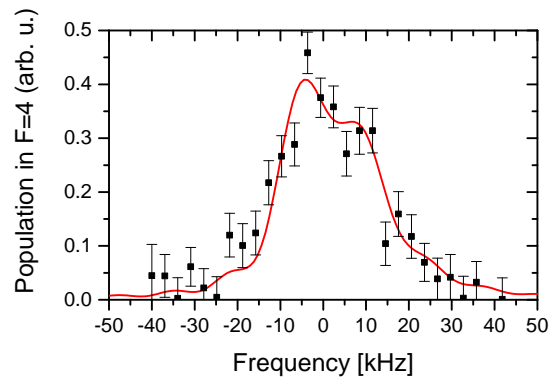


Figure 5.18: MW spectrum of the $|F = 3, m_F = -3\rangle \leftrightarrow |F = 4, m_F = -3\rangle$ transition for an accurately aligned trap. The solid line represents the calculated shape of the MW spectrum of this transition, taking into account the different azimuthal trap frequencies of the trapping potentials for the two states and a finite temperature of the atoms. See text for more information.

Nonreciprocal waveguide based on spin–orbit interaction

Classical or quantum electromagnetic fields possess angular momentum which is composed of a spin part and an orbital part [126]. The spin angular momentum (SAM) is an intrinsic (origin of space independent) quantity that is associated with the degree of circular polarization of the light field [32]. The orbital angular momentum (OAM) can exhibit both intrinsic and extrinsic behavior and thus is described as “quasi-intrinsic” [32, 126, 127]. For paraxial light fields, e.g., freely propagating and not-focused light fields, the SAM and the OAM are independent physical quantities. These light fields can be, e.g., tailored that they exhibit no SAM and carry an integer multiple of \hbar of OAM per photon, as it is the case for Gauss-Laguerre beams [128]. For the simple case of a circularly-polarized collimated Gaussian beam, the field has one \hbar of SAM per photon and no OAM.

When the light field is strongly confined by, e.g., focusing it with a high numerical aperture lens or by guiding it via a nanoscale waveguide, the field generally exhibits a significant spin–orbit interaction (SOI) [32]. That means that the orbital angular momentum and the spin angular momentum are not independent quantities anymore. In [65], it is presented that when a circular polarized light field is strongly focused, its spin angular momentum can partly be transferred to the orbital angular momentum. This was observed by the rotation of gold particles that interacted with tightly focused light. In [31], it is demonstrated experimentally that already non-confined classical light fields exhibit SOI when they propagate along a curved trajectory. The SOI in this experiment manifests in two phenomena: First, the light’s polarization state is affected by its curved trajectory. Second, the spin also affects the trajectory, i.e., a polarization-dependent perturbation of the trajectory occurs, which is revealed by a spatial separation of the light field into two beams with opposite circularity.

In the first part of this chapter, I will demonstrate that the spin–orbit interaction of the nanofiber-guided light fields leads to a directionality in the spontaneous emission of photons that are emitted by the trapped atoms into counter-propagating modes of the nanofiber. I will show that we can tailor the asymmetry of the scattering rates by changing the internal state of

the atoms and by suitably exciting them. In the second part of this chapter, I will show how the effect of SOI can lead to a nonreciprocal behavior of the system regarding the transmittance of a nanofiber-guided light field. Taking advantage of this effect, I will show the experimental realization of a nanofiber-based optical diode.

6.1 Directional spontaneous emission into optical nanofibers

It is possible to couple light into propagating electromagnetic surface waves in metal-dielectric nanostructure waveguides known as surface plasmon polaritons. In [129–131], it was shown that the SOI leads to directional launching of surface plasmon polaritons into these waveguides. These asymmetric scattering patterns have been observed recently as well in sub-wavelength hyperbolic metamaterials [132]. The directional scattering of photons, emitted by quantum dots into photonic-crystal waveguides, has been proposed [133, 134]. In [135], directional incoupling of the emission of a sub-wavelength nearfield probe source into a photonic-crystal waveguide has been demonstrated. In [136], the directional scattering of photons by a gold nanoparticle into a nanofiber has been studied in detail in dependency of the polarization of the excitation laser and the position of the nanoparticle.

Here, I will demonstrate that the SOI in our system leads to a directional spontaneous emission of photons into the nanofiber. We investigated this effect with nanofiber-trapped atoms as the photon emitters and observed an asymmetry of higher than 10:1 of the emission rates into counter-propagating nanofiber-guided modes.

We summarized the majority of the experiments that I present in this chapter in an article which is accessible on the ArXiv [51].

6.1.1 Basic idea of the experiment

I showed in chapter 2.3 that the sign of the spin angular momentum of the nanofiber-guided light field depends on the propagation direction. The polarization of a nanofiber-guided mode with its main direction of polarization along the x axis that propagates in the $+z$ direction exhibits, e.g., an almost unity overlap with σ^+ -polarization at the spatial position $x > a$ and $y = 0$ (see Tab. 2.1), with a being the radius of the fiber. Changing the propagation direction of the mode to the $-z$ direction the overlap with σ^- -polarization is almost unity. As before, the quantization axis is taken to be along the y axis.

In order to probe the propagation-depending polarization of the guided modes, we perform the following experiment. The principle of the experiment is sketched in Fig. 6.1. We prepare only one atomic ensemble on one side of the optical nanofiber. The atoms are then prepared in one outermost Zeeman substate $|F = 4, m_F = -4\rangle$. The next step is to excite the atoms with an external light field that propagates along the y axis. This light field is σ^- -polarized and thus drives the atoms on the cycling transition. A fraction of the purely σ^- -polarized light field that is scattered by the atoms is coupled into the nanofiber. This light is measured by two detectors positioned at the two outputs of the nanofiber. We will see that this light propagates preferentially in one direction through the nanofiber since it mostly couples to one mode. It is essential that we work with only one atomic ensemble. since the other atomic ensemble would

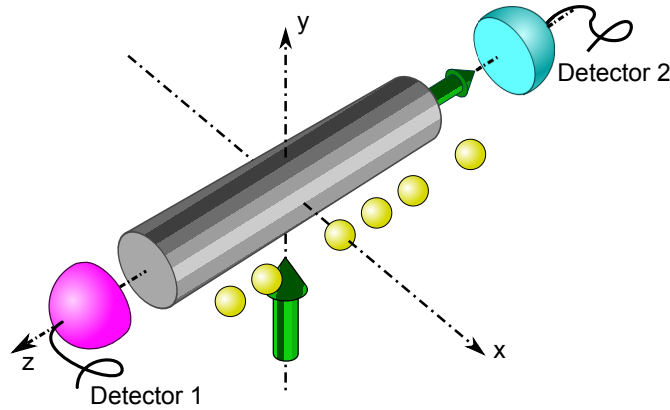


Figure 6.1: Schematic of the experiment: one atomic ensemble (yellow spheres) is trapped on one side of the nanofiber (gray cylinder) at the transverse position $x = 480$ nm and $y = 0$ nm. The atoms are excited by an external σ^- -polarized light field (vertical green arrow) propagating along the y axis. The fluorescence light that is emitted by the atoms into the fiber (horizontal green arrow) is measured by two detectors that are positioned at both ends of the fiber.

preferentially scatter in the opposite mode. Their combined emission would make it impossible to detect any directionality.

In the first part of this section, we will take a look at the electric field of the external excitation laser. Since the atoms are positioned only a few hundred nanometer away from the fiber, we may have to consider the scattering effects of the light field by the fiber. In the subsequent section I will show the experimental results and how the directionality can be tuned by changing the internal state of the atoms.

6.1.2 Light scattering by an optical nanofiber

In this section, I study the effect of light scattering by an infinite circular cylinder at normal incidence. I follow the approach outlined in [137]: the incoming light field is approximated as a plane wave that propagates along the y axis. As usual, the axis of the fiber is the z axis (see Fig. 6.2). The polarization of this light field can be decomposed into the two basis modes, the transverse magnetic (TM) and the transverse electric (TE) case. For the TM mode, the electric field is linearly polarized in a direction parallel to the cylinder axis (i.e. the z axis). For the TE mode, the electric field is linearly polarized in a direction parallel to the x axis. From these two basis modes, we can compose any polarization of the incoming light field.

The electric field outside the cylinder is the sum of the incident field E^{in} and the scattered field E^{scat} . They read for the

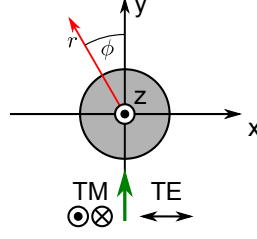


Figure 6.2: A plane wave propagates along the y axis (indicated by the green arrow). The polarization of the wave is either TM, where the electric field is linearly polarized along the z axis, or TE, where the electric field is linearly polarized along the x axis. The gray disk indicates the nanofiber. The spatial coordinates are given by r and ϕ . Note that the angle ϕ is measured with respect to the y axis.

- TM mode

$$E_z^{\text{in}}(r, \phi) = e^{ikr \cos \phi}, \quad (6.1)$$

$$E_z^{\text{scat}}(r, \phi) = -b_0 H_0^{(1)}(kr) - 2 \sum_{l=1}^{\infty} i^l b_l H_l^{(1)}(kr) \cos(l\phi), \quad (6.2)$$

- TE mode

$$\begin{aligned} E_r^{\text{in}}(r, \phi) &= \sin(\phi) e^{ikr \cos \phi}, \\ E_\phi^{\text{in}}(r, \phi) &= \cos(\phi) e^{ikr \cos \phi}, \end{aligned} \quad (6.3)$$

$$E_r^{\text{scat}}(r, \phi) = \frac{2i}{kr} \sum_{l=1}^{\infty} i^l a_l H_l^{(1)}(kr) \sin(l\phi),$$

$$E_\phi^{\text{scat}}(r, \phi) = i \left[a_0 H_0^{(1)}(kr) + 2 \sum_{l=1}^{\infty} i^l a_l H_l^{(1)}(kr) \cos(l\phi) \right]. \quad (6.4)$$

The coefficients a_l and b_l are [137]

$$\begin{aligned} a_l &= \frac{J_l'(n\kappa)J_l(\kappa) - nJ_l(n\kappa)J_l'(\kappa)}{J_l'(n\kappa)H_l^{(1)}(\kappa) - nJ_l(n\kappa)H_l^{(1)}(\kappa)}, \\ b_l &= \frac{nJ_l'(n\kappa)J_l(\kappa) - J_l(n\kappa)J_l'(\kappa)}{nJ_l'(n\kappa)H_l^{(1)}(\kappa) - J_l(n\kappa)H_l^{(1)}(\kappa)}, \end{aligned} \quad (6.5)$$

where $\kappa = ka$ is the size parameter and the prime indicates the first derivation with respect to the argument. The Hankel function of the first kind is defined as $H_l^{(1)}(x) \equiv J_l(x) + iY_l(x)$ with $J_l(x)$ and $Y_l(x)$ being the Bessel functions of the first and second kind, respectively. For these calculations, it is assumed that the cylinder is isotropic. Note that the only nonvanishing component of the TM mode is the z component. For the TE mode the nonvanishing components

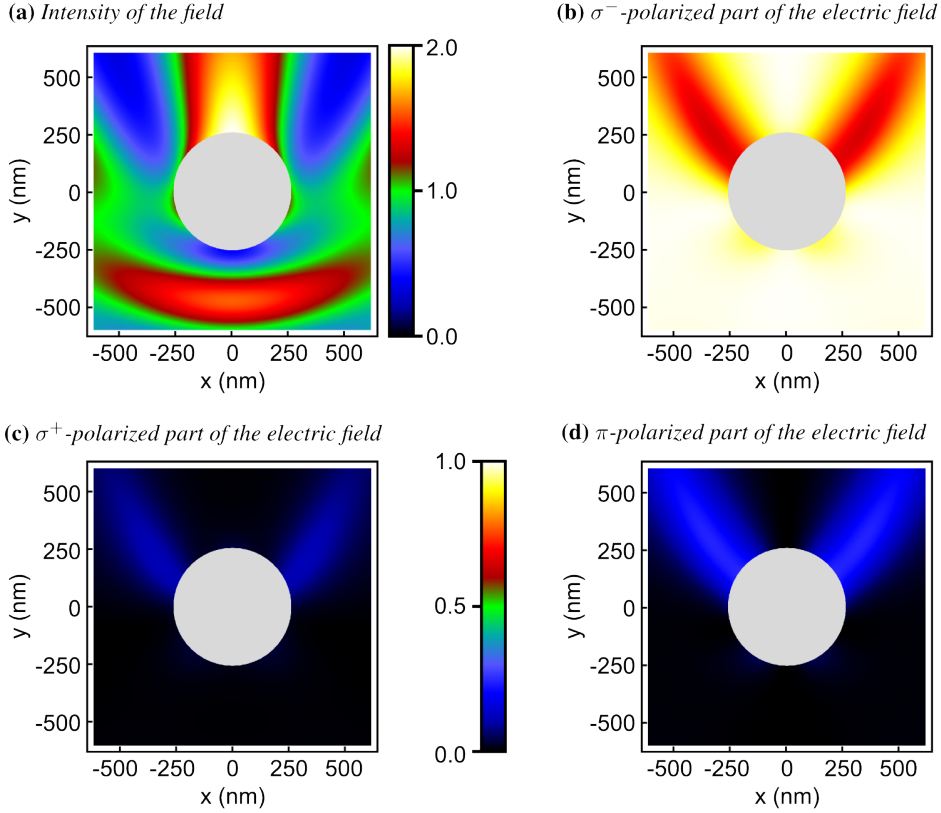


Figure 6.3: (a) Intensity and normalized polarization components (b) ξ_{σ^-} , (c) ξ_{σ^+} , and (d) ξ_{π} of a σ^- -polarized plane wave that propagates along the y axis and is scattered by the nanofiber. For this calculation the fiber radius is $a = 250$ nm, the wavelength of the incident light field is $\lambda = 852$ nm, and the quantization axis is chosen along the y axis. The intensity of the incident field is normalized to one.

are the r and the ϕ component. The electric field outside the fiber for, e.g., a σ^- -polarized incident field can be composed from the two basis modes

$$\mathbf{E}^{\sigma^-} = \frac{1}{\sqrt{2}} (\mathbf{E}^{\text{TE}} - i\mathbf{E}^{\text{TM}}) . \quad (6.6)$$

Thus, the r , ϕ , and z component of \mathbf{E}^{σ^-} are:

$$E_r^{\sigma^-}(r, \phi) = \frac{1}{\sqrt{2}} (E_r^{\text{in}}(r, \phi) + E_r^{\text{scat}}(r, \phi)) , \quad (6.7)$$

$$E_\phi^{\sigma^-}(r, \phi) = \frac{1}{\sqrt{2}} (E_\phi^{\text{in}}(r, \phi) + E_\phi^{\text{scat}}(r, \phi)) , \quad (6.8)$$

$$E_z^{\sigma^-}(r, \phi) = -\frac{i}{\sqrt{2}} (E_z^{\text{in}}(r, \phi) + E_z^{\text{scat}}(r, \phi)) . \quad (6.9)$$

With this information, we can take a look how the intensity and the polarization of a σ^- -polarized plane wave impinging on the nanofiber are altered by the presence of the latter. In Fig. 6.3 (a), we plot the intensity of the light field that propagates in the y direction. The intensity has been normalized to the intensity of the incident light field. The plot reveals that the intensity can be tremendously changed: behind the fiber ($x = 0$ nm and $y = a = 250$ nm) constructive interference of the incident and scattered light field leads to a two-fold increase of the intensity, whereas in front of the fiber ($x = 0$ nm and $y = -250$ nm) the fields interfere destructively and the intensity is reduced by more than 50 %. However, at the position of the atoms ($x = \pm 480$ nm and $y = 0$ nm) the intensity is almost not altered by the presence of the fiber and is decreased by only ≈ 1.5 %.

The part of the light field that is σ^- -, σ^+ -, and π -polarized is given in the spherical tensor basis by $\xi_j = |\mathcal{E}_j^2|/|\mathcal{E}^*\mathcal{E}|^2$ with $j \in (\sigma^+, \pi, \sigma^-)$. The ξ_j are plotted in Fig. 6.3 (b), (c), and (d), respectively. These plots reveal as well that the change of the polarization can be significant, e.g., the part of the light that is σ^- -polarized is decreased maximally by almost 35 %. However, at the position of the atoms the polarization is almost not altered at all with $\xi_{\sigma^-} = 0.983$.

Note that these small changes in intensity and polarization are exactly the same for the atoms positioned on the left and on the right side of the nanofiber. Nevertheless, in the experimental setup the external light field hits the fiber under a small angle in the x - y plane. This leads to small deviations of the intensity and the ξ_j between the atomic positions on the left and on the right sides of the fiber. However, for tilt angles $\leq 5^\circ$ of the laser beam with respect to the nanofiber these deviations are still smaller than 2 %. In summary, to a very good approximation, the external light field at the position of the atoms is unperturbed by the presence of the nanofiber.

6.1.3 Experimental realization

For the experimental observation of directional spontaneous emission of photons by atoms into the nanofiber, we prepare one atomic ensemble on one side of the nanofiber, see Fig. 6.1. For this purpose, we make use of the techniques presented in chapter 5. For the first set of measurements, we prepare the atoms on one side of the nanofiber in the $|F = 4, m_F = -4\rangle$ state: The atoms of both atomic ensembles are initially distributed in the $F = 4$ manifold. In a magnetic offset field $B_{\text{off}} = 3$ G that is applied to prevent spin flips we perform optical pumping into the $|F = 4, m_F = 0\rangle$ state, see chapter 5.2.1. The quantization axis is taken to be parallel to the magnetic field, i.e., along the y axis. In order to discern the two atomic ensembles, we use the technique presented in chapter 5.3.3: we send a light field at the tune-out wavelength with a power of $100 \mu\text{W}$ through the nanofiber. Thus, the degeneracy of the clock transition frequency for the two atomic ensembles is lifted. To enhance the effect of the tune-out light field, we apply a homogeneous magnetic offset field of $B = 28$ G as described before. Here, we chose to discern the atoms via the tune-out light field and not by tilting the polarization of the blue-detuned trapping light field. In principle, there should be no difference between the two techniques. But in the current experimental setup we can turn on and off the tune-out light field within one experimental run, whereas a tilt of the polarization cannot be change that fast since it has to be done manually. Thus, we can turn on the tune-out light field only for the time it is needed to discern the two ensembles in order to avoid a possible distortion of the trap as long as possible.

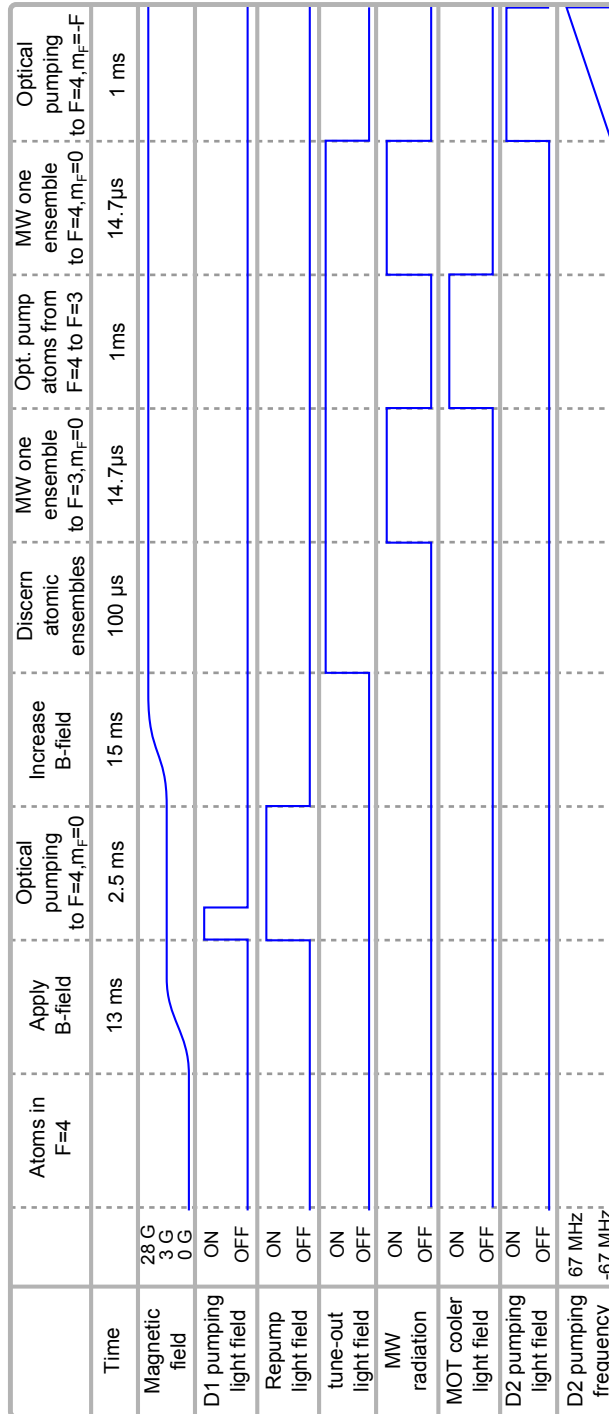


Figure 6.4: Experimental sequence to prepare one atomic ensemble in the $|F = 4, m_F = -4\rangle$ state. At the beginning of the sequence the atoms are in the $F = 4$ manifold.

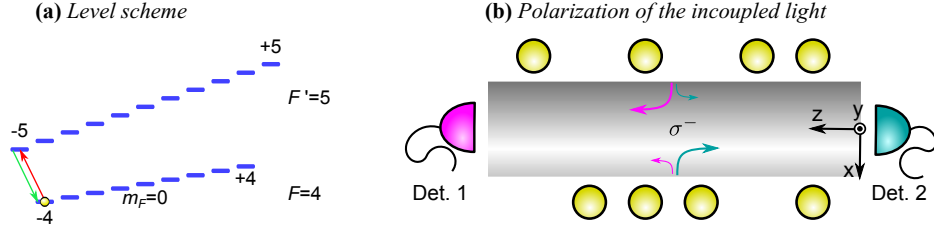


Figure 6.5: (a) Atomic level scheme of the $6^2S_{1/2}$, $F = 4$ ground state and the $6^2P_{3/2}$, $F' = 5$ excited state. The initial state of the atoms is indicated by the yellow sphere. The transition driven by the external laser is shown by the red arrow and the possible decay channel of the excited atom by the green arrow. (b) Sketch of the propagation direction of the light that is emitted by the atoms (yellow spheres) and coupled into the nanofiber (gray rectangle). The relative amount of light that propagates into a given direction is roughly indicated by the strength and the size of the arrows. Here, the polarization of the emitted light is σ^- .

Now, we transfer the atoms that are trapped on the left side of the nanofiber ($x < -a$) to the $|F = 3, m_F = 0\rangle$ state via a $14.7 \mu\text{s}$ -long MW π -pulse. All the atoms from both atomic ensembles that remained in the $F = 4$ manifold are now optically transferred to the $F = 3$ manifold. Here, we used a 1 ms -long pulse of the MOT cooler light fields. With the preceding experimental steps, we have emptied the $F = 4$ manifold and maximized the number of atoms of the atomic ensemble trapped on the left side of the fiber that are in $|F = 3, m_F = 0\rangle$. Via another MW π -pulse, which only addresses these atoms, they are transferred back into $|F = 4, m_F = 0\rangle$. Now, the only remaining atoms in the $F = 4$ manifold are in $|F = 4, m_F = 0\rangle$ and located on the left side of the fiber. All the other atoms that are still trapped are in the other hyperfine ground state. To finalize the preparation procedure the atoms are optically pumped to $|F = 4, m_F = -4\rangle$ by sending an optical pumping light field that propagates through the nanofiber in the $+z$ direction, see chapter 5.2.2. The experimental sequence is summarized in Fig. 6.4.

A resonant σ^- -polarized light field that propagates along the y axis drives the cycling transition $|F = 4, m_F = -4\rangle \leftrightarrow |F' = 5, m_{F'} = -5\rangle$ of the prepared atoms, see Fig. 6.5 (a). As we have seen in the previous section 6.1.2, at the position of the atoms the light field is virtually not altered by the presence of the fiber. On this closed transition the atoms can only emit σ^- -polarized light. The light that is scattered by the atoms into the nanofiber is detected by two SPCMs at both ends of the nanofiber: detector 1 (2) records the light that propagates in $+z$ ($-z$) direction. We record the number of photons on each detector within $20 \mu\text{s}$. In Fig. 6.6 (a) the number of photons detected by the two detectors as a function of time is plotted. The measurement reveals a drop of the signal which we attribute to the loss of atoms from the trap due to photon recoil heating because of the external light field. We integrate these signals over $10 \mu\text{s}$ and calculate the fractions η_1 and η_2 of the total incoupled light that is detected by detector 1 and detector 2, respectively, see Fig. 6.7 (a).

Then, this measurement is repeated but this time the atomic ensemble trapped on the right side of the nanofiber ($x > a$) is prepared in $|F = 4, m_F = -4\rangle$. In order to do so, the same experimental sequence is performed but the frequency of the MW π pulses is changed by \approx

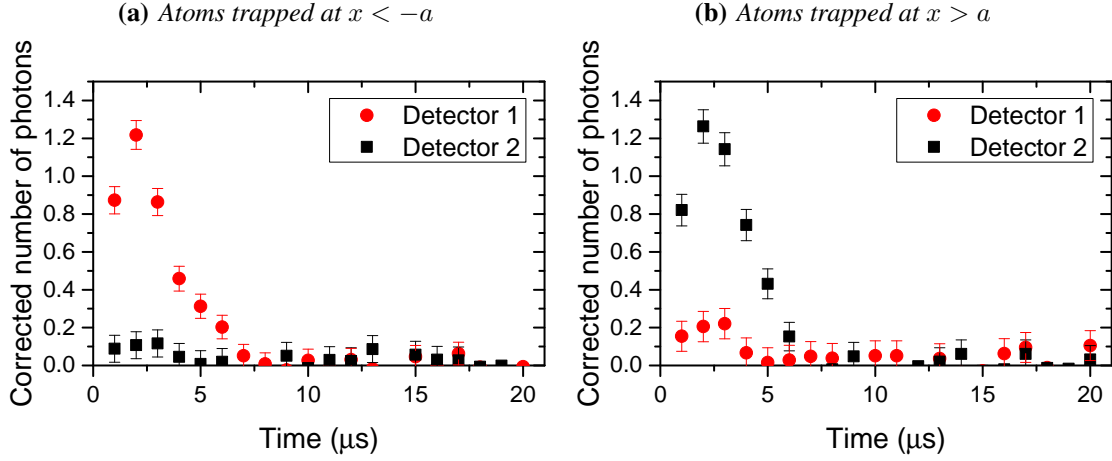


Figure 6.6: Number of photons that have been emitted into the $+z$ ($-z$) direction and measured by detector 1 (2) as a function of the time. The external light field illuminated the atoms that are prepared in $|F = 4, m_F = -4\rangle$ for $20 \mu\text{s}$. The counts given by the detector are converted into a number of photons by taking optical losses in the setup and the detector efficiency into account. Each data point was averaged over 3600 experimental runs and was corrected for background photons by recording and subsequently subtracting the signal without having atoms trapped.

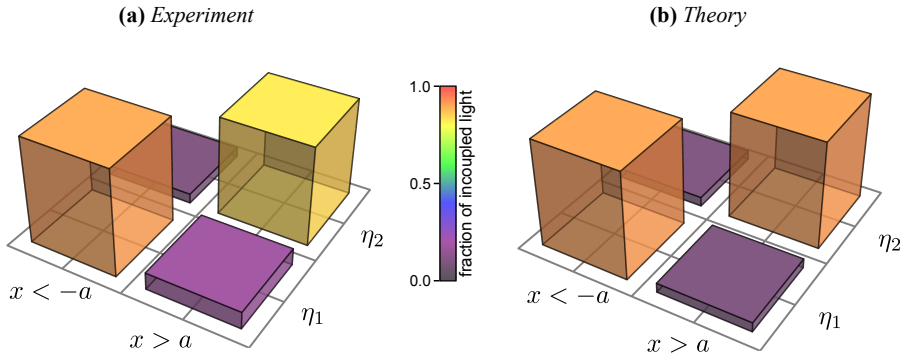


Figure 6.7: (a) Measurement results and (b) theoretical prediction of the fraction of incoupled light η_1 and η_2 emitted by the atoms on the left (right) side of the nanofiber at $x < -a$ ($x > a$) that is recorded by detector 1 and 2, respectively. Here, the atoms were prepared in $|F = 4, m_F = -4\rangle$.

30 kHz to address the clock transition of the atomic ensemble trapped on the right side of the fiber. For the final step of the sequence the atoms on the right side of the fiber that are in the $|F = 4, m_F = 0\rangle$ state have to be optically pumped to $|F = 4, m_F = -4\rangle$. Therefore, the propagation direction of the optical pumping light field is changed so that it propagated in the $+z$ direction. Then, the atoms are illuminated by the external σ^- -polarized light field and the photons that are scattered into the nanofiber are recorded, see Fig. 6.6 (b). The fractions η_1 and

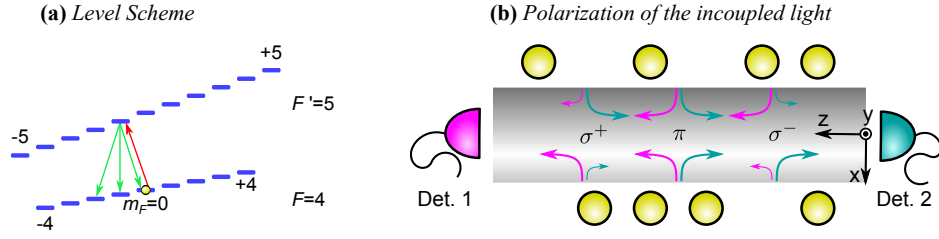


Figure 6.8: (a) Atomic level scheme of the $6^2S_{1/2}$, $F = 4$ ground state and the $6^2P_{3/2}$, $F' = 5$ excited state. The initial state of the atoms is indicated by the yellow sphere. The transition driven by the external laser is shown by the red arrow and the possible decay channels of the excited atom by the green arrows. (b) Sketch of the propagation direction of the light that is emitted by the atoms (yellow spheres) and coupled into the nanofiber (gray rectangle). The relative amount of light that propagates into a given direction is roughly indicated by the strength and the size of the arrows. Here, the polarization of the emitted light is σ^+ , π , and σ^- .

η_2 are plotted in Fig. 6.7 (a), as well. The experimental data is averaged over 3600 experimental runs.

When the atoms are located on the left side of the nanofiber ($x < -a$), then detector 1 records significantly more light ($\eta_1 = 92\% \pm 3\%$) than detector 2. The main propagation direction of the incoupled light is reversed, when the atoms are located on the right side of the nanofiber ($x > a$). Then, detector 2 records significantly more light ($\eta_2 = 86\% \pm 3\%$) than detector 1. The main propagation direction of the incoupled light for the two different scenarios is sketched in Fig. 6.5 (b). The theoretically expected values for η_1 and η_2 are plotted in Fig. 6.7 (b) and are in good agreement with our measurements. The theoretical model will be discussed in the next section. The experimental data reveal that the directionality given by the ratio of η_1 and η_2 for the atomic ensemble on the right side (1 : 6.1) is not as good as for the ensemble on the left side (11.5 : 1). This could be caused by the polarization of the external excitation light field that might be not fully σ^- -polarized at the position of the ensemble trapped on the right side. Nevertheless, from the calculations described in section 6.1.2 this should be ruled out. Another possibility is imperfect optical pumping: if the optical pumping light field that propagates in the $+z$ direction is not perfectly aligned to be quasi-linearly polarized in the nanofiber, the atoms may not all be optically pumped into $|F = 4, m_F = -4\rangle$. After being excited they then can emit, e.g., π -polarized light that couples with the same probability to both propagation modes which would reduce the contrast of the directional emission.

For the next set of measurements, we want to study how the directional emission depends on the polarization of the light emitted by the atoms. In order to do so, we change the internal state of the atoms and prepare them in $|F = 4, m_F = 0\rangle$: We follow the experimental sequence explained above, see Fig. 6.4, with the exception that we do not perform the last optical pumping step. Thus, at this time all the atoms that are trapped in the $|F = 4, m_F = 0\rangle$ are located on only one side of the nanofiber. The atoms are excited by a σ^- -polarized light field propagating along the y axis as before. The involved atomic levels and transitions are shown in Fig. 6.8 (a). Again, we perform a measurement for the atoms trapped on the left side ($x < -a$) of the nanofiber and

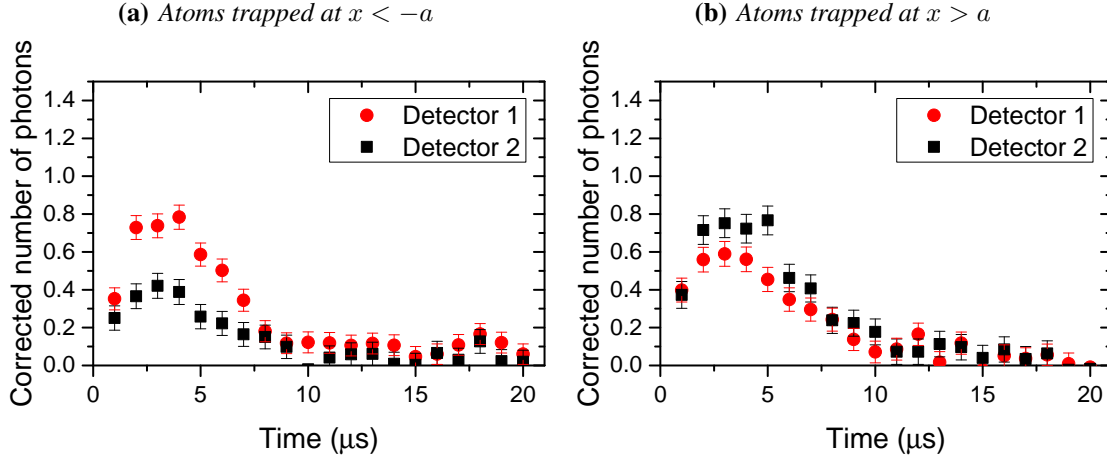


Figure 6.9: Number of photons that have been emitted into the $+z$ ($-z$) direction and measured by detector 1 (2) as a function of the time. The external light field illuminated the atoms that are prepared in $|F = 4, m_F = 0\rangle$ for $20 \mu\text{s}$. The counts given by the detector are converted into a number of photons by taking into account the coupling efficiency into the detector and the detector efficiency. Each data point was averaged over 4000 experimental runs and was corrected for the background.

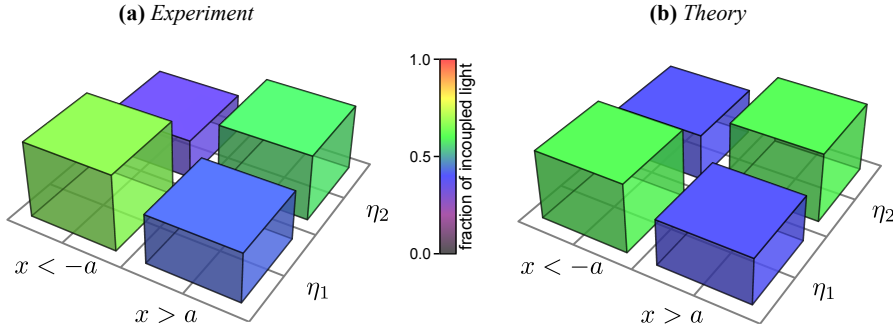


Figure 6.10: (a) Measurement results and (b) theoretical prediction of the fraction of incoupled light η_1 and η_2 emitted by the atoms on the left (right) side of the nanofiber at $x < -a$ ($x > a$) that is recorded by detector 1 and 2, respectively. The atoms were prepared in $|F = 4, m_F = 0\rangle$.

a measurement for the atoms trapped on the right side ($x > a$) of the nanofiber. The number of photons recorded by detector 1 and 2 is plotted as a function of time and shown in Fig. 6.9. The resulting fractions η_1 and η_2 are shown in Fig. 6.10 (a). The presented experimental data is the result of an average over 4000 experimental runs. Here, the emission of the light into the nanofiber is almost balanced. For the atoms trapped on the left (right) side of the nanofiber we find $\eta_1 = 66\% \pm 2\%$ ($\eta_2 = 57\% \pm 1\%$). The theoretically expected values for η_1 and η_2 are plotted in Fig. 6.10 (b) and are again in good agreement with our measurements.

The small deviations of the experimental results from the theory might be explained by optical pumping: While the external σ^- -polarized light field illuminates the atoms, it excites the atoms that are initially in $|F = 4, m_F = 0\rangle$. Since the atoms in this experimental setting are not on a cycling transition, optical pumping will occur to some extent. Nevertheless, the atoms will not be pumped to the outermost state since the atoms will be out of resonance after a few scattering processes. Due to the high magnetic field of $B_{\text{off}} = 28 \text{ G}$ the $|F = 4, m_F = -2\rangle \rightarrow |F' = 5, m_{F'} = -3\rangle$ transition is already detuned by $\approx 12 \text{ MHz}$ which is approximately twice the natural linewidth.

The results that are presented in this section, demonstrate that the emission of photons into the nanofiber in a given direction can be more than ten times stronger than in the opposite direction. Furthermore, the results show that we can qualitatively change the directional scattering of photons by changing the quantum state of the atomic emitter.

Theoretical estimation

To compare our results with a theoretical prediction, we make the following considerations: An atom that has been excited by the external light field has in general three possible decay channels. The probability for the atom to decay via a σ^+ , σ^- , or π transition is P_{σ^+} , P_{σ^-} , or P_{π} , respectively. In order to calculate the probability to scatter photons into a given nanofiber-guided mode, we use the overlap of the emitted polarization with the four basis modes that are summarized in Tab. 2.1. The basis modes have their main direction of polarization p along the x axis or along the y axis ($p = x$ or y) and propagate in the $+z$ or in the $-z$ direction. The probability of scattering into the $+z$ direction can be written as

$$\begin{aligned}
 P(+z) &= P(+z, p = x) + P(+z, p = y) \\
 &= P(+z, p = x|\sigma^+) \cdot P_{\sigma^+} + P(+z, p = x|\sigma^-) \cdot P_{\sigma^-} \\
 &\quad + \underbrace{P(+z, p = x|\pi)}_{=0} \cdot P_{\pi} \\
 &\quad + \underbrace{P(+z, p = y|\sigma^+)}_{=0} \cdot P_{\sigma^+} + \underbrace{P(+z, p = y|\sigma^-)}_{=0} \cdot P_{\sigma^-} \\
 &\quad + P(+z, p = y|\pi) \cdot P_{\pi}.
 \end{aligned} \tag{6.10}$$

The probabilities $P(+z, p|\sigma^+)$, $P(+z, p|\sigma^-)$, and $P(+z, p|\pi)$ that a σ^+ -, σ^- -, or π -polarized photon, respectively, is emitted into the p basis mode and propagates in the $+z$ direction are given by the product of two conditional probabilities: One is given by the overlap of the polarization of the emitted photon with the p basis mode, namely ξ_{σ^+} , ξ_{σ^-} , and ξ_{π} . The other contribution, denoted by $A_{\text{eff},x}$ ($A_{\text{eff},y}$), takes the effective area of the $p = x$ ($p = y$) basis mode at the position of the atom into account [101]. The effective area is defined as the ratio of the power in the nanofiber-guided mode and the intensity of evanescent field at the position of the atoms $A_{\text{eff}} = P/I(\mathbf{r}_{at})$ [138]. Thus, for an atom trapped on the left side of the nanofiber we get

$$P(+z) = 0.08 \cdot A_{\text{eff},x} P_{\sigma^+} + 0.92 \cdot A_{\text{eff},x} P_{\sigma^-} + A_{\text{eff},y} \cdot P_{\pi}. \tag{6.11}$$

For an atom that is prepared in the $|F = 4, m_F = 0\rangle$ state and then excited to the $|F' = 5, m_{F'} = -1\rangle$ state we have [120] $P_{\sigma^-} = 5/15$, $P_{\pi} = 8/15$, and $P_{\sigma^+} = 2/15$. In this

case, our calculation predicts for an atom located on the left side of the nanofiber that $\eta_1 = P(+z)/[P(+z) + P(-z)] = 60\%$ of the incoupled light is propagating in the $+z$ direction. Here, we have taken into account that the ratio of the effective areas for the two basis modes is given by $A_{\text{eff},y}/A_{\text{eff},x} = 0.36$. For an atom prepared in the $|F = 4, m_F = -4\rangle$ state and then excited to the $|F' = 5, m_{F'} = -5\rangle$ state the situation is even simpler, since $P_{\sigma-} = 1$ and $P_{\pi} = P_{\sigma+} = 0$. We therefore find $\eta_1 = 92\%$. The results of these calculations are in very good agreement with our experimental results and are shown in Fig. 6.7 (b) and Fig. 6.10 (b).

For these calculations, we considered only one atom. This is justified since the contributions of all atoms add up incoherently [40].

A general model to describe the scattering of light of an atom that is close to an optical nanofiber is given in [60]. Using this formalism, the absolute optical power that is emitted by an atom into a given nanofiber-guided mode can be calculated. This model further allows to study the emission behavior for an atom that has been prepared in a superposition of Zeeman substates.

6.2 Nanofiber-based optical diode

Analogously to electronic diodes that are nonreciprocal for an electrical current, a device that exhibits a nonreciprocal transmittance of a light field is called an optical diode. The most common optical diodes are based on the Faraday effect that is nonreciprocal and turns the direction of linearly polarized light depending on an applied magnetic field [139]. These so-called Faraday isolators require large magnetic fields and are usually several centimeters in size. The development of nanophotonic devices for optical signal processing purposes makes integrated, nano-scale optical isolators highly desirable and a matter of active research. Optical diodes based on Faraday rotation in chip-sized silicon waveguide-systems have been experimentally demonstrated in [140–142]. These works made use of fact that the magneto-optic materials used in the waveguides have high Faraday constants which allow miniaturizing of the device. Other works with chip-sized systems demonstrated that light shows nonreciprocal properties in parity-time-symmetric metamaterial waveguides: In [143], the symmetry breaking of light propagation in a coupled two-channel system was observed. In [144], unidirectional invisibility was demonstrated, which means that the reflection coefficient of the used waveguide is nonreciprocal. In [145], nonreciprocal mode conversion has been shown. However, the implementation of an optical diode has not been demonstrated in these systems yet [146].

Nevertheless, using nonlinear effects in optical waveguides [147] or microcavities [146,148], optical diodes have been realized. These implementations require high optical powers in order to work. This makes their use in single-photon applications impossible. However, such a single-photon diode would be of particular importance in quantum information processing protocols where single photons carry quantum information. Micron-sized optical diodes based on micro-resonators that should work at the single-photon level have been proposed in [149] and [150]. The first work proposes to make use of the nonlinear coupling between light and a mechanical mode inside a micro-resonator. The second work proposes to exploit the coupling of helicity-sensitive transitions between Zeeman levels of, e.g., a quantum dot to a micro-resonator.

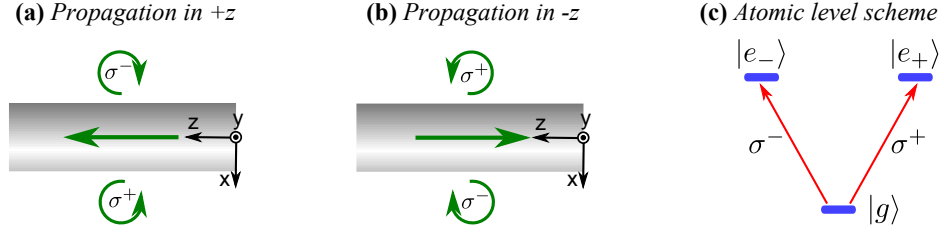


Figure 6.11: A light field that is quasi-linearly polarized along the x axis propagates along (a) the $+z$ direction and (b) the $-z$ direction (straight green arrow). Its polarization outside the nanofiber is sketched (curved green arrows) in the x - z plane, i.e., the plane containing the atoms. The quantization axis is taken to be the y axis. (c) Simplified atomic level scheme with the ground state $|g\rangle$ and the two excited states $|e_+\rangle$ and $|e_-\rangle$ that are coupled by σ^+ - and σ^- -transitions respectively.

In this section, I will report on the realization of an optical diode based on nanofiber-trapped atoms which could operate in the single-photon regime.

6.2.1 Basic idea of the nanofiber-based optical diode

In the previous chapters (see, e.g., chapter 2.2), I discussed the polarization properties of the quasi-linearly polarized fundamental nanofiber-guided modes. Let us consider a light field that propagates in the $+z$ direction and has its main direction of polarization along the x axis. The quantization axis is again taken to be along the y axis. At the position of an atom, e.g., at $x = 480$ nm and $y = 0$ nm, it is almost purely σ^+ -polarized, see Fig. 6.11 (a). For reasons of simplicity, let us assume that the light field is fully σ^+ -polarized at this position. The light field thus drives the $|g\rangle \rightarrow |e_+\rangle$ transition of an atom placed at this specified position, see Fig. 6.11 (c). When the light field propagates in the opposite direction, i.e., the $-z$ direction [see Fig. 6.11 (b)] it is σ^- -polarized at the position of the atom and drives the $|g\rangle \rightarrow |e_-\rangle$ transition of the atom.

In order to make this system nonreciprocal in terms of transmission of the light field, an imbalance between the absorptions of the σ^+ -polarization and the σ^- -polarization has to be realized. This can be achieved in two ways: First, a homogenous magnetic field can be applied, which lifts the degeneracy of $|e_-\rangle$ and $|e_+\rangle$. The frequency of the light field could then be tuned such that it is resonant with one transition and therefore out of resonant with the other. Second, in a multilevel atom, different transitions have different Clebsch-Gordan coefficients, i.e., not the same transition strengths. Both ways lead to the situation that the light field is more strongly absorbed for a certain propagation direction but less strongly for the opposite one.

In our system, we will combine the two methods: Additionally to the application of a strong magnetic offset field, we prepare the atoms in an outermost Zeeman substate $|F = 4, m_F = \pm 4\rangle$. There, the strength of the $|F = 4, m_F = \pm 4\rangle \rightarrow |F' = 5, m_{F'} = \pm 5\rangle$ transition is 45 times larger than the $|F = 4, m_F = \pm 4\rangle \rightarrow |F' = 5, m_{F'} = \pm 3\rangle$ transition.

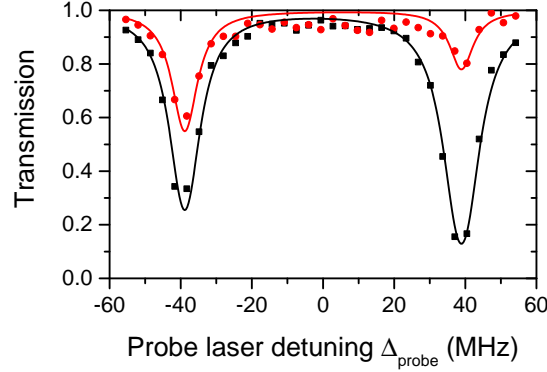


Figure 6.12: Transmission of a probe pulse as a function of its detuning Δ_{probe} . The probe pulse propagates along the $-z$ direction (black squares) and along the $+z$ direction (red disks). The solid lines are fits that yield the on-resonance transmission. Each data point corresponds to an average over 80 experimental realizations.

6.2.2 Experimental realization

To realize an optical diode with nanofiber-trapped atoms, we carried out the following steps: Initially, the atoms are prepared in the $F = 4$ manifold. Then, a magnetic offset field $B_{\text{off}} = 28$ G is applied along the y axis and the optical pumping procedure presented in chapter 5.2.2 is performed to transfer the trapped atoms into the outermost Zeeman substate. The optical pumping light field propagates in the $-z$ direction. Thus, the atomic ensemble on the left side of the nanofiber ($x < -a$) is transferred to the $|F = 4, m_F = +4\rangle$ state and the atomic ensemble on the right side ($x > a$) to the $|F = 4, m_F = -4\rangle$ state. Now, we probe the atoms with a light field that is resonant with the $F = 4 \rightarrow F' = 5$ transition and polarized like the pumping light field: quasi-linearly polarized with its main direction of polarization along the x axis ($p = x$). For these measurements, it propagates in the same direction as the pumping light field ($f = -z$). The transmission of a $300 \mu\text{s}$ -long probe pulse with a power of ≈ 0.8 pW is recorded and normalized to its transmission without trapped atoms. The signal without having atoms trapped is always measured in the same experimental run by turning off the red-detuned trapping light field for a few milliseconds, thereby expelling all atoms. A transmission spectrum is taken by repeating the measurement for different detunings of the probe light field and shown in Fig. 6.12 (black squares). The detuning of the probe light field Δ_{probe} is given with respect to the $F = 4 \rightarrow F' = 5$ transition of the trapped atoms without applying a magnetic offset field. In order to determine the on-resonance transmission, the spectrum is fitted with a function similar to Eq. (5.1), see solid black line. The fit will be explained in more detail later in this section. Here, we do not expect power broadening since the intensity of the propagating light field at the position of the atoms is only 2% of the saturation intensity of the strongest transition.

The transmission at the detuning of the probe light field $\Delta^{(-)} = -38.9 \pm 0.1$ MHz is $T_{-z}^{(-)} = 25 \pm 2\%$ and at $\Delta^{(+)} = 38.9 \pm 0.1$ MHz it is $T_{-z}^{(+)} = 13 \pm 1\%$. In Fig. 6.13, the involved transitions are sketched. At $\Delta^{(+)}$, the probe light field is resonant with the cycling tran-

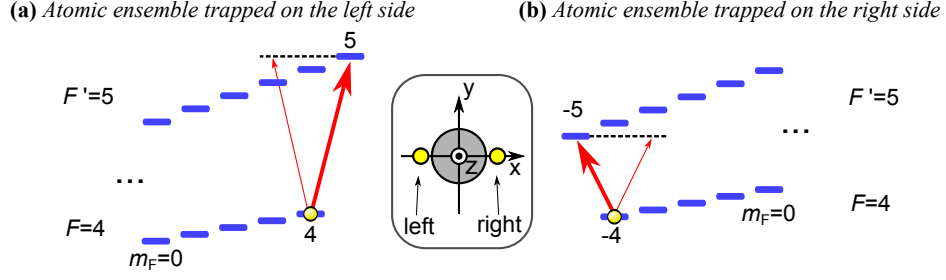


Figure 6.13: Level scheme and population of the atomic ensemble trapped on (a) the left side and (b) the right side of the nanofiber. The yellow spheres indicate that the atoms on the left (right) side have been pumped to $|F = 4, m_F = +4\rangle$ ($|F = 4, m_F = -4\rangle$). The red arrows indicate the probe light field at (a) $\Delta^{(-)}$ and (b) $\Delta^{(+)}$. The thickness of the arrow indicates the relative strength of the light field's polarization components. The probe light field propagates in the $-z$ direction.

sition $|F = 4, m_F = 4\rangle \rightarrow |F' = 5, m_{F'} = 5\rangle$. It therefore only addresses the atoms trapped on the left side of the nanofiber since they have been pumped into $|F = 4, m_F = 4\rangle$. At this position, the the probe light field is mostly σ^+ -polarized ($\xi_{\sigma^+} = 92\%$). Thus, the probe light field is absorbed by the atoms and its transmission is reduced. The small part of the light field that is σ^- -polarized is detuned by 31 MHz with respect to the $|F = 4, m_F = 4\rangle \rightarrow |F' = 5, m_{F'} = 3\rangle$ transition. The other dip in the transmission spectrum is found at a detuning of the probe light field of $\Delta^{(-)}$. At this detuning the probe light field is resonant with the cycling transition $|F = 4, m_F = -4\rangle \rightarrow |F' = 5, m_{F'} = -5\rangle$. Thus, it only addresses the atoms trapped on the right side of the nanofiber since they have been pumped into $|F = 4, m_F = -4\rangle$. At this position the polarization of the probe light field is mostly σ^- -polarized ($\xi_{\sigma^-} = 92\%$). Thus, the probe light field with this detuning is absorbed as well and its transmission is reduced.

Now, the measurement is repeated for a probe light field that propagates in the $+z$ direction, whereas the optical pumping light field still propagates in the $-z$ direction. The transmission spectrum resulting from this measurement is shown in Fig. 6.12 (red disks). The fit of the data yields a transmission $T_{+z}^{(-)} = 55 \pm 2\%$ at $\Delta^{(-)}$ and $T_{+z}^{(+)} = 78 \pm 2\%$ at $\Delta^{(+)}$. The involved level schemes for the trapped atoms are sketched in Fig. 6.14. Here, at $\Delta^{(+)}$ the light field is resonant with the $|F = 4, m_F = 4\rangle \rightarrow |F' = 5, m_{F'} = 5\rangle$ transition. But only a small fraction $\xi_{\sigma^+} = 8\%$ of the light field on the left side of the fiber is σ^+ -polarized and can drive this transition. The major part of the probe light field is σ^- -polarized ($\xi_{\sigma^-} = 92\%$). But this polarization component cannot significantly drive the $|F = 4, m_F = 4\rangle \rightarrow |F' = 5, m_{F'} = 3\rangle$ transition since it is detuned by 31 MHz. Furthermore, the strength of this transition given by the Clebsch-Gordon coefficients is by a factor of 45 smaller than the strength of the $|F = 4, m_F = 4\rangle \rightarrow |F' = 5, m_{F'} = 5\rangle$ transition [120]. Thus, the absorption of the probe light field by the atoms is drastically decreased, i.e., its transmission is higher. The fact that the transmission at $\Delta^{(-)}$ is higher than for the case where the probe and the pumping light field are co-propagating can be explained analogously [see level scheme in Fig. 6.14 (b)].

These results show that the on-resonance transmission of a probe light field depends strongly

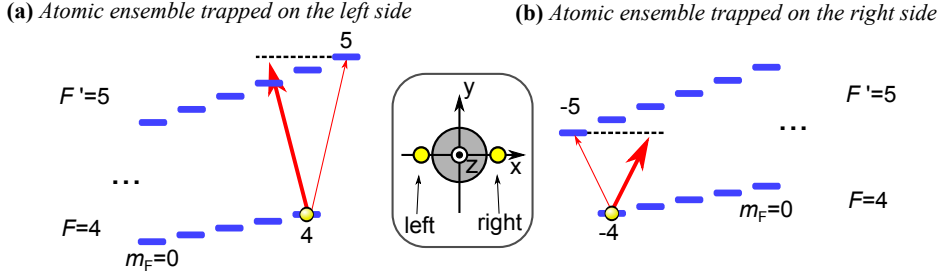


Figure 6.14: Level scheme and population of the atomic ensemble trapped on (a) the left side and (b) the right side of the nanofiber. The yellow spheres indicate that the atoms on the left (right) side have been pumped to $|F = 4, m_F = +4\rangle$ ($|F = 4, m_F = -4\rangle$). The red arrows indicate the probe light field at (a) $\Delta^{(-)}$ and (b) $\Delta^{(+)}$. The thickness of the arrow indicates the relative strength of the light field's polarization components. The probe light field propagates in the $+z$ direction.

on its propagation direction through the nanofiber. The on-resonance transmission at $\Delta^{(+)}$ is about 6 times larger for propagation of the probe light field in the $-z$ direction than in the $+z$ direction, i.e., co- and counter-propagating with the pumping light field, respectively. At $\Delta^{(-)}$, the on-resonance transmission differs by a factor of about 2.2 for the different propagation directions of the probe light field.

The nonreciprocal behavior in the transmission of a light field can be used to realize a nanofiber-based optical diode: a light field is absorbed when it is resonant with one of the two atomic ensembles and is launched into the fiber in one direction. However, when the same light field propagates in the opposite direction, it is almost fully transmitted. According to the terminology used for diodes we will call the propagation directions blocking and passing direction, respectively. In the presented experimental realization the optical diode worked best for a light field at $\Delta^{(+)}$. Here, we obtain an isolation $\mathcal{I}^{(+)} = 10 \cdot \log(T_{+z}^{(+)} / T_{-z}^{(+)}) = (7.8 \pm 0.9)$ dB while the passing direction still shows a transmission of $T_{+z}^{(+)} = 78\%$.

The results show that, at $\Delta^{(-)}$, the figures of merit for our optical diode, i.e., transmission in passing direction and the isolation, are not as good as for $\Delta^{(+)}$. Since the dip in the transmission spectrum at $\Delta^{(-)}$ ($\Delta^{(+)}$) is caused by the atomic ensemble trapped on the right side (left side) of the nanofiber, the different behaviors might be explained as follows: For the diode in the blocking configuration ($f = -z$ for the probe light field), the absorption is not very high at $\Delta^{(-)}$. We attribute this fact to a small number of atoms trapped on the right side of the nanofiber. For the diode in the passing configuration ($f = +z$ for the probe light field), the transmission $\Delta^{(-)}$ is not very high, which we attribute to the fact that the optical pumping procedure was imperfect. We know from experimental observations that the atoms populate preferentially the negative m_F levels when they are initially loaded in the $F = 4$ manifold and a magnetic offset field is applied [101]. Therefore, for an imperfect optical pumping procedure not all atoms trapped on the left side of the nanofiber were pumped into $|F = 4, m_F = 4\rangle$ and some also stayed in $|F = 4, m_F = -4\rangle$. There, they can absorb the probe light field when its detuning is

$\Delta^{(-)}$ which leads to a reduced transmission.

In the next measurements, we study the performance of the diode while turning the main direction of polarization of the probe light field. Thus, we perform the same experimental steps described above and measure a transmission spectrum similar to the one shown in Fig. 6.12 for different angles ϕ_0 of the main direction of polarization of the probe light field. The preceding optical pumping light field is unchanged, i.e., it propagates along the $-z$ direction and has its main axis of polarization along the x axis.

For $\phi_0 = 0$ the main direction of polarization of the probe light field is along the x axis, which corresponds to the experimental situation described above. This means the light field drives σ^\pm -transitions and depending on its detuning and its propagation direction, the probe light field can be absorbed by the atoms on the $|F = 4, m_F = \pm 4\rangle \rightarrow |F' = 5, m_{F'} = \pm 5\rangle$ transition. For $\phi_0 = \pi/2$, the main direction of polarization is along the y axis and the light field is completely π -polarized at the position of the atoms. Thus, depending on the detuning the probe light can be absorbed by the atoms on the $|F = 4, m_F = \pm 4\rangle \rightarrow |F' = 5, m_{F'} = \pm 4\rangle$ transition. Note that this does not depend on the propagation direction of the probe light field (see chapter 2.2).

These measurements yield, for each setting of ϕ_0 , two transmission spectra similar to those presented in Fig. 6.12: one for each propagation direction of the probe light field. To obtain the on-resonance transmissions at $\Delta^{(+)}$, we fit all transmission spectra simultaneously with a function similar to Eq. (5.1) but taking into account four Lorentzians, corresponding to the $|F = 4, m_F = \pm 4\rangle \rightarrow |F' = 5, m_{F'} = \pm 5\rangle$ and $|F = 4, m_F = \pm 4\rangle \rightarrow |F' = 5, m_{F'} = \pm 4\rangle$ transitions. For this fit, the detunings of the four transitions are taken to be global fit parameters. The width of the transition Γ is fixed for the global fit and obtained by a separate fit of Eq. (5.1) to the data points (black squares) shown in Fig. 6.12. This is justified, because this data set shows the strongest dips in the transmission and is thus most sensitive to the width of the transition. This fit yields $\Gamma = 7.6 \pm 0.3$ MHz, which is slightly higher than the natural line width. This can be explained by the finite temperature of the atoms (see chapter 5.2.2).

In Fig. 6.15 the on-resonance transmissions at $\Delta^{(+)}$ for different angles ϕ_0 for a light field propagating in the $-z$ direction (black squares) and in the $+z$ direction (red disks) are shown. The plot reveals that for $\phi_0 = 90^\circ$ the transmissions $T_{+z}^{(+)}$ and $T_{-z}^{(+)}$ are almost the same and the system shows a reciprocal behavior. This is expected, since the light field drives the $|F = 4, m_F = 4\rangle \rightarrow |F' = 5, m_{F'} = 4\rangle$ transition independent of the light's propagation direction. Due to its weak transition strength that is 5 times weaker than the $|F = 4, m_F = 4\rangle \rightarrow |F' = 5, m_{F'} = 5\rangle$ transition, the total absorption is very weak. These results show that by changing the polarization of the probe light that propagates in the nanofiber, the system is either strongly nonreciprocal for the transmission of the probe light field or reciprocal.

Theoretical prediction

To explain the shape of the transmission depending on ϕ_0 , we model the transmission $T_{\pm z}(\phi_0)$ of a light field propagating in the nanofiber when a single atom is prepared in $|F = 4, m_F = 4\rangle$ on the left side of the nanofiber. We assume that the transmission can be decomposed in the

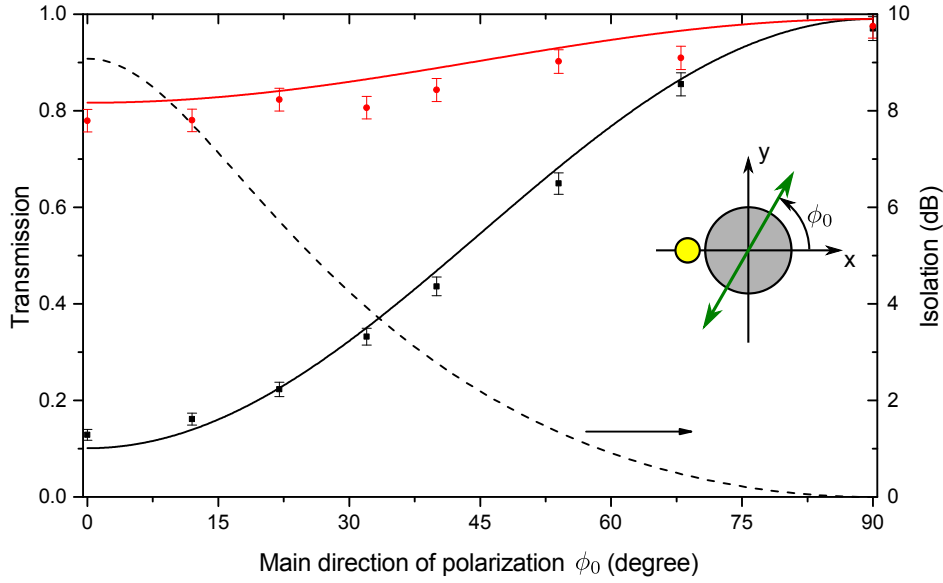


Figure 6.15: Transmission in the passing direction $+z$ (red disks) and in the blocking direction $-z$ (black squares) depending on the main direction of polarization ϕ_0 of the probe light field. The detuning is $\Delta^{(+)}$. The solid lines are fits to the data points that yield a mean atom number $\langle N \rangle = 27 \pm 1$. The dashed line is the isolation \mathcal{I} calculated from the fitted functions. The data points are averaged over 80 experimental runs.

following way:

$$T_{\pm z}(\phi_0) = t_{\pm z}^{90^\circ} + \left(t_{\pm z}^{0^\circ} - t_{\pm z}^{90^\circ} \right) \cos^2(\phi_0). \quad (6.12)$$

Here, the coefficients $t_{\pm z}^{0^\circ}$ and $t_{\pm z}^{90^\circ}$ are the transmissions of a light field that propagates in the $\pm z$ direction and has its main direction of polarization along the x axis ($\phi_0 = 0^\circ$) and along the y axis ($\phi_0 = 90^\circ$), respectively. These values can be calculated with the formalism presented in [151] and are tabulated for our trapping geometry in Tab. 6.1. Since we not only trap one but N atoms, we substitute the transmission coefficients $t_{\pm z}$ in Eq. (6.12) by $t_{\pm z}^N$. However, the number of trapped atoms fluctuates for different experimental realizations. When we assume that these fluctuations are Poissonian we can further substitute $t_{\pm z}^N$ by $\exp[-\langle N \rangle (1 - t_{\pm z})]$, where $\langle N \rangle$ is the mean number of trapped atoms. We fit the modified Eq. (6.12) to the data plotted in Fig. 6.15 and obtain $\langle N \rangle = 27 \pm 1$. From the fitted curves, we can calculate the isolation $\mathcal{I}(\phi_0)$ and plot it as well in Fig. 6.15 (dashed line): the highest isolation is obtained as expected for $\phi_0 = 0^\circ$, since the nonreciprocal behavior is the strongest for this angle.

Note that the only accurate method to obtain the number of trapped atoms is performing a saturation measurement. Here, the mean number of trapped atoms resulting from the fit depends on the transmission coefficients of a single atom. These coefficients result from calculations taking into account our trapping configuration. For deviations in, e.g., the powers of the trapping light fields, the distance of the atoms from the fiber could change and, thus, the actual trans-

$t_{-z}^{0^\circ}$	$t_{-z}^{90^\circ}$	$t_{+z}^{0^\circ}$	$t_{+z}^{90^\circ}$
91.39 %	99.96 %	99.24 %	99.96 %

Table 6.1: Transmission coefficients for a light field that propagates in the $\pm z$ direction through the fiber with its main direction of polarization along the x axis ($\phi_0 = 0^\circ$) or along the y axis ($\phi_0 = 90^\circ$) when one atom is trapped 230 nm away from the fiber surface and is prepared in the $|F = 4, m_F = 4\rangle$ state.

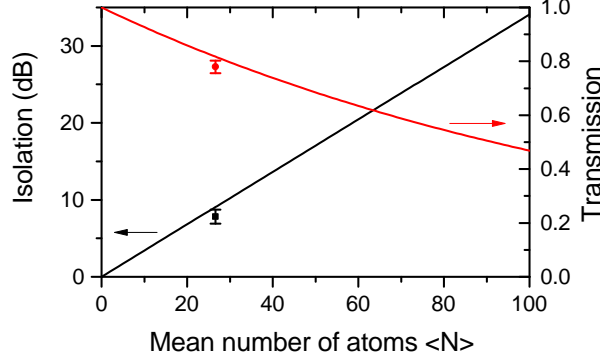


Figure 6.16: Calculated isolation \mathcal{I} (black line) and transmission $T_{+z}(0^\circ)$ in passing direction of the optical diode as a function of the mean atom number $\langle N \rangle$. The black and the red data point are the measured values for the isolation and the transmission, respectively, for $\phi_0 = 0^\circ$. As before, the quantization axis is taken to be along the y axis.

mission coefficients would deviate from the calculated values. Therefore, the mean number of trapped atoms $\langle N \rangle$ stated here has to be taken as a rough approximation.

In Fig. 6.16, the isolation and the transmission $T_{+z}(0^\circ)$ in passing direction is plotted as a function of the mean atom number $\langle N \rangle$. At $\langle N \rangle = 27$, we plotted the measured values for the isolation and the transmission in passing direction. The measured values are in reasonable agreement with the theoretical prediction. Remarkably, for higher atom numbers $\langle N \rangle \approx 100$ the predicted isolation reaches $\mathcal{I} = 34$ dB, while the predicted transmission in the passing direction only drops to $T_{+z}(0^\circ) = 47\%$. Thus, with our system, we should be able to realize an optical diode that exhibits high isolation while the transmission in the passing direction remains reasonably high. For comparison, the systems based on Faraday rotation in chip-sized silicon waveguides presented in [140, 142] exhibit similar values for the isolation (≈ 20 dB) and for the transmission in passing direction ($\approx 50\%$).

In order to optimize the optical diode, we could minimize the absorption of the mode that propagates in the $+z$ direction. Let us consider an atom that emits σ^- -polarized light ($q \equiv -1$) with respect to a quantization axis. The scattering coefficient into the mode that is quasi-linearly polarized and has its main direction of polarization along the x -axis can be written as [60]

$$\gamma^{(fx)} \propto (|e_r| \sin(\theta) + fq|e_z|)^2. \quad (6.13)$$

Here, θ is the angle between the x axis and the quantization axis. For all experimental real-

izations described in this thesis, the quantization axis coincided with the y axis, i.e., $\theta = 90^\circ$. Remarkably, for an angle

$$\theta_{\text{crit}} = f \arcsin \frac{|e_z|}{|e_r|} = 33.1^\circ, \quad (6.14)$$

the scattering into the mode polarized along x that propagates in the $+z$ direction ($f = 1$) is zero, whereas it is nonzero for the mode propagating in the other direction: $\gamma^{(\bar{f}x)} \neq 0$. This leads to the following situation at, e.g., the right side of the fiber ($x > a$): For a quantization axis along the y axis ($\theta = 90^\circ$) the overlap of the polarization of a light field that propagates in the $+z$ direction with σ^+ -, π -, and σ^- -polarization is $\xi_{\sigma^+} = 92\%$, $\xi_\pi = 0\%$, and $\xi_{\sigma^-} = 8\%$, respectively, see chapter 2.2. For a quantization axis with θ_{crit} , the overlaps are $\xi_{\sigma^+} = 46\%$, $\xi_\pi = 54\%$, and $\xi_{\sigma^-} = 0\%$. In Fig. 6.14, the level scheme for the situation $\theta = 90^\circ$ is shown. For $\theta = \theta_{\text{crit}}$ the part of the light fields represented in Fig. 6.14 by the thin arrows driving the $|F = 4, m_F = \pm 4\rangle \rightarrow |F' = 5, m_{F'} = \pm 5\rangle$ transition do not exist anymore. Thus, the absorption of the probe light is drastically reduced.

Nevertheless, there is still a π - and σ^\mp -polarized component that couples to the $|F = 4, m_F = \pm 4\rangle \rightarrow |F' = 5, m_{F'} = \pm 4\rangle$ and $\rightarrow |F' = 5, m_{F'} = \pm 3\rangle$ transitions, respectively and that can thus still be absorbed. This can be omitted when a magnetic offset field is applied along the quantization axis that shifts the π - and σ^+ -transitions out of resonance. In Fig. 6.17 (a), the transmission of the fiber-based optical diode is plotted for 27 atoms in dependency of the direction of the quantization axis for different B_{off} . The plot shows the expected behavior of maximal transmission for $\theta = \theta_{\text{crit}}$ for increasing B_{off} for a light field propagating in $+z$ direction. The absorption in blocking direction ($-z$) also decreases at this angle and, therefore, the isolation decreases as well [see Fig. 6.17 (b)]. Nevertheless, with the quantization axis at θ_{crit} the isolation could be increased by increasing the number of trapped atoms while maintaining a high transmission in passing direction.

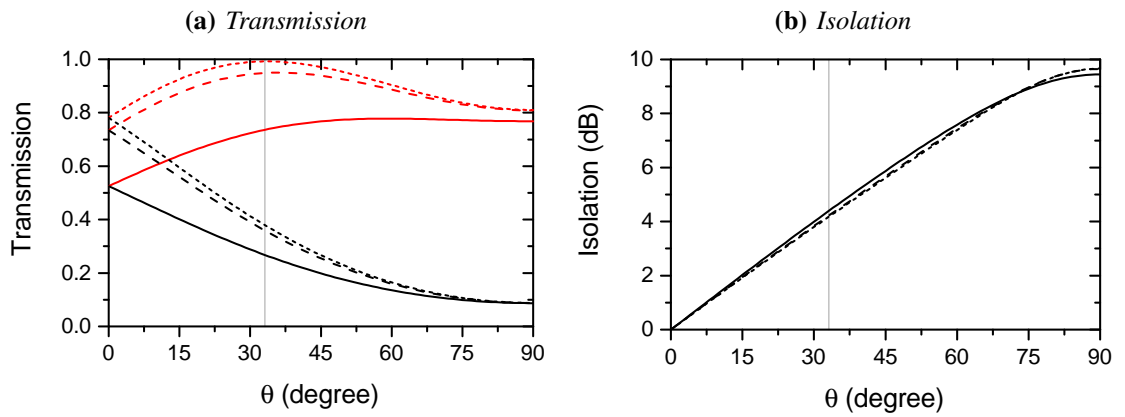


Figure 6.17: (a) Calculated transmission of a light field propagating in blocking direction ($-z$) (black lines) and in passing direction ($+z$) (red lines). (b) Isolation of the fiber based optical diode. The curves are calculated for $B_{\text{off}} = 0$ G (solid lines), $B_{\text{off}} = 10$ G (long-dashed lines), and $B_{\text{off}} = 28$ G (short-dashed lines). The gray vertical line marks $\theta_{\text{crit}} = 33.1^\circ$.

Summary & Outlook

In this thesis, the interaction of spin–orbit coupled light with trapped neutral atoms was investigated experimentally and theoretically. For this purpose, we trapped cesium atoms in the vicinity of an optical nanofiber. I described the fundamental mode that is guided by such a nanofiber and exhibits a prominent evanescent field. For such strongly confined light fields its spin and orbital angular momentum are coupled quantities. In particular, the fundamental quasi-linearly polarized nanofiber-guided mode exhibits a spin angular momentum that is purely transverse. Depending on the propagation directions of the light field the direction of the spin changes sign. I showed that the spin–orbit interaction manifests in the fact that the polarization of the nanofiber-guided light field is not only transverse polarized but also exhibits an azimuthally varying longitudinal component. This component is $\pi/2$ -phase shifted with respect to the transverse polarized components of the nanofiber-guided light field. Thus, the local polarization azimuthally varies from being almost completely σ^\pm -polarized to being completely π -polarized with respect to a quantization axis that is orthogonal to the fiber’s axis.

In the following, I showed how it is possible to trap neutral atoms in the evanescent field around such a nanofiber. The effect of the ac Stark interaction on the atoms in the nanofiber-based two-color dipole trap was investigated. I showed in particular that for the excited state’s energy levels of the trapped atoms m_F is, in general, not a good quantum number. However, an additional interaction with an external magnetic field leads, to some extent, to a situation where the atomic energy levels can again be described in the m_F -basis where m_F is a good quantum number. Moreover, it was discussed that the vector part of the ac Stark interaction has an effect on the Zeeman substates of the trapped atoms that can be treated as a magnetic field.

I demonstrated that the internal state of the trapped atoms can be manipulated via fiber-guided light fields. I showed in particular that we used the properties of the spin–orbit coupled light fields to prepare via optical pumping one of the two atomic ensembles that are trapped along the fiber in a different Zeeman substate than the other. Even when all atoms are prepared in the same Zeeman substate, it is possible to discern the two atomic ensembles with optical or microwave radiation. Here, we made use of fictitious magnetic fields induced by nanofiber-guided light fields. We can thus realize two different ensembles of the same atomic species that

are coupled to the same optical mode. These methods can be used for future experiments which I will describe in the next section. We used this technique to remove one atomic ensemble from the trap so that experiments with only one array of trapped atoms could be performed.

One ensemble of nanofiber-trapped atoms was used to demonstrate in a paradigmatic way how the spin-orbit interaction of the fiber-guided light fields influences the propagation direction of photons that were spontaneously emitted by the trapped atoms. I showed that the photons were scattered asymmetrically into counter-propagating nanofiber-guided modes. The achieved directionality of higher than 10:1 was experimentally demonstrated. I showed that this ratio depends on the one hand on the spatial position of the emitter relative to the nanofiber and on the other hand on the polarization of the emitted light. Thus, by changing the internal state of the atoms I showed that we can tailor the amount of light that is scattered in the counter-propagating modes. The experimental results can be well described by our theoretical model.

I demonstrated that the spin-orbit interaction can lead to the fact that our system is nonreciprocal with respect to the transmittance of a nanofiber-guided light field. The nonreciprocal behavior made it possible to realize a new type of a nano-scale optical diode. In the experiments conducted here, the optical diode transmitted almost 80 % of the light in passing direction and had an isolation of up to 8 dB.

In conclusion, the presented findings allowed to investigate, prepare, and manipulate the nanofiber-trapped atoms with a higher degree of freedom and precision than before. Furthermore, this work will improve the understanding of other systems where atoms or atom-like emitters are coupled to waveguides in the nonparaxial regime as well [152]. A few of such systems where atoms are involved are for example atoms coupled to plasmonic structures [153], nanophotonic cavities [154], or optical microtraps [155, 156]. The presented findings will have a significant impact on integrated optical signal processing with regard to the rise of technologies such as silicon photonics [157]. In particular, it paves the way towards an atom-mediated quantum photon router, in which the state of an atom controls the propagation direction of guided optical photons and which might thus constitute a central component for an optical quantum network [158]. The presented observations are also applicable for other strongly-confined optical fields [159].

Outlook

The experiments that will be conducted in the near future aim towards the realization of a fiber-integrated quantum memory. The next step that will be done on the way to store quantum information in the ensemble of nanofiber-trapped atoms is to observe electromagnetically induced transparency (EIT). For EIT an atomic medium that is initially opaque for a weak probing light field is rendered transparent by a classical control field. This is the result of destructive interferences of the excitation pathways. Figure 7.1 shows a Λ -type level scheme of the involved atomic energy levels. Not only that the probing light field is not absorbed on resonance under EIT conditions. It additionally experiences a steep normal dispersion around the resonance. This leads to a substantially reduced group velocity of a probing pulse within the atomic medium, known as slow light. Associated with the low group velocity is a spatial compression of the pulse leading to the fact that the probe pulse can be almost completely localized in the atomic medium. The

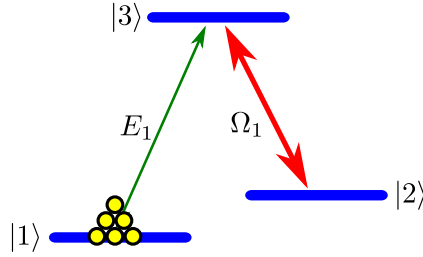


Figure 7.1: Λ -type level scheme: the two stable ground states $|1\rangle$ and $|2\rangle$ are coupled to the excited state $|3\rangle$ via a weak probing field E_1 and a classical control light field Ω_1 , respectively. The yellow circles indicate the atomic population in state $|1\rangle$.

light pulse can be even stopped, when the control field is turned off while the light pulse is localized inside the medium. EIT has been experimentally demonstrated for the first time in [160]. Slow light has been observed in [161, 162]. In [163, 164], the storage of light pulses in an atomic ensemble is reported.

In our system, the nanofiber-trapped atoms provide the required high optical densities and have ground state coherence times in the order of milliseconds. An early result on EIT is shown in Fig. 7.2. For this experiment the cesium atoms were prepared in the $|1\rangle \equiv |F = 4\rangle$ hyperfine manifold. While a control light field drives the $|2\rangle \equiv |F = 3\rangle \rightarrow |3\rangle \equiv |F' = 4\rangle$ transition, the transmission of a pulse of the weak probe light field is measured (red dots). The phase of the probe light field was stabilized with respect to the phase of the control light field via an optical phase-locked-loop [165]. For this measurement, the powers of the control field and the probe field were 500 pW and 20 pW, respectively. The measurement is repeated for different detunings of the frequency of the probe field with respect to the $|1\rangle \rightarrow |2\rangle$ transition. In Fig. 7.2 (b) a close-up of the transparency window is shown with a Gaussian line-shaped fit yielding a width of $\text{FWHM} = (1.53 \pm 0.04)$ MHz and an on-resonance transmission of $T_{\text{res}} = (47 \pm 3)\%$. Note that this measurement has been performed without a magnetic offset field. Thus, the transition that is inhomogeneously broadened due to ac Stark shifts and the presence of spin flips influenced the shape of the transmission window. We expect to have narrower transparency windows with a higher on-resonance transmission when a magnetic offset field is applied and single Zeeman sublevels are addressed. As explained in chapter 3.3.2, we need $B_{\text{off}} \approx 10$ G to overcome the excited state level mixing due to the ac Stark effect. The currently ongoing experiments show promising results regarding the EIT transmission signal, slow light, and storing of μs -long light pulses.

Nonlinear optics with single photons

Besides realizing a quantum memory with the nanofiber-trapped atoms, electromagnetically induced transparency in this system can be used to realize nonlinear optics with single photons. In order to observe the interaction of two light fields, high intensities with a large number of photons [166] are usually required, since the nonlinear susceptibilities of a material are typically

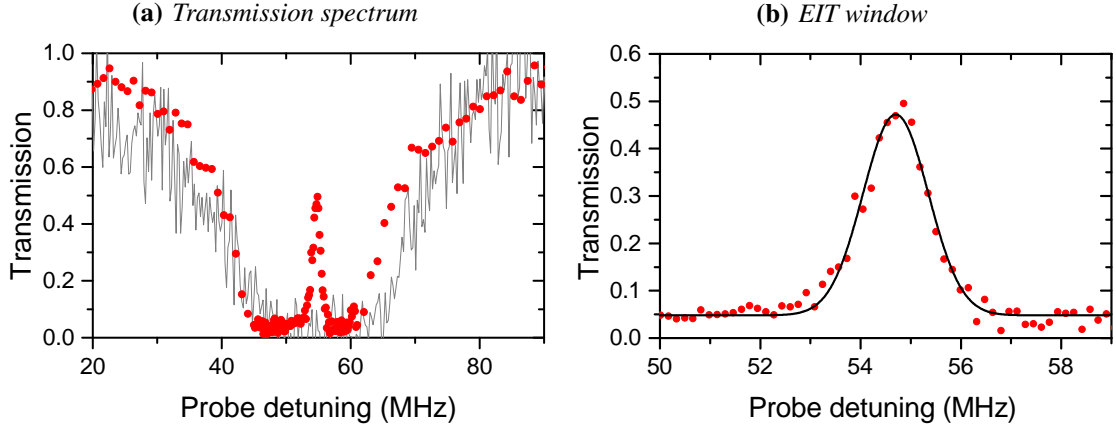


Figure 7.2: (a) Transmission spectrum of a weak probe field on the $|F = 4\rangle \rightarrow |F' = 4\rangle$ transition under EIT conditions (red data points). The gray line shows the transmission spectrum under the absence of the control light field, measured by sweeping the frequency of the probe light field within 5 ms continuously over the resonance. (b) Zoomed view of the transparency window. The black line is a fit yielding a width of the window $\text{FWHM} = 1.54$ MHz and the on-resonance transmission $T_{\text{res}} = 47\%$. Each data point has been averaged over 10 experimental runs.

very weak. In [167], a scheme is described that allows to observe the interaction of two weak light pulses down to single photons. The scheme is based on EIT and slow light involving two different atomic ensembles. In Fig. 7.3, the involved atomic levels for this scheme are sketched. A weak light field E_1 and a classical control field Ω_1 are used in a Λ type system (involving the levels of a first atomic ensemble $|A, 1\rangle$, $|A, 2\rangle$, and $|A, 3\rangle$). In this situation, we assume “EIT conditions” for E_1 , i.e., E_1 is transmitted lossless and with a reduced group velocity. Additionally, another weak light field E_2 is applied that is detuned by δ from the resonance of the $|A, 2\rangle \rightarrow |A, 4\rangle$ transition. This off-resonant light field induces a light shift of $|A, 2\rangle$ which alters the refractive index experienced by E_1 . Thus, via E_2 the phase of E_1 can be modulated, leading to cross-phase modulation (XPM) [168, 169]. Since E_1 propagates with a strongly reduced group velocity while the velocity of E_2 is basically not altered, the interaction time while XPM can occur is in principle very short. To reduce the group velocity of E_2 as well, it interacts with a second classical field Ω_2 , involving the another atomic species with the levels $|B, 1\rangle$, $|B, 2\rangle$, and $|B, 3\rangle$, see Fig. 7.3. In such a way, it is possible to realize similar group velocities for both quantum fields and a maximal interaction time. This scheme should allow for E_1 to experience a nonlinear phase shift controlled by E_2 [167]. In [170, 171] the possible implementation of XPM mediated by EIT as the basis to realize a “controlled-NOT” gate for all-optical quantum computing is discussed. In these works they describe the limitation of such a scheme when the two weak light fields are described by localized single-photon pulses: When one photon experiences a nonlinear phase shift of π , then the logical operation will not be a high fidelity process. However, it is still interesting to experimentally investigate the phase shift that can be maximally achieved by employing complex atomic multilevel structures.

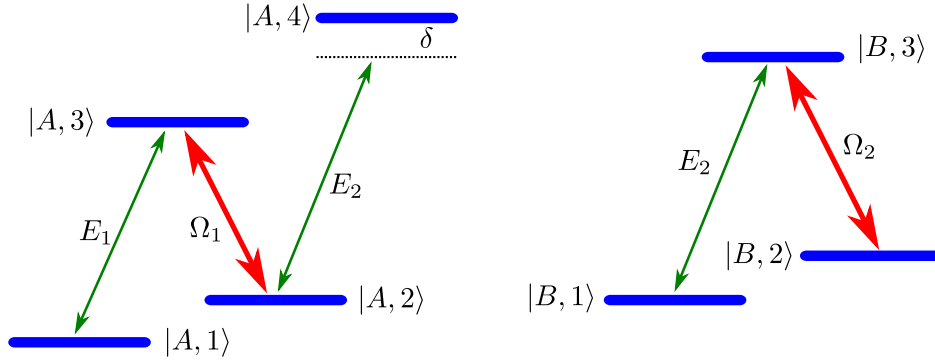


Figure 7.3: Double EIT scheme: on the left side the levels of the atomic ensemble A are shown providing a Λ -type system with a weak probe light field E_1 and a classical light field Ω_1 . A weak modulation light field E_2 is detuned by δ from resonance of the $|A, 2\rangle \rightarrow |A, 4\rangle$ transition. On the right side the levels of the atomic ensemble B are shown providing a Λ -type system with the weak probe light field E_2 and another classical light field Ω_2 . Original figure from [167].

Instead of realizing the two atomic species that are needed for this scheme by using two isotopes of, e.g., alkali atoms as it is proposed in [167], we can implement it using nanofiber-trapped atoms. In chapter 5, I showed that it is possible to realize two different atomic ensembles of the same species coupled to the same optical mode. This was achieved by using fictitious magnetic fields induced by fiber-guided fields. Thus, the two atomic ensembles trapped along the nanofiber experienced different shifts of their levels making them optically discernible by light fields propagating in the nanofiber. With this technique it should be possible to realize the scheme proposed in [167] in order to observe nonlinear interaction of single photons with only one atomic species. In [172, 173], the observation of all-optical switching is reported where only one atomic species (^{133}Cs) is used. However, in our systems we can combine the advantages of both systems: First, the usage of just one atomic species (as in [172, 173]) reduces the experimental requirements, e.g., there is no need for different laser systems to address different atomic species. Second, the usage of two discernible ensembles (as proposed in [167]) allows for higher flexibility in terms of selecting advantageous Λ -systems and adjusting the required EIT conditions for both weak light fields.

Bibliography

- [1] Royal Swedish Academy of Sciences. Measuring and manipulating individual quantum systems. Scientific Background on the Nobel Prize in Physics 2012, Oct 2012.
- [2] http://www.nobelprize.org/nobel_prizes/physics/laureates/2012, 2014. Accessed 2014-07-22.
- [3] David J. Wineland. Nobel Lecture: Superposition, entanglement, and raising Schrödinger's cat. *Rev. Mod. Phys.*, 85:1103–1114, Jul 2013.
- [4] D. Meschede and A. Rauschenbeutel. Manipulating single atoms. *Advances in Atomic, Molecular, and Optical Physics*, 53:75–104, 2006.
- [5] E. Fraval, M. J. Sellars, and J. J. Longdell. Method of Extending Hyperfine Coherence Times in $\text{Pr}^{3+}:\text{Y}_2\text{SiO}_5$. *Phys. Rev. Lett.*, 92:077601, Feb 2004.
- [6] Gopalakrishnan Balasubramanian, Philipp Neumann, Daniel Twitchen, Matthew Markham, Roman Kolesov, Norikazu Mizuochi, Junichi Isoya, Jocelyn Achard, Johannes Beck, Julia Tissler, Vincent Jacques, Philip R. Hemmer, Fedor Jelezko, and Jorg Wrachtrup. Ultralong spin coherence time in isotopically engineered diamond. *Nat Mater*, 8(5):383–387, May 2009.
- [7] J. R. Petta, A. C. Johnson, J. M. Taylor, E. A. Laird, A. Yacoby, M. D. Lukin, C. M. Marcus, M. P. Hanson, and A. C. Gossard. Coherent manipulation of coupled electron spins in semiconductor quantum dots. *Science*, 309(5744):2180–2184, 2005.
- [8] S. Kuhr, W. Alt, D. Schrader, I. Dotsenko, Y. Miroshnychenko, W. Rosenfeld, M. Khudaverdyan, V. Gomer, A. Rauschenbeutel, and D. Meschede. Coherence properties and quantum state transportation in an optical conveyor belt. *Phys. Rev. Lett.*, 91:213002, Nov 2003.
- [9] Ch. Roos, Th. Zeiger, H. Rohde, H. C. Nägerl, J. Eschner, D. Leibfried, F. Schmidt-Kaler, and R. Blatt. Quantum state engineering on an optical transition and decoherence in a paul trap. *Phys. Rev. Lett.*, 83:4713–4716, Dec 1999.
- [10] P. Zoller et al. Quantum information processing and communication. *The European Physical Journal D - Atomic, Molecular, Optical and Plasma Physics*, 36(2):203–228, 2005.

- [11] M. Wallquist, K. Hammerer, P. Rabl, and M. Lukin. Hybrid quantum devices and quantum engineering. *Phys. Scripta*, T137(T137):014001, 2009.
- [12] Nicolas Gisin, Grégoire Ribordy, Wolfgang Tittel, and Hugo Zbinden. Quantum cryptography. *Rev. Mod. Phys.*, 74:145–195, Mar 2002.
- [13] W. K. Wootters and W. H. Zurek. A single quantum cannot be cloned. *Nature*, 299(5886):802–803, October 1982.
- [14] H.-J. Briegel, W. Dür, J. I. Cirac, and P. Zoller. Quantum repeaters: The role of imperfect local operations in quantum communication. *Phys. Rev. Lett.*, 81:5932–5935, Dec 1998.
- [15] L.-M. Duan, M. D. Lukin, J. I. Cirac, and P. Zoller. Long-distance quantum communication with atomic ensembles and linear optics. *Nature Physics*, 414:413–418, Nov 2001.
- [16] L. Novotny and B. Hecht. *Principles of Nano-Optics*. Cambridge University Press, 2012.
- [17] Michael Bass, Eric W. Van Stryland, David R. Williams, and William L. Wolfe, editors. *Handbook of optics*, volume I. McGraw-Hill, Inc., 2 edition, 1995.
- [18] Melvin Lax, William H. Louisell, and William B. McKnight. From Maxwell to paraxial wave optics. *Phys. Rev. A*, 11:1365–1370, Apr 1975.
- [19] Lorenzo Cicchitelli, H. Hora, and R. Postle. Longitudinal field components for laser beams in vacuum. *Phys. Rev. A*, 41:3727–3732, Apr 1990.
- [20] D. Axelrod, T. P. Burghardth, and N. L. Thompson. Total internal reflection fluorescence. *Ann. Rev. Biophys. Bioeng.*, 13:247–268, 1984.
- [21] L. Novotny, M. R. Beversluis, K. S. Youngworth, and T. G. Brown. Longitudinal field modes probed by single molecules. *Phys. Rev. Lett.*, 86:5251–5254, Jun 2001.
- [22] Marlan O. Scully and M. S. Zubairy. Simple laser accelerator: Optics and particle dynamics. *Phys. Rev. A*, 44:2656–2663, Aug 1991.
- [23] Konstantin Y. Bliokh, Miguel A. Alonso, Elena A. Ostrovskaya, and Andrea Aiello. Angular momenta and spin-orbit interaction of nonparaxial light in free space. *Phys. Rev. A*, 82:063825, Dec 2010.
- [24] Andrea Aiello, Norbert Lindlein, Christoph Marquardt, and Gerd Leuchs. Transverse angular momentum and geometric spin hall effect of light. *Phys. Rev. Lett.*, 103:100401, Aug 2009.
- [25] Martin Neugebauer, Peter Banzer, Thomas Bauer, Sergej Orlov, Norbert Lindlein, Andrea Aiello, and Gerd Leuchs. Geometric spin hall effect of light in tightly focused polarization-tailored light beams. *Phys. Rev. A*, 89:013840, Jan 2014.

-
- [26] T. Kawalec, L. Józefowski, J. Fiutowski, M.J. Kasprówicz, and T. Dohnalik. Spectroscopic measurements of the evanescent wave polarization state. *Optics Communications*, 274(2):341 – 346, 2007.
- [27] K. Y. Bliokh and A. Aiello. Goos-Hänchen and Imbert-Fedorov beam shifts: an overview. *Journal of Optics*, 15(1):014001, 2013.
- [28] Xiaobo Yin, Ziliang Ye, Junsuk Rho, Yuan Wang, and Xiang Zhang. Photonic spin hall effect at metasurfaces. *Science*, 339(6126):1405–1407, 2013.
- [29] Masaru Onoda, Shuichi Murakami, and Naoto Nagaosa. Hall effect of light. *Phys. Rev. Lett.*, 93:083901, Aug 2004.
- [30] O. Hosten and P. Kwiat. Observation of the Spin Hall Effect of Light via Weak Measurements. *Science*, 319:787–, February 2008.
- [31] Konstantin Y. Bliokh, Avi Niv, Vladimir Kleiner, and Erez Hasman. Geometrodynamics of spinning light. *Nat Photon*, 2(12):748–753, December 2008.
- [32] K. Y. Bliokh, A. Aiello, and M. A. Alonso. *The Angular Momentum of Light*. Cambridge University Press, 2012.
- [33] Yutaka Yoshikawa, Kazumasa Satake, Takahisa Mitsui, and Hiroyuki Sasada. Can a linearly polarized light beam polarize atomic spin? *Optics Communications*, 190(1–6):173 – 178, 2001.
- [34] Christian Junge, Danny O’Shea, Jürgen Volz, and Arno Rauschenbeutel. Strong coupling between single atoms and nontransversal photons. *Phys. Rev. Lett.*, 110:213604, May 2013.
- [35] Christian Junge. *Cavity quantum electrodynamics with non-transversal photons*. PhD thesis, Technische Universität Wien, 2013.
- [36] Fam Le Kien, V. I. Balykin, and K. Hakuta. Atom trap and waveguide using a two-color evanescent light field around a subwavelength-diameter optical fiber. *Phys. Rev. A*, 70(6):063403, Dec 2004.
- [37] Jonathan P. Dowling and Julio Gea-Banacloche. Evanescent light-wave atom mirrors, resonators, waveguides, and traps. *Advances In Atomic, Molecular, and Optical Physics*, 37:1 – 94, 1996.
- [38] E. Vetsch, D. Reitz, G. Sagué, R. Schmidt, S. T. Dawkins, and A. Rauschenbeutel. Optical interface created by laser-cooled atoms trapped in the evanescent field surrounding an optical nanofiber. *Phys. Rev. Lett.*, 104(20):203603, May 2010.
- [39] E. Vetsch, S. T. Dawkins, R. Mitsch, D. Reitz, P. Schneeweiss, and A. Rauschenbeutel. Nanofiber-based optical trapping of cold neutral atoms. *IEEE Journal of Selected Topics in Quantum Electronics*, 18(6):1763–1770, Dec 2012.

- [40] D. Reitz, C. Sayrin, B. Albrecht, I. Mazets, R. Mitsch, P. Schneeweiss, and A. Rauschenbeutel. Backscattering properties of a waveguide-coupled array of atoms in the strongly nonparaxial regime. *Phys. Rev. A*, 89:031804, Mar 2014.
- [41] S. T. Dawkins, R. Mitsch, D. Reitz, E. Vetsch, and A. Rauschenbeutel. Dispersive optical interface based on nanofiber-trapped atoms. *Phys. Rev. Lett.*, 107:243601, Dec 2011.
- [42] P. Schneeweiss, S. T. Dawkins, R. Mitsch, D. Reitz, E. Vetsch, and A. Rauschenbeutel. A nanofiber-based optical conveyor belt for cold atoms. *Applied Physics B*, 110(3):279–283, 03 2013.
- [43] D. Reitz, C. Sayrin, R. Mitsch, P. Schneeweiss, and A. Rauschenbeutel. Coherence properties of nanofiber-trapped cesium atoms. *Phys. Rev. Lett.*, 110:243603, Jun 2013.
- [44] Daniel Reitz and Arno Rauschenbeutel. Nanofiber-based double-helix dipole trap for cold neutral atoms. *Optics Communications*, 285(23):4705 – 4708, 2012. Special Issue: Optical micro/nanofibers: Challenges and Opportunities.
- [45] C. Lacroûte, K. S. Choi, A. Goban, D. J. Alton, D. Ding, N. P. Stern, and H. J. Kimble. A state-insensitive, compensated nanofiber trap. *New J. Phys.*, 14(2):023056, February 2012.
- [46] A. Goban, K. S. Choi, D. J. Alton, D. Ding, C. Lacroûte, M. Pototschnig, T. Thiele, N. P. Stern, and H. J. Kimble. Demonstration of a state-insensitive, compensated nanofiber trap. *Phys. Rev. Lett.*, 109:033603, Jul 2012.
- [47] M. Hafezi, Z. Kim, S. L. Rolston, L. A. Orozco, B. L. Lev, and J. M. Taylor. Atomic interface between microwave and optical photons. *Phys. Rev. A*, 85:020302, Feb 2012.
- [48] D. E. Chang, J. I. Cirac, and H. J. Kimble. Self-organization of atoms along a nanophotonic waveguide. *Phys. Rev. Lett.*, 110:113606, Mar 2013.
- [49] J.-B. Béguin, E. Bookjans, S. L. Christensen, H. L. Sørensen, J. H. Müller, J. Appel, and E. S. Polzik. Generation and detection of a sub-Poissonian atom number distribution in a one-dimensional optical lattice. *ArXiv:1408.1266*, August 2014.
- [50] R. Mitsch, C. Sayrin, B. Albrecht, P. Schneeweiss, and A. Rauschenbeutel. Exploiting the local polarization of strongly confined light for sub-micrometer-resolution internal state preparation and manipulation of cold atoms. *Phys. Rev. A*, 89:063829, Jun 2014.
- [51] R. Mitsch, C. Sayrin, B. Albrecht, P. Schneeweiss, and A. Rauschenbeutel. Directional nanophotonic atom–waveguide interface based on spin–orbit interaction of light. *ArXiv:1406.0896*, June 2014.
- [52] Royal Swedish Academy of Sciences. Two revolutionary optical technologies. Scientific Background on the Nobel Prize in Physics 2009, Oct 2009.

-
- [53] http://www.nobelprize.org/nobel_prizes/physics/laureates/2009,2014. Accessed 2014-04-26.
- [54] A. W. Snyder and J. D. Love. *Optical Waveguide Theory*. Chapman and Hall, New York, 1983.
- [55] Amnon Yariv. *Optical Electronics in Modern Communications*. Oxford University Press, Inc., New York, 5th edition, 1997.
- [56] John David Jackson. *Classical Electrodynamics*. John Wiley & Sons, Inc, 3rd edition, 1999.
- [57] Guillem Sague. *Cold atom physics using ultra-thin optical fibres*. PhD thesis, Rheinische Friedrich-Wilhelms-Universität Bonn, 2008.
- [58] Fam Le Kien, S. Dutta Gupta, K. P. Nayak, and K. Hakuta. Nanofiber-mediated radiative transfer between two distant atoms. *Phys. Rev. A*, 72:063815, Dec 2005.
- [59] Fam Le Kien, V. I. Balykin, and K. Hakuta. Angular momentum of light in an optical nanofiber. *Phys. Rev. A*, 73:053823, May 2006.
- [60] Fam Le Kien and A. Rauschenbeutel. Anisotropy in scattering of light from an atom into the guided modes of a nanofiber. *arXiv:1406.0108*, 2014.
- [61] D. A. Varshalovich and V. K. Moskalev, A. N. Khersonskii. *Quantum Theory of Angular Momentum*. World Scientific, 1988.
- [62] K. Y. Bliokh, A. Y. Bekshaev, and F. Nori. Extraordinary momentum and spin in evanescent waves. *Nat. Commun.*, 5, 2014.
- [63] Fam Le Kien and A. Rauschenbeutel. Negative azimuthal force of nanofiber-guided light on a particle. *Phys. Rev. A*, 88:063845, Dec 2013.
- [64] Konstantin Y. Bliokh and Franco Nori. Transverse spin of a surface polariton. *Phys. Rev. A*, 85:061801, Jun 2012.
- [65] Yiqiong Zhao, J. Scott Edgar, Gavin D. M. Jeffries, David McGloin, and Daniel T. Chiu. Spin-to-orbital angular momentum conversion in a strongly focused optical beam. *Phys. Rev. Lett.*, 99:073901, Aug 2007.
- [66] A. Stiebeiner. *Nanofiber-based Spectroscopy of Organic Molecules*. PhD thesis, Johannes Gutenberg-Universität Mainz, 2014.
- [67] A. Timothy Birks and Youwei W. Li. The shape of fiber tapers. *Journal of Lightwave Technology*, 10(4):432–438, 1992.
- [68] R. Garcia-Fernandez, W. Alt, F. Bruse, C. Dan, K. Karapetyan, O. Rehband, A. Stiebeiner, U. Wiedemann, D. Meschede, and A. Rauschenbeutel. Optical nanofibers and spectroscopy. *Applied Physics B*, 105(1):3–15, 2011.

- [69] J. E. Hoffman, S. Ravets, J. A. Grover, P. Solano, P. R. Kordell, J. D. Wong-Campos, L. A. Orozco, and S. L. Rolston. Ultrahigh transmission optical nanofibers. *AIP Advances*, 4(6):–, 2014.
- [70] Florian Warken. *Ultradünne Glasfasern als Werkzeug zur Kopplung von Licht und Materie*. PhD thesis, Rheinische Friedrich-Wilhelms-Universität Bonn, 2007.
- [71] Florian Warken, Arno Rauschenbeutel, and Thomas Bartholomäus. Fiber pulling profits from precise positioning. *Photonics Spectra*, 42(3), 2008.
- [72] Eugen Vetsch. *Optical Interface Based on a Nanofiber Atom-Trap*. PhD thesis, Johannes Gutenberg-Universität Mainz, 2010.
- [73] A. Stiebeiner, R. Garcia-Fernandez, and A. Rauschenbeutel. Design and optimization of broadband tapered optical fibers with a nanofiber waist. *Optics Express*, 18(22):22677–22685, 2010.
- [74] Christian Wuttke. *Thermal excitations of optical nanofibers measured with a fiber-integrated Fabry-Pérot cavity*. PhD thesis, Johannes Gutenberg Universität Mainz, 2013.
- [75] E. Arimondo, M. Inguscio, and P. Violino. Experimental determinations of the hyperfine structure in the alkali atoms. *Rev. Mod. Phys.*, 49:31–75, Jan 1977.
- [76] Fam Le Kien, Philipp Schneeweiss, and Arno Rauschenbeutel. Dynamical polarizability of atoms in arbitrary light fields: general theory and application to cesium. *The European Physical Journal D*, 67(5):1–16, 2013.
- [77] Vladislav Gerginov, Andrei Derevianko, and Carol E. Tanner. Observation of the Nuclear Magnetic Octupole Moment of ^{133}Cs . *Phys. Rev. Lett.*, 91:072501, Aug 2003.
- [78] J. Terrien. News from the International Bureau of Weights and Measures. *Metrologia*, 4(1):43, 1968.
- [79] http://www.bipm.org/en/si/si_brochure/chapter2/2-1/second.html, 2014. Accessed 2014-05-02.
- [80] Robert W. Schmieder. Matrix elements of the quadratic stark effect on atoms with hyperfine structure. *AJP*, 40:297, Feb 1972.
- [81] Abbas Khadjavi, Allen Lurio, and W. Happer. Stark effect in the excited states of Rb, Cs, Cd, and Hg. *Phys. Rev.*, 167:128–135, Mar 1968.
- [82] N. L. Manakov, V. D. Ovisiannikov, and L. P. Rapoport. Atom in a laser field. *Physics Reports*, 141(6):319–433, 03 1986.
- [83] P. Rosenbusch, S. Ghezali, V. A. Dzuba, V. V. Flambaum, K. Beloy, and A. Derevianko. ac Stark shift of the Cs microwave atomic clock transitions. *Phys. Rev. A*, 79:013404, Jan 2009.

-
- [84] P. Schneeweiss, Fam Le Kien, and A. Rauschenbeutel. Nanofiber-based atom trap created by combining fictitious and real magnetic fields. *New Journal of Physics*, 16(0313014), January 2014.
- [85] Bindiya Arora, M. S. Safronova, and Charles W. Clark. Tune-out wavelengths of alkali-metal atoms and their applications. *Phys. Rev. A*, 84:043401, Oct 2011.
- [86] R. Grimm, M. Weidemüller, and Y. B. Ovchinnikov. Optical Dipole Traps for Neutral Atoms. *Advances in Atomic Molecular and Optical Physics*, 42:95–170, 2000.
- [87] H. E. White. *Introduction to Atomic Spectra*. McGraw-Hill, New York, 1934.
- [88] Fam Le Kien, P. Schneeweiss, and A. Rauschenbeutel. State-dependent potentials in a nanofiber-based two-color trap for cold atoms. *Phys. Rev. A*, 88:033840, Sep 2013.
- [89] B. S. Mathur, H. Tang, and W. Happer. Light shifts in the alkali atoms. *Phys. Rev.*, 171:11–19, Jul 1968.
- [90] Claude Cohen-Tannoudji and Jacques Dupont-Roc. Experimental Study of Zeeman Light Shifts in Weak Magnetic Fields. *Phys. Rev. A*, 5:968–984, Feb 1972.
- [91] W. T. Hill and C. H. Lee. *Light-Matter Interaction*. Wiley-VCH Verlag GmbH & Co. KGaA, 2007. ISBN: 978-3-527-40661-6.
- [92] József Fortágh and Claus Zimmermann. Magnetic microtraps for ultracold atoms. *Rev. Mod. Phys.*, 79:235–289, Feb 2007.
- [93] Harold J. Metcalf and Peter van der Straten. *Laser Cooling and Trapping*. Springer-Verlag, 1999.
- [94] A. I. Lvovsky, B. C. Sanders, and W. Tittel. Optical quantum memory. *Nat. Phot.*, 3:706–714, December 2009.
- [95] C. Simon. Quantum memories. *Eur. Phys. J. D*, 58:1, 2010.
- [96] A. Stute, B. Casabone, B. Brandstatter, K. Friebe, T.E. Northup, and R. Blatt. Quantum-state transfer from an ion to a photon. *Nat. Phot.*, February 2013.
- [97] Zhen-Sheng Yuan, Yu-Ao Chen, Bo Zhao, Shuai Chen, Jörg Schmiedmayer, and Jian-Wei Pan. Experimental demonstration of a BDCZ quantum repeater node. *Nature*, 454:1098–1101, Aug 2008.
- [98] Eric R. I. Abraham and Eric A. Cornell. Teflon feedthrough for coupling optical fibers into ultrahigh vacuum systems. *Applied Optics*, 37(10):1762–1763, 1998.
- [99] Wolfgang Alt. An objective lens for efficient fluorescence detection of single atoms. *Optik - International Journal for Light and Electron Optics*, 113(3):142–144, 2002.
- [100] Wolfgang Demtröder. *Laserspektroskopie 2*. Springer Spektrum, 6th edition, 2013.

- [101] Daniel Reitz. *Coherent manipulation of nanofiber-trapped atoms*. PhD thesis, Johannes Gutenberg Universität Mainz, 2014. to be published.
- [102] Robert Rath. Kompensatoren. *Abhandlungen der Braunschweigischen Wissenschaftlichen Gesellschaft*, 12:116–123, 1960.
- [103] R. H. Stolen and Clinton Lee. Development of the stimulated raman spectrum in single-mode silica fibers. *J. Opt. Soc. Am. B*, 1(4):652–657, August 1984.
- [104] X. Baillard, A. Gauguet, S. Bize, P. Lemonde, Ph. Laurent, A. Clairon, and P. Rosenbusch. Interference-filter-stabilized external-cavity diode lasers. *Optics Communications*, 266:609–613, 2006.
- [105] OptiGrate Corp., 562 Soth Econ Circle, Oviedo, FL 32765. *Volume Bragg Grating Specifications*, 2013.
- [106] N. Schlosser, G. Reymond, and P. Grangier. Collisional blockade in microscopic optical dipole traps. *Phys. Rev. Lett.*, 89(2):023005, Jun 2002.
- [107] J. E. Bjorkholm. Collision-limited lifetimes of atom traps. *Phys. Rev. A*, 38:1599–1600, Aug 1988.
- [108] C. Wuttke, G. D. Cole, and A. Rauschenbeutel. Optically active mechanical modes of tapered optical fibers. *Phys. Rev. A*, 88:061801, Dec 2013.
- [109] C. Wuttke and A. Rauschenbeutel. Thermalization via heat radiation of an individual object thinner than the thermal wavelength. *Phys. Rev. Lett.*, 111:024301, Jul 2013.
- [110] J. M. McGuirk, D. M. Harber, J. M. Obrecht, and E. A. Cornell. Alkali-metal adsorbate polarization on conducting and insulating surfaces probed with bose-einstein condensates. *Phys. Rev. A*, 69:062905, Jun 2004.
- [111] C. Henkel, S. Pötting, and M. Wilkens. Loss and heating of particles in small and noisy traps. *Applied Physics B: Lasers and Optics*, 69:379–387, June 1999.
- [112] V. S. Malinovsky and J. L. Krause. General theory of population transfer by adiabatic rapid passage with intense, chirped laser pulses. *The European Physical Journal D*, 14:147–155, 2001.
- [113] Nikolay V. Vitanov, Thomas Halfmann, Bruce W. Shore, and Klaas Bergmann. Laser-induced population transfer by adiabatic passage techniques. *Annual Review of Physical Chemistry*, 52:763–809, Oct 2001.
- [114] J. C. Camparo and R. P. Frueholz. A dressed atom interpretation of adiabatic rapid passage. *J. Phys. B: At. Mol. Phys.*, 17:4169–4178, 1984.
- [115] W. Happer. Optical pumping. *Rev. Mod. Phys.*, 44:169–249, Apr 1972.

-
- [116] G. Avila, V. Giordano, V. Candelier, E. de Clercq, G. Theobald, and P. Cerez. State selection in a cesium beam by laser-diode optical pumping. *Phys. Rev. A*, 36:3719–3728, Oct 1987.
- [117] M. Auzinsh, D. Budker, and S. Rochester. *Optically Polarized Atoms*. Oxford University Press, Inc., New York, 2010.
- [118] S. Kuhr, W. Alt, D. Schrader, I. Dotsenko, Y. Miroshnychenko, A. Rauschenbeutel, and D. Meschede. Analysis of dephasing mechanisms in a standing-wave dipole trap. *Phys. Rev. A*, 72:023406, Aug 2005.
- [119] Antoine Browaeys. private communication, 2013. CNRS - Institut d’Optique, Palaiseau.
- [120] D. A. Steck. *Cesium D Line Data*. available online at <http://steck.us/alkalidata>, 2010.
- [121] A. B. Matsko and V. S. Ilchenko. Optical resonators with whispering-gallery modes-part I: basics. *Selected Topics in Quantum Electronics, IEEE Journal of*, 12(1):3–14, Jan 2006.
- [122] D. O’Shea, C. Junge, S. Nickel, M. Pöllinger, and A. Rauschenbeutel. Ultra-high Q whispering-gallery-mode bottle microresonators: properties and applications. *SPIE Proceedings: Laser Resonator and Beam Control XIII*, 7913, Feb 2011.
- [123] Paul R. Berman, David R. Bates, and Benjamin Bederson, editors. *Cavity Quantum Electrodynamics*. Advances in Atomic, Molecular, and Optical Series. Elsevier Science & Technology Books, 1993.
- [124] Fam Le Kien, J.Q. Liang, K. Hakuta, and V.I. Balykin. Field intensity distributions and polarization orientations in a vacuum-clad subwavelength-diameter optical fiber. *Optics Communications*, 242(4-6):445 – 455, 2004.
- [125] Stefan Kuhr. *A concontrol quantum system of individual neutral atoms*. PhD thesis, Rheinische Friedrich-Wilhelms-Universität Bonn, June 2003.
- [126] S. Franke-Arnold, L. Allen, and M. Padgett. Advances in optical angular momentum. *Laser & Photonics Reviews*, 2(4):299–313, 2008.
- [127] Roberta Zambrini and Stephen M. Barnett. Quasi-intrinsic angular momentum and the measurement of its spectrum. *Phys. Rev. Lett.*, 96:113901, Mar 2006.
- [128] M. W. Beijersbergen, L Allen, H. E. L. O. van der Veen, and J. P. Woerdman. Astigmatic laser mode converters and transfer of orbital angular momentum. *Optics Communications*, 96(1-3):123–132, feb 1993.
- [129] Seung-Yeol Lee, Il-Min Lee, Junghyun Park, Sewoong Oh, Wooyoung Lee, Kyoung-Youm Kim, and ByoungHo Lee. Role of magnetic induction currents in nanoslit excitation of surface plasmon polaritons. *Phys. Rev. Lett.*, 108:213907, 2012.

- [130] J. Lin, J. P. B. Mueller, Q. Wang, G. Yuan, N. Antoniou, X.-C. Yuan, and F. Capasso. Polarization-controlled tunable directional coupling of surface plasmon polaritons. *Science*, 340:331, 2013.
- [131] F. J. Rodriguez-Fortuno, G. Marino, P. Ginzburg, D. O'Connor, A. Martínez, G. A. Wurtz, and A. V. Zayats. Near-Field Interference for the Unidirectional Excitation of Electromagnetic Guided Modes. *Science*, 340:328, 2013.
- [132] Polina V. Kapitanova, Pavel Ginzburg, Francisco J. Rodriguez-Fortuno, Dmitry S. Filonov, Pavel M. Voroshilov, Pavel A. Belov, Alexander N. Poddubny, Yuri S. Kivshar, Gregory A. Wurtz, and Anatoly V. Zayats. Photonic spin hall effect in hyperbolic metamaterials for polarization-controlled routing of subwavelength modes. *Nat. Commun.*, 5, 2014.
- [133] I. Söllner, S. Mahmoodian, A. Javadi, and P. Lodahl. A chiral spin-photon interface for scalable on-chip quantum-information processing. *arXiv:1406.4295*, June 2014.
- [134] A. B. Young, A. Thijssen, D. M. Beggs, L. Kuipers, J. G. Rarity, and R. Oulton. Polarization engineering in photonic crystal waveguides for spin-photon entanglers. *arXiv:1406.0714*, June 2014.
- [135] B. le Feber, N. Rotenberg, and L. Kuipers. A scalable interface between solid-state and flying qubits: observations of near-unity dipole helicity to photon pathway coupling. *ArXiv:1406.7741*, June 2014.
- [136] J. Petersen, J. Volz, and A. Rauschenbeutel. Chiral nanophotonic waveguide interface based on spin-orbit coupling of light. *ArXiv:1406.2184*, June 2014.
- [137] P. W. Barber and S. C. Hill. *Light Scattering by Particles: Computational Methods*. World Scientific Publishing, 1998.
- [138] F. Warken, E. Vetsch, D. Meschede, M. Sokolowski, and A. Rauschenbeutel. Ultra-sensitive surface absorption spectroscopy using sub-wavelength diameter optical fibers. *Opt. Express*, 15(19):11952–11958, Sep 2007.
- [139] Dieter Meschede. *Optik, Licht und Laser*. Vieweg+Teubner Verlag, 3rd edition, 2008.
- [140] Yuya Shoji, Tetsuya Mizumoto, Hideki Yokoi, I-Wei Hsieh, and Richard M. Osgood. Magneto-optical isolator with silicon waveguides fabricated by direct bonding. *Applied Physics Letters*, 92(7):–, 2008.
- [141] Ming-Chun Tien, Tetsuya Mizumoto, Paolo Pintus, Herbert Kromer, and John E. Bowers. Silicon ring isolators with bonded nonreciprocal magneto-optic garnets. *Opt. Express*, 19(12):11740–11745, Jun 2011.
- [142] Lei Bi, Juejun Hu, Peng Jiang, Dong Hun Kim, Gerald F. Dionne, Lionel C. Kimerling, and C. A. Ross. On-chip optical isolation in monolithically integrated non-reciprocal optical resonators. *Nat Photon*, 5(12):758–762, December 2011.

-
- [143] Christian E. Rüter, Konstantinos G. Makris, Ramy El-Ganainy, Demetrios N. Christodoulides, Mordechai Segev, and Detlef Kip. Observation of parity-time symmetry in optics. *Nat Phys*, 6(3):192–195, March 2010.
- [144] Liang Feng, Ye-Long Xu, William S. Fegadolli, Ming-Hui Lu, José E. B. Oliveira, Vilson R. Almeida, Yan-Feng Chen, and Axel Scherer. Experimental demonstration of a unidirectional reflectionless parity-time metamaterial at optical frequencies. *Nat Mater*, 12(2):108–113, February 2013.
- [145] Liang Feng, Maurice Ayache, Jingqing Huang, Ye-Long Xu, Ming-Hui Lu, Yan-Feng Chen, Yeshaiah Fainman, and Axel Scherer. Nonreciprocal light propagation in a silicon photonic circuit. *Science*, 333(6043):729–733, 2011.
- [146] Shanhui Fan, Roel Baets, Alexander Petrov, Zongfu Yu, John D. Joannopoulos, Wolfgang Freude, Andrea Melloni, Milos Popovic, Mathias Vanwolleghem, Dirk Jalas, Manfred Eich, Michael Krause, Hagen Renner, Ernst Brinkmeyer, and Christopher R. Doerr. Comment on “Nonreciprocal Light Propagation in a Silicon Photonic Circuit”. *Science*, 335(6064):38, 2012.
- [147] Katia Gallo, Gaetano Assanto, Krishnan R. Parameswaran, and Martin M. Fejer. All-optical diode in a periodically poled lithium niobate waveguide. *Applied Physics Letters*, 79(3):314–316, 2001.
- [148] Bo Peng, Sahin Kaya Ozdemir, Fuchuan Lei, Faraz Monifi, Mariagiovanna Gianfreda, Gui Lu Long, Shanhui Fan, Franco Nori, Carl M. Bender, and Lan Yang. Parity-time-symmetric whispering-gallery microcavities. *Nat Phys*, 10(5):394–398, May 2014.
- [149] Mohammad Hafezi and Peter Rabl. Optomechanically induced non-reciprocity in microring resonators. *Opt. Express*, 20(7):7672–7684, Mar 2012.
- [150] Erik J. Lenferink, Guohua Wei, and Nathaniel P. Stern. Coherent optical non-reciprocity in axisymmetric resonators. *Opt. Express*, 22(13):16099–16111, Jun 2014.
- [151] Fam Le Kien and A. Rauschenbeutel. Propagation of guided evanescent light in an array of atoms outside a nanofiber. *to be published*, 2014.
- [152] T. Lund-Hansen, S. Stobbe, B. Julsgaard, H. Thyrrstrup, T. Sünner, M. Kamp, A. Forchel, and P. Lodahl. Experimental realization of highly efficient broadband coupling of single quantum dots to a photonic crystal waveguide. *Phys. Rev. Lett.*, 101:113903, Sep 2008.
- [153] Christian Stehle, Helmar Bender, Claus Zimmermann, Dieter Kern, Monika Fleischer, and Sebastian Slama. Plasmonically tailored micropotentials for ultracold atoms. *Nat. Photon.*, 5(8):494–498, August 2011.
- [154] J. D. Thompson, T. G. Tiecke, A. S. Zibrov, V. Vuletic, and M. D. Lukin. Coherence and Raman sideband cooling of a single atom in an optical tweezer. *Phys. Rev. Lett.*, 110:133001, 2013.

- [155] A. M. Kaufman, B. J. Lester, and C. A. Regal. Cooling a single atom in an optical tweezer to its quantum ground state. *Phys. Rev. X*, 2:041014, Nov 2012.
- [156] J. D. Thompson, T. G. Tiecke, N. P. de Leon, J. Feist, A. V. Akimov, M. Gullans, A. S. Zibrov, V. Vuletic, and M. D. Lukin. Coupling a single trapped atom to a nanoscale optical cavity. *Science*, 340(6137):1202–1205, 2013.
- [157] Graydon, O. et al. Focus: Silicon photonics. *Nat. Phot.*, 4:491, 2010.
- [158] H. J. Kimble. The quantum internet. *Nature*, 453(7198):1023–1030, June 2008.
- [159] Susumu Noda, Masayuki Fujita, and Takashi Asano. Spontaneous-emission control by photonic crystals and nanocavities. *Nat Photon*, 1(8):449–458, August 2007.
- [160] K.-J. Boller, A. Imamolu, and S. E. Harris. Observation of electromagnetically induced transparency. *Phys. Rev. Lett.*, 66:2593–2596, May 1991.
- [161] L. V. Hau, S. E. Harris, Z. Dutton, and C. H. Behroozi. Light speed reduction to 17 metres per second in an ultracold atomic gas. *Nature*, 397:594–598, 1999.
- [162] Michael M. Kash, Vladimir A. Sautenkov, Alexander S. Zibrov, L. Hollberg, George R. Welch, Mikhail D. Lukin, Yuri Rostovtsev, Edward S. Fry, and Marlan O. Scully. Ultraslow group velocity and enhanced nonlinear optical effects in a coherently driven hot atomic gas. *Phys. Rev. Lett.*, 82:5229–5232, Jun 1999.
- [163] D. F. Phillips, A. Fleischhauer, A. Mair, R. L. Walsworth, and M. D. Lukin. Storage of light in atomic vapor. *Phys. Rev. Lett.*, 86:783–786, Jan 2001.
- [164] C. Liu, Z. Dutton, C. H. Behroozi, and L. V. Hau. Observation of coherent optical information storage in an atomic medium using halted light pulses. *Nature*, 409, 2001.
- [165] Melanie Müller. Realization and characterization of a phase locked laser system for coherent spectroscopy of fiber-coupled cesium atoms. Master’s thesis, Johannes Gutenberg Universität Mainz, 2010.
- [166] Bahaa E. A. Saleh and Malvin Carl Teich. *Fundamentals of Photonics*. John Wiley & Sons, Inc, 2nd edition, 2007. Chapter 21: Nonlinear Optics.
- [167] M. D. Lukin and A. Imamoglu. Nonlinear optics and quantum entanglement of ultraslow single photons. *Phys. Rev. Lett.*, 84:1419–1422, Feb 2000.
- [168] H. Schmidt and A. Imamoglu. Giant kerr nonlinearities obtained by electromagnetically induced transparency. *Opt. Lett.*, 21(23):1936–1938, Dec 1996.
- [169] S. E. Harris and Lene Vestergaard Hau. Nonlinear optics at low light levels. *Phys. Rev. Lett.*, 82:4611–4614, Jun 1999.
- [170] Jeffrey H. Shapiro. Single-photon kerr nonlinearities do not help quantum computation. *Phys. Rev. A*, 73:062305, Jun 2006.

- [171] Julio Gea-Banacloche. Impossibility of large phase shifts via the giant kerr effect with single-photon wave packets. *Phys. Rev. A*, 81:043823, Apr 2010.
- [172] Bor-Wen Shiau, Meng-Chang Wu, Chi-Ching Lin, and Ying-Cheng Chen. Low-light-level cross-phase modulation with double slow light pulses. *Phys. Rev. Lett.*, 106:193006, May 2011.
- [173] Chi-Ching Lin, Meng-Chang Wu, Bor-Wen Shiau, Yi-Hsin Chen, Ite A. Yu, Yong-Fan Chen, and Ying-Cheng Chen. Enhanced all-optical switching with double slow light pulses. *Phys. Rev. A*, 86:063836, Dec 2012.

Danksagung

An erster Stelle möchte ich Prof. Arno Rauschenbeutel für seine Betreuung und das entgegengebrachte Vertrauen bedanken. Er hat es ermöglicht, dass ich in den letzten Jahren an einem vielseitigen und physikalisch hoch interessanten Projekt arbeiten durfte.

Ich möchte mich bei den Mitgliedern des Doktoranden-Programm CoQuS bedanken, an dem ich während meiner Zeit in Wien teilnehmen durfte. Stellvertretend für alle, die für das Gelingen und reibungslose Funktionieren des Programms verantwortlich sind möchte ich hier besonders Prof. Markus Arndt, den ehemaligen Leiter des Programms und Dr. Christiane Losert-Valiente-Kroon erwähnen.

Ich bedanke mich herzlich bei den Mitgliedern der Arbeitsgruppe, die zu einem hervorragendem Klima beigetragen haben. Dadurch war es möglich stundenlang physikalische Probleme zu wälzen aber auch mal abseits der Physik hoch kreativ zu diskutieren. Bei David Papencordt, Michael Scheucher und Bernhard Albrecht möchte ich mich für die gute Atmosphäre im Büro bedanken.

Den beiden Post-Docs Dr. Philipp Schneeweiß und Dr. Clément Sayrin möchte ich an dieser Stelle sehr für ihre große Unterstützung und das unermüdliche Korrekturlesen meiner Arbeit danken. Philipp, der immer ein Schritt weiter plant und so dafür sorgt, dass die Experimente reibungslos aneinandergereiht werden können. Clément konnte mir durch sein tiefes physikalisches Verständnis viele Sachverhalte deutlich machen. In den vielen Stunden, die wir zusammen im Labor verbracht haben konnte ich einiges von seiner gründlichen Arbeitsweise lernen. Meinem Kollegen Daniel Reitz danke ich an dieser Stelle sehr. Nicht nur dass er mich am Anfang in die dunklen Abgründe des Experiments eingeführt hat, wir haben auch zusammen den Umzug nach Wien erfolgreich über die Bühne gebracht. Darüber hinaus denke ich gerne an die vielen lustigen Stunden im Labor.

Ich danke Dr. Christian Junge, der mit seiner Freundschaft dafür gesorgt hat, dass ich auch hier in Wien noch ein Privatleben hatte.

Meiner Olivia kann ich nicht genug für ihre immerwährende Unterstützung und ihr Verständnis während der letzten Jahre danken. Zu guter Letzt bedanke ich mich ganz besonders bei meinen Eltern und bei meinen Geschwistern. Sie haben mich sehr unterstützt und mich zum Beispiel durch regelmäßige Besuche immer wieder motiviert.

LEBENS LAUF

Rudolf Mitsch
Turmburggasse 13/2-3
1060 Wien
Österreich

Persönliche Daten

Geburtsdatum: 11. Juli 1983
Geburtsort: Heppenheim
Staatsangehörigkeit: deutsch

Ausbildung

seit 10/2009	Technische Universität Wien und Johannes Gutenberg-Universität Mainz Doktorand in Technischer Physik
09/2006 – 03/2009	Technische Universität Darmstadt und Universidad de Salamanca, Spanien Master of Science in Physik
04/2004 – 09/2006	Technische Universität Darmstadt, Bachelor of Science in Physik
08/1994 – 07/2003	Starkenburger-Gymnasium, Heppenheim
08/1990 – 07/1994	Eichendorffschule, Kirschhausen